Measuring Particle Migration in Neutrally Buoyant Suspensions with Light Attenuation

Jasper Kamsteeg

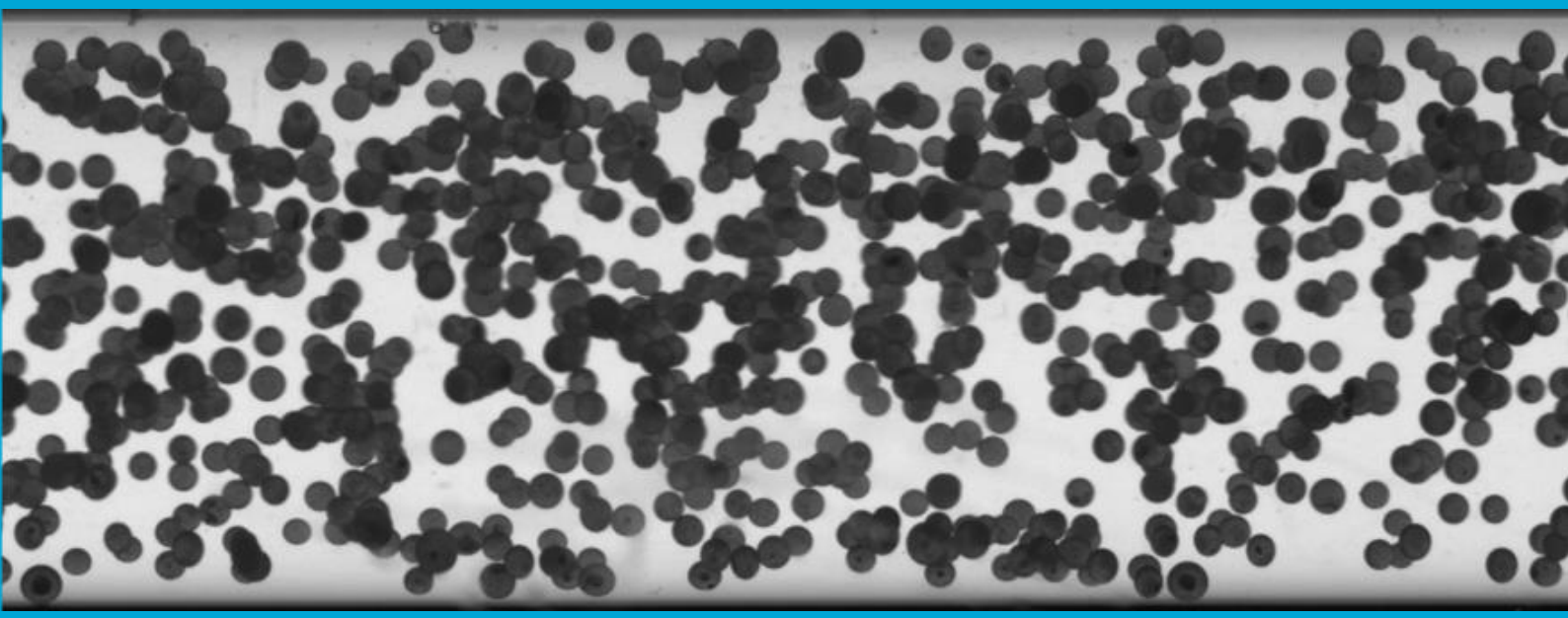

TU Delft

Measuring Particle Migration in Neutrally Buoyant Suspensions with Light Attenuation

by

Jasper Kamsteeg

to obtain the degree of Master of Science in Mechanical Engineering
at the Delft University of Technology,
to be defended publicly on August 28, 2025 at 10:00 AM.

Student number:	4926102	
Master's track:	Energy, Flow & Process Technology	
Thesis committee:	Prof.dr.ir C. Poelma,	Supervisor & Chair, TU Delft
	Dr.ir. W.J. Hogendoorn,	Supervisor, TU Delft
	Dr. A. Laskari,	TU Delft

An electronic version of this thesis is available at http://repository.tudelft.nl/.

Acknowledgements

Firstly I would like to thank Christian and Willian for your supervision during this project. I enjoyed our meetings and appreciate the input you had on everything from experiment design to thesis drafts. Your guidance has been essential for the successful completion of this thesis. Working on this project with you has been a great opportunity. I also want to thank Alberto, Ali and Udhav for your help with the experimental work. I want to thank anyone within the department that helped with the technical support of the experimental setup. My gratitude also extends to my friends, both inside and outside the TU, for your support during this process and the good times we had and will continue to have. Lastly I want to thank my family, specifically my parents and sisters, for your continued encouragement and for offering plenty of distractions during this project.

Jasper Kamsteeg
Delft, August 2025

Abstract

Suspension pipe flows can exhibit a behaviour called core-peaking where the particles accumulate in the centre of the pipe. This is due to shear-induced migration, where particles migrate towards areas of the flow with lower shear rate. While this concept is well documented, the exact causes are still unknown. Experimental research can uncover how this behaviour is impacted by different flow properties. This knowledge can be used to predict whether a given system will display core peaking behaviour. Knowing this a priori is convenient, as core peaking can impact the pressure drop in the pipe flow significantly. This thesis investigates the applicability of an experimental method that uses light attenuation to measure volume fraction distributions in a suspension pipe flow. Investigating this method is worthwhile as it is relatively quick and affordable compared to other methods like MRI. The theoretical relationship between the concentration of a substance and the attenuation of light is given by the Beer-Lambert law. However, this linear law does not hold for dense suspensions. To account for this, a set of calibration experiments was done in a setup where the path length was varied consistently. The results give a relationship between the attenuation and the amount of particles, expressed as the product of the volume fraction and the path length. This relationship is initially linear before it transitions to a cube root function for higher particle loadings. This change is thought to be due to multiple scattering becoming more prominent when more particles are present. The found calibration curve was then applied to attenuation measurements that were done in a pipe flow setup. However, the resulting volume fractions deviate significantly from the values expected based on the known amount of particles in the flows. This deviation suggests that there are significant differences between these pipe flow experiments and the calibration experiments that cause a difference in the measured attenuation for the same particle loadings. The volume fraction distributions that were found are thus not quantitatively correct, but by comparing them, the accuracy of this method can still be defined. Because the behaviour in the pipe flow is axisymmetric, the radial volume fraction distributions can be found from a single measured projection with the inverse Abel transform. However, the measured attenuation profiles were not symmetric. This means that the resulting radial volume fraction profiles are not actual representations of the real volume fraction distributions. This also means that the current data cannot be used to study particle migration in detail. Nevertheless, the accuracy of the method can be determined by looking a the measured attenuation profiles directly. Even at small path lengths, a difference of 1% in volume fraction was measured successfully. This proves that the proposed experimental method is in theory accurate enough to be used to measure volume fraction distributions in suspension pipe flows. To apply this method successfully, the identified improvements to the experimental setup and processing will need to be implemented. Additional research will be necessary to verify if these improvements are sufficient.

Contents

1 Introduction

Suspension pipe flows are present in many different processes, including construction, dredging, and blood flows. While the behaviour of these suspensions has been a topic of research for many decades, there are still concepts that are not fully understood. One such topic of interest is particle migration. Under certain flow conditions, a homogeneously mixed suspension will become heterogeneous due to the radial migration of particles. This redistribution of particles changes the behaviour of the system. For example, the effective viscosity is impacted, changing the pressure drop over a length of pipe. This is one reason why it is important to further the understanding of particle migration in suspensions, as this will allow the proper prediction of the pump requirements for industrial pipe flows. At low solid volume fractions and Reynolds numbers, particles undergo inertial migration where they migrate to an equilibrium position about halfway between the pipe axis and the wall. This phenomenon has been researched extensively and the responsible forces are generally understood. However, at higher volume fractions and Reynolds numbers, the particles undergo shear-induced migration where the particles migrate towards areas of the flow with lower shear rate. In the case of pipe flows this is the centre of the pipe. The onset of this type of migration and the rate at which it happens are dependent on the Reynolds number, the solid volume fraction and the particle size and shape. The reasons these properties impact the migration are not fully understood. Research is still ongoing to capture this behaviour and the influence of these different parameters on the migration. Additionally there have been efforts to model this behaviour.
The accumulation of particles in the centre of the pipe due to shear-induced migration specifically has a significant impact on the flow. It impacts the flow velocity profile as well as the friction of the pipe flow. This is due to the aforementioned change in effective viscosity caused by the concentration gradient in the flow. When solid particles are added to a liquid flow, they act as non-deformable obstacles, increasing the resistance to flow and thus the effective viscosity. There are different suspension viscosity models that attempt to capture the effect of added particles in a flow. They mostly model suspensions as single phase liquid flows of higher viscosity. However, these models assume a homogeneous distribution of particles. In the case of core-peaking flows due to shear-induced migration, the large difference in local concentration causes these suspension viscosity models to fail at predicting the friction. This is because a particle free layer forms between the wall and the particle core. This acts as a lubrication layer of lower viscosity, lowering the friction in the flow compared to the suspension viscosity model predictions. Additionally, the behaviour of dense suspensions, especially around the turbulence transition, is distinctly different from single phase flows. This means that a suspension viscosity model is not sufficient for predicting the turbulence transition of suspension flows.
Many current investigations into shear-induced migration specifically pertain to neutrally buoyant suspensions of spherical particles. While other suspensions also exhibit this behaviour, examining it in detail is easier when buoyancy effects are eliminated and the use of spherical particles eliminates orientation effects on the behaviour of the particles. The goal of much of this research is creating a model that accurately predicts the change in effective viscosity due to core-peaking. Such a model could serve to calculate the pressure drops in suspension pipe flows. While different models have been proposed, none are universally applicable. An all encompassing model should accurately anticipate the concentration gradient and the resulting effective viscosity and drag in the flow. It should take the Reynolds number, solid volume fraction and particle size and shape into account. Formulating such a model will require a lot of additional knowledge about shear-induced migration. In neutrally buoyant suspensions of spherical particles, the impact of the Reynolds number, solid volume fraction and particle size can be studied separately without the impact of particle shape and density differences. Some current investigations vary all these three parameters while others keep the particle size constant and only vary Reynolds number and the solid volume fraction. What most of these more recent investigations have in common is that they tend to use methods that are time consuming and expensive. Common methods are magnetic resonance imaging (MRI) and direct numerical simulations (DNS). The initial goal of this thesis was to find and apply an experimental technique for the investigation of neutrally buoyant suspension pipe flows that is less expensive, less time consuming and generally easier to apply than MRI and DNS. Light attenuation measurements were identified as a worthwhile method to measure volume fraction distributions. This method was chosen because it is relatively quick and affordable and has the potential to be fairly precise. In theory this method can be used to measure the degree of core peaking in suspension pipe flows of different Reynolds numbers, volume fractions and particle sizes. This information can then be used to investigate the impact these variables have on shear-induced migration. The current investigation is limited to a single particle size, but the Reynolds number and volume fraction will be varied. The experiments will be used to review the accuracy of the light attenuation measurement. This thesis will start with a review of relevant literature in section 2, concluding with the posed research questions. The experimental methods will be discussed in section 3. The results of the calibration experiments are given in section 4 and those of the pipe flow experiments in section 5. This is followed by a discussion of the results in section 6 and finally the conclusion and recommendations in section 7.

2 Literature research

Before doing experiments it is important to know the relevant background information relating to particle migration and the measurement methods that have been applied to measure this behaviour. The general principles of light attenuation measurements should also be explored. This section contains the literature research that was done before the experiments were started. Section 2.1 will discuss concepts of fluid dynamics related to single phase pipe flows that are important background knowledge for suspension pipe flows. Section 2.2 will cover concepts specific to suspensions in general and to suspension pipe flows. Section 2.3 will cover the concepts of inertial and shear-induced particle migration. Then section 2.4 will cover the available measurement methods and justify the choice for camera imaging light attenuation measurements. The expected issues with camera imaging are also discussed and the proposed experiments are described. Lastly section 2.5 contains the conclusion of this literature review and will present the further research questions for this thesis.

2.1 Single-phase pipe flows

There are some concepts relating to single phase pipe flows that are important to understand before delving into suspension flows. Reynolds (1883) was the first to define what is now known as the Reynolds number. It is used to qualify a flow as being either laminar or turbulent. It is also used to calculate the energy loss through friction. The Reynolds number is the ratio of inertial forces to viscous forces in the flow. It is defined as

$$Re = \frac{\rho u l}{\mu}. \tag{1}$$

Here ρ is the density of the fluid, u is the flow velocity, l is a characteristic geometric length scale of the flow and μ is the fluid's dynamic viscosity. In the case of a pipe flow the characteristic length scale is taken to be the inner diameter of the pipe D. It is also possible to replace the ρ/μ term with the kinematic viscosity $\nu = \mu/\rho$.

When qualifying a flow as either laminar or turbulent, the transitional Reynolds number or critical Reynolds number needs to be known. For flow in smooth pipes, Avila et al. (2011) defined the critical Reynolds number, as $Re_c = 2040$. They show that the single phase turbulence transition region is characterised by turbulent puffs. These are local, transient patches of turbulence surrounded by laminar flow. These puffs can split when a patch of chaotic vorticity escapes downstream and seeds a new puff, proliferating turbulence. The puffs have a limited lifetime determined by the time scale for the decay of turbulence. Similarly, the splitting of puffs has a timescale. As the Reynolds number increases, the time scale for the decay of turbulence increases whilst the time scale of the splitting of puffs decreases. At the critical $Re_c = 2040$, the time scale of turbulence proliferation matches the time scale of turbulence decay and thus above this value, turbulence persists. At even higher Reynolds numbers the turbulence proliferation occurs not only in the form of splitting puffs but also the growth of puffs.

Another important concept is the head loss over a length of pipe. This is defined as the loss of energy in the flow due to friction. This concept is equivalent to the pressure drop over a length of pipe. The pressure drop and head loss are related as such,

$$h_f = \frac{\Delta p}{\rho g}, \tag{2}$$

where h_f is the head loss, Δp is the pressure drop and g is the gravitational acceleration constant. For flow in pipes, the Darcy-Weisbach equation relates the head loss to the average flow velocity as

$$h_f = f \frac{L}{D} \frac{u^2}{2g}. \tag{3}$$

Here L is the length of the pipe segment, and f is the Darcy friction factor. This friction factor is a function of the Reynolds number and the ratio of the pipe roughness ϵ over the pipe diameter D, called the relative roughness. For a fully developed pipe flow with known Reynolds number and pipe roughness, the friction factor can be found. With this, the head loss or pressure drop can be calculated. In the laminar flow regime the friction factor is independent of the relative roughness, and it is known to follow a simple inverse relation with the Reynolds number

$$f = \frac{64}{Re}. \tag{4}$$

This is an exact definition of the friction factor in the laminar regime, found by combining Eq. 3 and 2 into an equation for the pressure drop and equating this to the pressure drop found with the Hagen-Poiseuille equation. The Hagen-Poiseuille equation is an exact relation for the pressure drop for laminar flow in a pipe that can be

directly derived from the Navier-Stokes equations. In the turbulent regime the friction factor does not have an exact definition, but instead can be found using various empirical correlations. For a smooth pipe the friction factor initially follows the Blasius correlation (Blasius, 1913), which is valid for $4000 \lesssim Re \lesssim 10^5$ (White, 2016),

$$f = 0.316 Re^{-1/4}. \tag{5}$$

Moody (1944) created a diagram that plots Eqs. 4 and 5 as well as empirical relationships for the friction factor for turbulent flow in non-smooth pipes, shown in Fig. 1. This Moody diagram can be used to quickly find the friction factor for a pipe flow where the Reynolds number and relative roughness are known. It can be seen from Fig. 1 that the friction factor is a non-monotonic function of the Reynolds number, increasing in the transition region from the curve of Eq. 4 up to the relevant turbulent curve. When a specific pipe flow is characterized, often either the local minimum or the inflection point of the measured friction factor curve will be used to define the critical Reynolds number. This is a practical way of defining the Re_c for a specific system. The resulting value may deviate from the value predicted by Avila et al. (2011) due to differences in the pipe flow setup.

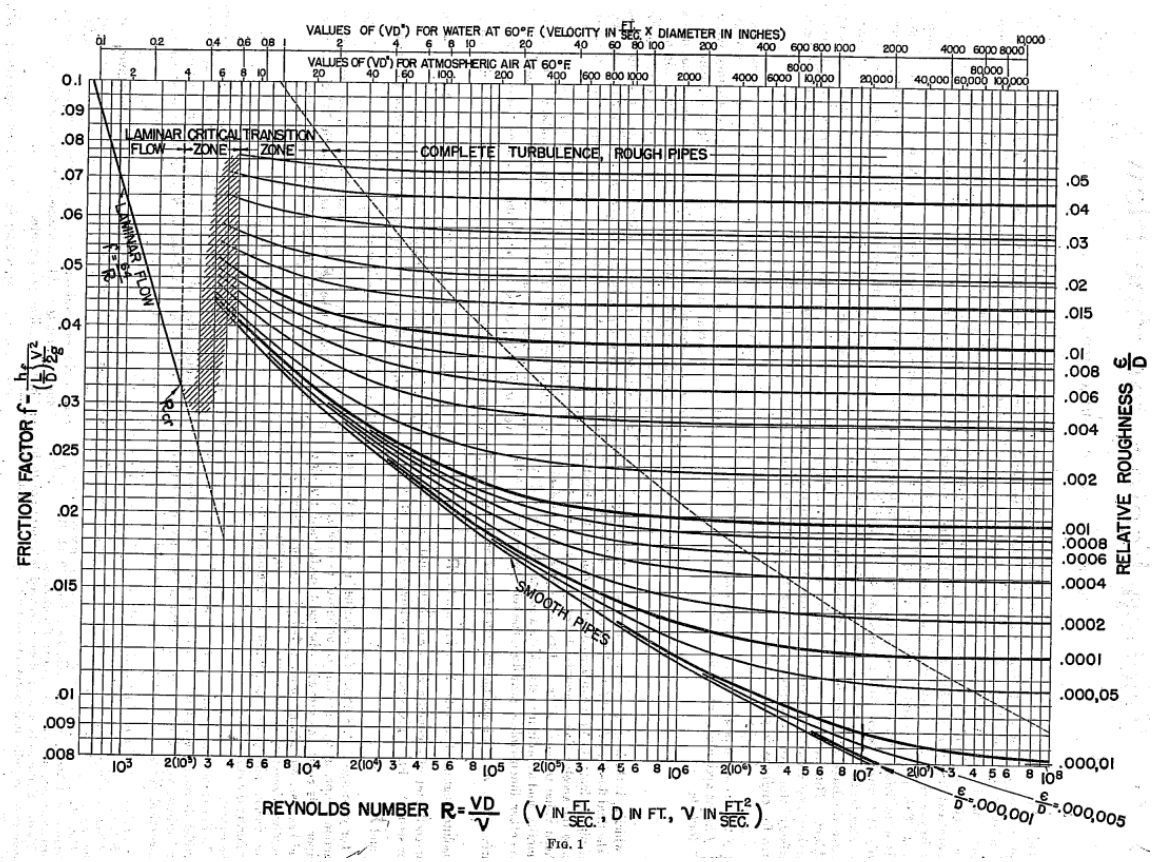

Figure 1: The original diagram created by L.F. Moody for determining the friction factor of a pipe flow based on the relative roughness and Reynolds number, now known as a Moody Diagram. The figure uses the kinematic viscosity definition of the Reynolds number and uses V for flow velocity instead of u. Reproduced from Moody (1944).

Laminar flow in pipes is characterised by the movement of fluid in smooth paths parallel to the pipe wall. There is no exchange of fluid between the layers. Turbulent flow on the other hand is characterised by chaotic movement of the fluid. The velocity at any point has fluctuations in all directions. This causes mixing of the fluid. The resulting time-averaged velocity profiles for both types of pipe flow are shown in Fig. 2. These profiles are valid for fully developed pipe flows. A pipe flow is considered fully developed when the time-averaged velocity profile no longer changes further downstream. The length of the pipe after the inlet where the flow is still developing is called the development region, as shown in Fig. 3. The length of this region is called the entrance length. In this development region the effects of the pipe wall on the bulk flow propagate inwards radially as a boundary layer. Once the boundary layers meet, the flow is fully developed. There are many different relations for the entrance length in both laminar and turbulent flow that were attained through analytical, numerical or

empirical methods. Correlations that are often used are given in the following equations (e.g. White, 2016)

$$\frac{\mathcal{L}_{lam}}{D} = 0.06Re, \tag{6a}$$

$$\frac{\mathcal{L}_{tur}}{D} = 1.6(Re)^{1/4}. \tag{6b}$$

It is clear that for Reynolds numbers of the same order, the entrance length for the turbulent case is much shorter. This is due to the turbulent mixing that happens which expedites the process of flow development. For most engineering applications the Reynolds number is such that the entrance effects become negligible after a pipe length of a few pipe diameters. The following engineering approximation for the entrance length is thus often used for easier calculations

$$\frac{\mathcal{L}}{D} \approx 10. \tag{7}$$

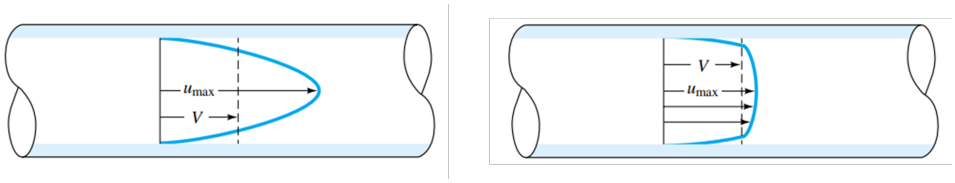

Figure 2: Velocity profiles in fully developed pipe flow. Laminar flow on the left and turbulent flow on the right. The dashed lines and capital V show the mean velocity. Adapted from White (2016)

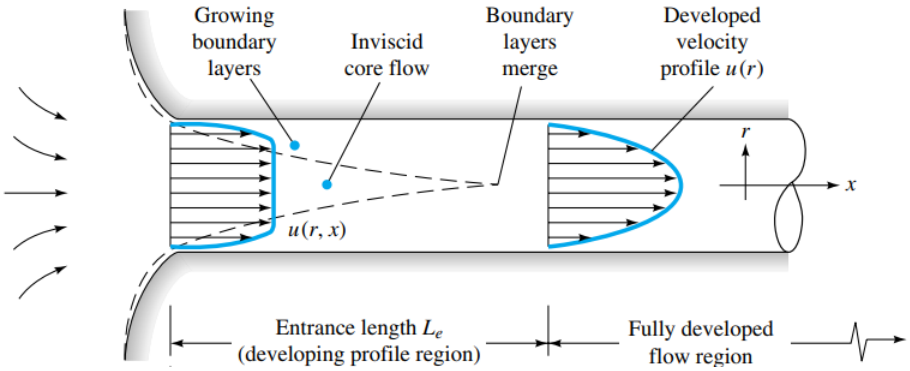

Figure 3: Visual explanation of the concept of flow development in a pipe flow, adapted from White (2016).

2.2 Suspensions

A suspension is defined as a continuous fluid phase with solid particles dispersed in it. In this work the word suspension will only be used to describe solid, non-Brownian particles dispersed in a liquid phase, unless stated otherwise. A non-Brownian particle is relatively large, having a size of $d \gtrsim 1\,\mu m$. If the particles are smaller they will undergo Brownian motion. Together with other driving forces like electrostatic repulsion this causes the particles to stay homogeneously dispersed, regardless of the density difference between the phases. These dispersions of small particles are called colloidal dispersions or colloids. The particles in colloids do not experience particle migration in the same way that non-Brownian particles do. Colloids are not included in the rest of this work unless specifically mentioned. In a suspension the solid particles should also be insoluble in the liquid phase as this would instead create a solution, not a suspension. An example of a suspension can be seen in Fig. 4.

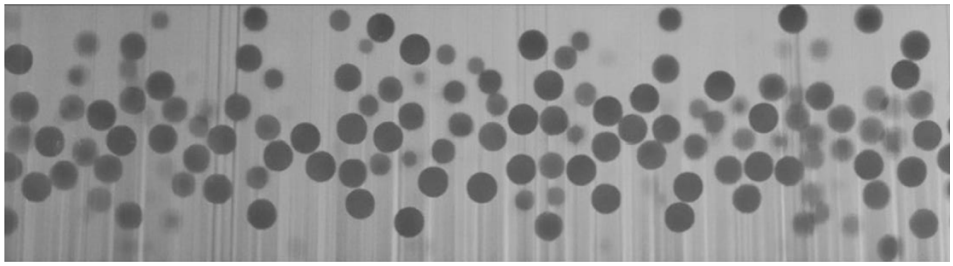

Figure 4: An image of a suspension. This image was made to study the behaviour of particles in a vertical oscillatory pipe flow. Reproduced from Snook et al. (2015).

Apart from the individual material properties of the suspended and continuous phases there are other properties of importance when considering suspensions. Firstly the volume fractions. Two-phase suspensions have a solid and a liquid volume fraction defined as

$$\phi_s = \frac{V_s}{V} \tag{8a}$$

$$\phi_l = \frac{V_l}{V} \tag{8b}$$

where ϕ_s, ϕ_l, V_s and V_l respectively denote the volume fractions and volumes of the solid and liquid phases and V denotes the total suspension volume. It is evident that in a two phase suspension $\phi_s + \phi_l = 1$. Because of this, often only the solid volume fraction is mentioned as simply ϕ. Other properties of influence are the size and shape of the particles. These properties can influence the suspensions behaviour, like the percolation threshold in the suspension, i.e. the volume fraction at which a fully connected network of particles across the entire system exists, (Xue, 2004) or the light scattering behaviour (Piedra et al., 2019). This work will only focus on suspensions with spherical particles. Lastly, the density difference between the solid and liquid phase, ρ_s and ρ_l, will determine whether the particles will sediment, float or whether the suspension is neutrally buoyant. While other properties that are not mentioned here can also have an impact on the behaviour of suspensions, the mentioned properties are of specific importance to the current investigation.

2.2.1 Suspension pipe flows

There are some concepts that are needed to describe the pipe flow of suspensions. One of those concepts is the particle Reynolds number which is given by

$$Re_p = \frac{\rho_l u d}{\mu_l} \tag{9}$$

where ρ_l and μ_l are the density and viscosity of the continuous liquid phase and d is the particle diameter. The velocity u can be defined in different ways depending on the application and the available information. When there is no detailed information available about the velocity of the particle, the average flow velocity can be used, see for example Han et al. (1999). If the particle is stagnant, the fluid velocity at the height of the particles centre may be used, as was done by Burdick et al. (2001). If the particles are rising or settling in a stagnant fluid, the velocity of the particle itself can be used, as was done by Waldschläger et al. (2020). If a particle is flowing and the velocity profile in the flow is known, then the velocity difference across the particle may be used, as was done by Kulkarni and Morris (2008). In this case $u = \dot{\gamma} d$ where $\dot{\gamma}$ is the shear rate. The first and last mentioned definitions are most applicable to suspension pipe flows. For suspension pipe flows it is useful to mention the size of the particles relative to the pipe diameter. In the case of spherical particles the dimensionless parameter d/D is used.
The presence of particles has an impact on the effective suspension viscosity. Every particle is an obstacle to the flow, increasing the effective viscosity of the suspension. One of the models that can be used to account for this impact is the empirical Eilers' viscosity model (Eilers, 1941)

$$\frac{\mu_s}{\mu_l} = \left(1 + 1.25 \frac{\phi}{1 - \phi/0.64}\right)^2 \tag{10}$$

where μ_s is the suspension viscosity and 0.64 is the random close packing fraction for monodispersed perfect spheres. For small particles that are close to spherical with a slim range of polydispersity, the results of eq. 10 are sufficiently accurate, especially at lower volume fractions. The shortcomings of the Eilers viscosity model

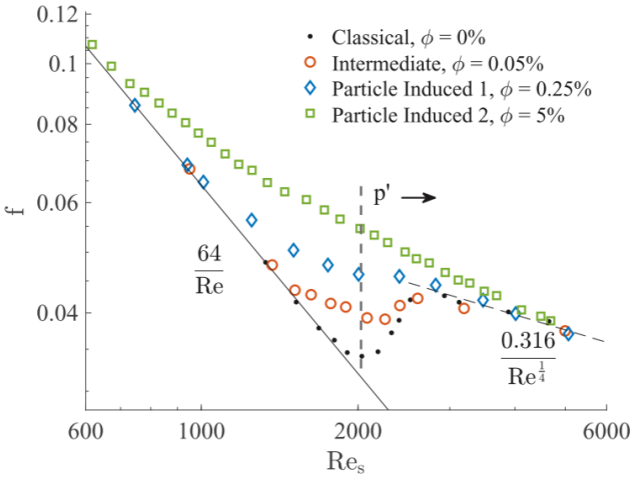

Figure 5: Moody diagram showing the friction factor as a function of the suspension Reynolds number for four different solid volume fractions. The particles were the same size for all four cases, namely $d/D = 0.175$. Adapted from Hogendoorn, Chandra, et al. (2021).

and similar models is expanded upon in section 2.3.3. This suspension viscosity can then be used to calculate the suspension Reynolds number as

$$Re_s = \frac{\rho_l u D}{\mu_s}. \tag{11}$$

In certain situations the particle distribution in suspensions may become heterogeneous as a result of the flow. This can impact the effective viscosity of the system. If the effective viscosity of the suspension changes with the shear rate applied to the flow, the suspension is considered a non-Newtonian fluid.

The presence of particles also affects the turbulence transition. Hogendoorn and Poelma (2018) found that particle-laden flows have a lower critical Reynolds number than single-phase flows. At low volume fractions, the particles introduce disturbances and trigger turbulent patches to form at lower Reynolds numbers compared to single-phase flows. At high volume fractions however, the onset of turbulent flow happens much more gradually. Instead of distinct separated patches of fluctuating turbulent flow, the velocity and pressure fluctuations are continuous and they increase with increasing Reynolds number. As a result of this, the friction factor follows a different path for particle laden flows than for single-phase flows. Instead of the non-monotonic function that is characteristic of the turbulence transition in single-phase flow, the friction factor decreases monotonically with increasing Reynolds number. As the function does not have a minimum and the proliferation of turbulence is not dependent on puffs, the critical Reynolds number cannot be defined in the same way as it was for single-phase flows. In their experimental research, Hogendoorn, Chandra, et al. (2022) instead defined the critical Reynolds number based on the deviation of the measured friction factor from eq. 4. They used a threshold of $70/\mathrm{Re}$. The Reynolds number where the measured friction factor first exceeds this threshold is deemed the critical Reynolds number. They showed that the critical suspension Reynolds number scales with ϵ^{-1} where $\epsilon = f(\phi, d/D)$ is the amplitude of the particle-induced perturbations. In between these two cases of laminar-like turbulence transition and fully particle induced transition, systems show intermediate behaviour. In these flows, both patches of turbulent fluctuations and continuous fluctuations can be observed, according to Hogendoorn, Chandra, et al. (2021). Fig. 5 shows the measured friction factor for four cases they investigated. Here the transition from a non-monotonic function in the single-phase case to the monotonic decline in the particle-induced cases can clearly be seen.

2.3 Particle migration

One of the characteristic behaviours seen in suspension pipe flows is the radial migration of particles. Under certain flow conditions the radial distribution of particles does not remain homogeneous. Segré and Silberberg (1962) were the first to show that at relatively low Reynolds numbers ($\mathrm{Re}<30$) and solid volume fraction ($\phi_s < 0.005$) the particles migrate away from the centreline of the pipe and form an annulus. This equilibrium position has a radius of $0.6R$. This migration is called inertial migration. Karnis et al. (1966) showed that at higher solid volume fractions ($\phi_s \gtrsim 0.25$), particle interaction effects become prominent. This results in particles migrating towards the centre where they accumulate. This core peaking behaviour also effects the

velocity profile of the flow. Instead of the parabolic profile expected from a single phase or homogeneously dispersed flow, these flows exhibit a blunted velocity profile. They used hard spherical particles, as well as rods and discs. Later, Gadala-Maria and Acrivos (1980) conducted rheometric experiments of a suspension of polystyrene spheres in a silicone oil mixture. They measured a steady decrease of the apparent viscosity at high solid volume fractions ($\phi_s > 0.40$) over the course of hours. The viscosity eventually converged to a lower value. Leighton and Acrivos (1987) reproduced these results and showed that this reduction in apparent viscosity was due to the shear induced migration of the particles out of the gap towards the reservoir of the rheometer. They also explain this migration as being a result of irreversible particle-particle interactions. It is generally understood that the particle migration towards the pipe centre described by Karnis et al. (1966) and the migration of particles in the rheometer described by Gadala-Maria and Acrivos (1980) are both caused by this shear-induced migration.

2.3.1 Differences between pipe and duct flow

Although this thesis focusses on suspension flows in pipes with a circular cross section, a significant amount of research has been done on suspensions flowing through rectangular or square ducts. Many of the concepts relevant to suspension pipe flows are also present in suspension duct flows. There are, however, notable differences. It is important to mention these differences so that the results of these duct flow studies can be included in this discussion when they are also relevant to pipe flows.
When defining the Reynolds number or the suspension Reynolds number for a rectangular duct the characteristic length scale used is the hydraulic diameter which is defined as (e.g. White, 2016)

$$D_h = \frac{4A}{P} \tag{12}$$

where A is the cross sectional area of the duct and P is the wetted perimeter. In the case of a square duct with four equal sides a the hydraulic diameter is thus $D_h = 4a^2/4a = a$. The concept of a hydraulic diameter can be applied to a pipe of any cross sectional shape, not just rectangles.
The dimensionless size of the particles is defined as d/H where H is the height of the duct. In a square duct this can of course be the length of any of the sides. In a rectangular duct the height is the length of the shorter sides. This is because in experiments for suspension flows, the rectangular duct is often much wider than it's height. This is done because then the wall effects of the closer walls will be much more prominent than the further walls. If the wall effects of the far walls become negligible, the flow resembles a flow between two parallel plates. Particle migration can then be studied in a single plane, simplifying the investigation. This dimensionless particle size definition can also be used for 2D numerical investigations as was done by e.g. Nott and Brady (1994). In these studies often the particle Reynolds number is used to classify the flow.
When the flow in a duct of non-circular cross section is turbulent, secondary flow patterns are present. In the case of rectangular ducts, these are non-zero average velocities perpendicular to the axial flow direction that bring fluid from the core towards the corners. This forms eight eddies in the corners, two in each corner, one on both sides of the bisector. The characteristic velocity of these secondary flows scales with the bulk velocity u_b (e.g. Pirozzoli et al., 2018). This velocity has a maximum of around 0.02 u_b. This behaviour also impacts the mean streamwise velocity field.

2.3.2 Inertial migration

Segré and Silberberg (1962) were the first to describe the inertial migration of particles in a pipe flow, where particles migrate to an equilibrium position in between the wall and the pipe core. They called this the "tubular pinch" effect. This has been researched further experimentally (e.g. Matas, Glezer, et al., 2004), theoretically (e.g. Matas, Morris, et al., 2009) and numerically (e.g. Liu and Wu, 2019; Chun and Ladd, 2006). This inertial migration is most prevalent at low Reynolds numbers and volume fractions when particle interactions are infrequent. While an upper limit for the Reynolds number is not well defined, the mechanisms that cause this migration are only present for $Re > 1$. In other words, the inertial forces in the flow need to be significant compared to the viscous forces. Segré and Silberberg (1962) show that the phenomenon of inertial migration is not dependent on the volume fraction within the range that was considered in their study ($\phi < 0.005$). They describe it as an individual particle phenomenon.
In the case of neutrally buoyant suspensions, inertial migration is caused by opposing lift forces, explained by Martel and Toner (2014). They explain that a particle near the wall will undergo a wall interaction force, where the particle moves slightly slower than the surrounding fluid due to an increase of drag on the particle near

the wall. This means the fluid has to pass around the particle. In the space between the wall and the particle, the space is confined. This constricts the fluid flow which causes the pressure to build up here. The fluid that instead passes over the particle will accelerate, leading to lower pressure on the side of the particle away from the wall. This pressure gradient causes a lift force on the particle, directed away from the wall. Additionally the particle will undergo a shear gradient lift force. This is caused by the velocity gradient that is present in the wall normal direction. When considering the problem in two dimensions, the magnitude of the velocity of the fluid around the particle will be different on either side of it. If we assume that the particle travels with a velocity equal to the fluid velocity at the height of the particle centre, the fluid will have a positive relative velocity above the particle, nearer to the pipe centre. The relative fluid velocity on the side of the particle near the wall will be negative. The particle will cause the flow on both sides of it to accelerate. Near the wall the moving particle pushes the fluid down and around it. Near the pipe centre the liquid moves faster than the particle and thus has to move up and around it. Since the velocity gradient increases towards the wall in the case of a parabolic velocity profile, the absolute value of the relative velocity between the fluid and the particle is higher near the wall than near the centre of the pipe. This means that the increase in liquid velocity caused by the moving particle will be greater on the side near the wall. This results in a larger pressure drop and thus an induced lift force pointed towards the wall. These two opposing lift forces are presented in Fig. 6. Note that this is a simplified and two dimensional explanation. There are other effects that generate lift like vorticity and rotation effects. However, these effects are less prominent than the two effects mentioned above (e.g. Zeng et al., 2009).
In general, the forces causing inertial migration are known and understood. This allows for this phenomenon to be exploited in engineering applications. In microfluidics, inertial migration is used to precisely control the location of microparticles like cells. This application is called inertial focussing. Martel and Toner (2014) describe different fields where inertial focusing is applied. Depending on the parameters of the flow, the tubular pinch effect resulting from inertial migration may not be visible. If the system shows core-peaking behaviour instead, the inertial migration is dominated by shear-induced migration, which will be discussed in the next section.

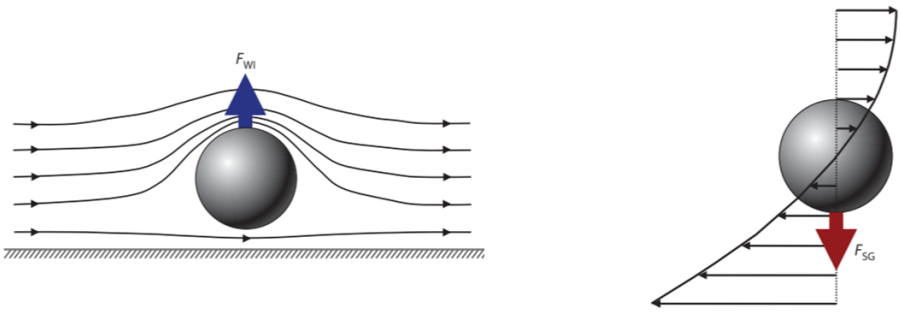

Figure 6: Inertial lift forces acting on a particle. Wall Induced lift on the left and Shear Gradient lift on the right. Adapted from Martel and Toner (2014)

2.3.3 Shear-Induced migration

Shear-Induced migration refers to the migration of particles to areas of the flow where the shear rate is lower. Fåhræus and Lindqvist (1931) described the change of the apparent viscosity of blood with the diameter of a capillary tube. For diameters smaller than 0.3 mm, the viscosity decreased with decreasing diameters. The authors argue that this is the result of red blood cells migrating to the centre of the tube, leaving a cell free layer near the walls which acts as a lubrication layer. This aligns with the findings of Karnis et al. (1966), Gadala-Maria and Acrivos (1980), and Leighton and Acrivos (1987) mentioned earlier in this chapter. While the presence of shear induced migration has been shown on numerous occasions, the physical reasons for this behaviour are not fully understood. Certain theoretical models have been developed, as will be discussed in the following section.

Theoretical models Following their experimental findings, Leighton and Acrivos (1987) developed a model based on irreversible particle-particle interactions. The following paragraph describes the details of their explanation. It should be noted however, that later research has disproven some of their hypotheses and shown that their resulting model is not universally applicable. Their explanation goes as follows:
If two perfectly spherical particles collide in a flow they will simply rotate around their contact point and

eventually return to their streamline. However, if the particles have a certain surface roughness or more than two particles interact at the same time the particles will undergo a net displacement. In a homogeneously distributed suspension flow with uniformly applied shear stress, the amount of particle interactions will be the same all throughout the flow. In this case the particles undergo a "random walk" and the concentration of particles will remain homogeneous. If there is a concentration gradient in the flow, the amount of particle interactions will be higher in the high concentration regions. This causes a net diffusion of particles to the lower concentration regions. The concentration gradient also causes a suspension viscosity gradient in the flow, which means that the particle interactions will on average cause a net displacement of particles to areas of low viscosity. This all would cause the particles to move from areas of high concentration to low concentration. However, a gradient in viscosity, together with a uniform applied shear stress, will lead to variations in the local shear rate. As a consequence of this, the amount of particle interactions will be greater in areas of lower viscosity and concentration, due to the higher shear rate. This will reduce the diffusion rate of particles into areas of low concentration. In flows with initially homogeneous distributions of particles but with non-uniform shear stress, the shear rate is also non-uniform. The movement of particles away from areas of high shear rate will also be present in these cases. The authors hypothesise that in their experiments, the shear-induced flux and the diffusive fluxes balanced each other out and converged to a steady state where the concentration of particles in the gap was low and in the reservoir it was high. They propose a model for this behaviour in the form of a diffusive flux equation. It is known as the Shear Induced Migration (SIM) model.
Later Nott and Brady (1994) show that the SIM model is not universally applicable. Even when the particles are perfect hard spheres, they undergo irreversible migration. They simulated a 2D suspension channel flow with Stokesian dynamics. The solid volume fraction range was $0.15 \leqq \phi \leqq 0.45$. They make use of the concept of suspension temperature which is a measure of the fluctuation velocity of the particles. They show that the suspension temperature does not reduce to zero at the centre of the channel where the shear rate is zero. This suggests a relationship between the shear rate and particle diffusion that is not linear, as Leighton and Acrivos (1987) suggested. They propose a different Suspension Balance Model (SBM) which includes mass, momentum and energy balances for the particle phase. They show that their model more accurately predicts their simulation results. Although some discrepancies are still present. They also introduce a characteristic time and length scale for the shear-induced migration based on the average distance a particle travels perpendicular to the main flow direction. They use this to explain the differences in the experimental result in previous investigations. They argue that certain authors did not find core-peaking behaviour because they measured at points where the flow was still developing. They propose the following scaling for the entrance length for dense suspension pipe flows

$$\frac{\mathcal{L}_{suspension}}{H} \sim \left(\frac{H}{0.5d}\right)^2. \tag{13}$$

Hampton et al. (1997) compared their MRI results to both the SBM and SIM model and concluded that they can both be used to predict the particle migration behaviour for a different subset of systems. For some flows, neither model predicts the behaviour well. Later, Nott, Guazzelli, et al. (2011) adjusted the SBM to address certain discrepancies. They mention other investigations where the SBM is applied successfully. Still, it is not universally applicable. Research into the underlying assumptions of this model is still ongoing (e.g. Jamshidi et al., 2021; Orsi et al., 2024). It should be noted that this adjusted version of the SBM is more complex, leading certain researchers to choose to apply older versions of it as was done by e.g. Mirbod (2016).

Experimental research Since the physical causes for shear-induced migration are not yet fully understood, research is still being done to try and further quantify this phenomenon. Of particular interest is the transition from a homogeneously distributed suspension to a core peaking flow. It is understood from previous research that the onset of core peaking behaviour will be influenced by the Reynolds number of the flow as well as the solid volume fraction and the particle size. Most investigations will vary either two or all three of these parameters within a certain range. The following section summarizes the results of a few of these investigations to give an overview of the current state of the research. It should be noted that the mentioned investigations only consider suspensions of neutrally buoyant spherical particles.
Han et al. (1999) used MRI to investigate the particle distribution in a neutrally buoyant suspension flow of varying solid volume fraction ϕ and Reynolds number. The particle size is kept constant at $d/D = 0.12$. The investigation is limited to low Reynolds numbers, the highest investigated particle Reynolds number flow was $Re_p = 0.376$ which is equal to $Re = 3.14$. The Reynolds number is based on the solvent viscosity and the average suspension velocity. They describe different combinations of ϕ and Re_p and present the radial velocity and concentration profiles. The volume fraction range investigated is $0.06 \leq \phi \leq 0.4$. They conclude that at very low Reynolds numbers of $Re_p = 0.05 \equiv Re = 0.42$ all flows show core peaking behaviour, regardless

of volume fraction. At the highest volume fraction $\phi = 0.4$ core peaking was always present and the velocity profile was blunted. For small volume fractions $\phi \leq 0.1$ and $Re_p \gtrsim 0.2 \equiv Re \gtrsim 1.7$ the particles showed the tubular pinch effect indicative of inertial migration. All other cases show some combination of these effects. Some show a concentration peak in the middle as well as halfway between the centre and the wall. Others show a concentration profile that peaks in the centre and then decreases to a plateau before dropping to zero at the wall. The velocity profile deviates from the single phase parabolic profile if there is a significant local concentration of particles. These results show that indeed, inertial migration does not present itself unless the flow has significant inertia and thus $Re \gtrsim 1$. They also show that for the particle size and volume fractions investigated, high Re is not required to induce shear-induced migration, the small shear rate differences are sufficient. This is consistent with the findings of Nott and Brady (1994) where the Stokesian dynamics simulations showed shear-induced migration.

Later, Hogendoorn, Breugem, et al. (2023) used both MRI experiments and Direct Numerical Simulations (DNS) to measure the concentration and velocity profiles in a suspension pipe flow, as well as the pressure drop. They investigated the flow at different ϕ and Re_s. The particle size is kept constant at $d/D = 0.058$. They defined three characteristic cases. In the first case, present in flow of low ϕ and high Re_s, the particle distribution is relatively homogeneous. For moderate ϕ the particles form a solid particle core in the centre of the pipe. For even higher ϕ the maximum packing fraction is reached in the centre of the pipe causing the solid particle core to expand towards the pipe walls. These volume fraction distributions are given in the left panel in Fig. 7. The horizontal dashed lines show the corresponding bulk solid volume fraction. On the top right, the regime map for the investigated flows is shown. The colour of the marker shows the ratio of the centreline volume fraction over the bulk volume fraction. There are dashed dotted lines separating the three cases. These are only a visual indicator as the available results do not suffice to fully define the transitions between the cases. Further research is needed to understand the nature of these transitions and when they occur. The bottom right panel in Fig. 7 shows the drag change of the flows with respect to the single phase cases with the same Re_s for increasing bulk volume fraction. It shows that the drag increases for low volume fractions and then decreases again as the volume fractions get higher. The authors hypothesise that these drag changes are caused by two opposing effects. In the case of low ϕ the particles are distributed homogeneously throughout the flow and thus interact with the walls. This creates added friction as the particles at the wall effectively increase the pipe roughness that the flow experiences. As ϕ increases, the core peaking behaviour of the particles creates a layer free of particles near the wall. This causes a large radial gradient of local effective viscosity. This lower viscosity, particle free layer acts as a lubrication layer.

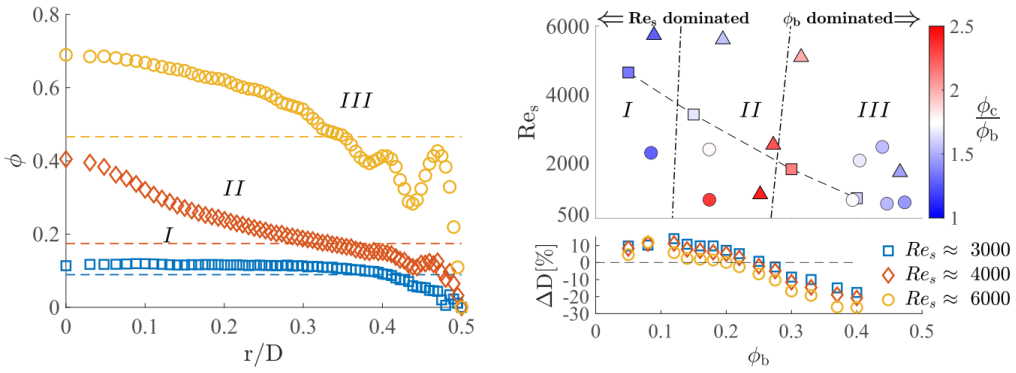

Figure 7: The three representative cases of particle laden flows as defined by Hogendoorn, Breugem, et al. (2023). On the left the measured volume fraction distributions are shown by the markers and the constant bulk volume fraction is shown by the horizontal dashed lines. On the top right the regime map is shown where the circular and triangular markers show the author's own results and the square markers, connected by a dashed line, show results from a numerical investigation by Ardekani et al. (2018) for a similar flow. The colour of the markers represents the ratio of the centreline ϕ to the bulk ϕ. The dashed dotted lines separate the results into the three cases. On the bottom right the drag change is shown for increasing bulk volume fraction with respect to single phase drag. Reproduced from Hogendoorn, Breugem, et al. (2023)

Drag variation The pressure drop variation described by Hogendoorn, Breugem, et al. (2023) shows that suspension viscosity models like Eilers' are not sufficient for predicting the drag of suspension pipe flows because

they do not capture the local variation in volume fraction. They are only based on the bulk volume fraction. On top of this, the size of the particles is not taken into account either in these models. Costa et al. (2016) used DNS data to verify that the continuum approach of suspension viscosity models does not accurately capture the behaviour of particle laden flows. They show that in the near wall region the particle-wall interactions impact the velocity profile. The particles form a particle-wall layer which prevents the bulk flow from interacting with the wall directly. The authors theorize that these flows can be modelled accurately by treating the near wall layer and the rest of the flow separately. Within the bulk flow the continuum approach of suspension viscosity models is applicable. For the wall layer the dynamics are modelled differently. They derive a drag law that accurately predicts the drag for the investigated suspension flows. Later however, Leskovec et al. (2024) showed the shortcomings of suspension viscosity models as well as the model created by Costa et al. (2016) in the prediction of drag. They used MRI and DNS to study the drag change for suspension flows of different particle sizes, volume fractions and Reynolds numbers. They found that neither Eilers' model nor the particle-wall layer theory could accurately predict the friction factor for all systems investigated. They show that all three variables that were altered had a significant impact on the friction factor. They identify two mechanisms that the particle-wall layer theory does not account for. Firstly the migration of particles towards the centre of the pipe which invalidates the assumption that a constant effective viscosity can be used in the core of the flow. Secondly the slip velocity between the fluid and the particles when the particles are large. This inertial effect between the particles and the fluid cannot be captured by a continuum model alone. The authors propose ways in which the particle-wall layer theory could be extended to account for these effects. Using all of their experimental data they create a master curve which can be used to predict the friction factor of a particle laden pipe flow. They test the application of this master curve with two experimental cases from Hogendoorn, Breugem, et al. (2023). For one of them the prediction and the measured result are very close but for the other, the prediction is quite far off from the measured result. The authors conclude that more experimental results could be used to strengthen the estimates of the master curve.
Leskovec et al. (2024) also show that the radial concentration profiles for two flows of the same Re_s and ϕ, but with different d/D, can be quite different. In their example, larger particles show more significant core peaking behaviour than smaller particles. This suggests that the regime map on the top right of Fig. 7 would look quite different for a flow with different d/D.

2.4 Measurement methods

Investigations into suspension flows are done in many different ways. All different methods have advantages and disadvantages and will provide different data and insights. The decision for which method to use is influenced by many different aspects. For example, if a specific physical quantity is of interest, this informs the choice of method. On top of that, financial and time constraints can come into play. Lastly some investigations may specifically set out to test the applicability of a certain method if this has not yet been verified. The following sections will list and compare certain methods which will lead to a method choice for this thesis.

2.4.1 Comparing experimental and computational investigation

Theoretical investigations can further the understanding of the causes of shear-induced migration. Doing this research effectively however, requires knowledges of how and when shear-induced migration presents itself, depending on different factors. The research that is done into the impact of these factors can be put into either of these two areas, experimental or computational. Experimental investigations consist of an experimental setup with an actual suspension flow loop at its core. This is paired with sensors and transducers to measure certain physical quantities and acquire the desired data. Computational methods instead use simulations to investigate suspension flows. There are many different types of computational fluid dynamics (CFD) simulations. Because of the complexity of suspension flows and the importance of small scale phenomena, current computational investigations tend to use direct numerical simulations (DNS) (e.g. Costa et al., 2016; Hogendoorn, Breugem, et al., 2023; Leskovec et al., 2024). Instead of modelling turbulence, as is done in other CFD methods, DNS numerically solves the Navier-Stokes equations down to very small spatial and temporal scales so that turbulence is entirely resolved. One of the main advantages of computational methods over experimental research is that they generate field data for all flow properties like velocity and pressure, as well as derived properties like vorticity. For experimental methods, the information gained is much more limited. DNS of course still has drawbacks. Firstly, because DNS requires high spatial and temporal resolution, running a simulation is a resource-intensive and time consuming process. Especially if multiple different flow variations are to be simulated. Secondly, even though the spatial resolution is very small, when particles approach each other, the liquid film between the particles becomes smaller than the simulation cell size. This means that the flow in these areas cannot be fully resolved and these effects need to be modelled. This introduces an uncertainty

in the results. Thirdly, because turbulent flow and particle displacement are chaotic, simulation results are dependent on the initial conditions. Especially when the computational domain is small and has periodic inlet and outlet conditions, the statistics of the results are influenced by the initial conditions. This is often the case for suspension flow DNS.

2.4.2 Available experimental techniques

When it comes to experimental investigations, the available measurement techniques are plenty. However, some experimental techniques that are common in fluid dynamics research are not applicable to suspension pipe flows. For example, Particle Image Velocimetry (PIV) and Laser Doppler Velocimetry (LDV) require the flow to be transparent. The presence of particles in suspension flows makes these methods hard to apply. Their application is generally limited to low volume fraction cases as was done by Hogendoorn, Chandra, et al. (2021). Alternatively the particles could be made of transparent material. If the refractive index of the working fluid is then matched to that of the particles, the flow is fully transparent (e.g. Snook et al., 2015). This still has drawbacks as the tracer particles used for these methods are only present in the liquid phase. This means that only the velocity field of the liquid phase can be measured. On top of that, the particles being invisible makes it difficult to evaluate the flow visually. An advantage of PIV and LDV is that the displacement results can be used to generate not only the velocity field but also the vorticity and pressure fields in the liquid phase. These results are quasi-instantaneous.
A different method that may be used is Ultrasound Imaging Velocimetry (UIV). Here, an ultrasound transducer is used to create an image of a 2D slice of the pipe. The ultrasound image shows peaks at the positions of the solid particles. The raw images can be used to measure the concentration profile in the flow. Additionally, applying correlation algorithms to these images, similar to PIV, can generate the velocity field of the particle phase. UIV is a relatively novel method that has certain drawbacks. For example, Dash et al. (2022) describe how attenuation puts limits on the volume fraction, penetration depth and time resolution of UIV. On top of this, the difference in the speed of sound in the liquid and the solid phase causes an uncertainty in the measured position of the particles. These limits mean that UIV can only reliably be used to measure time averaged velocity and concentration profiles.
X-ray techniques are also used to characterise multiphase flows. X-ray imaging can be used to create volume fraction contours of gas-liquid and solid-gas systems (Aliseda and Heindel, 2021) and of flowing suspensions (Gholami et al., 2018). It can also be used to study the microstructure of particle suspensions (Deboeuf et al., 2018). Velocity information can also be gathered through X-ray particle tracking velocimetry (XPTV) (Aliseda and Heindel, 2021). X-ray imaging is based on density differences which means that in a neutrally buoyant flow with particles made of a single material, it cannot be used. A potential solution to this is using particles that have a dense core encased by a lighter material as was done by e.g. Seeger et al. (2001) who used polyurethane foam particles with lead inserts. A major drawback of X-ray techniques is that it uses ionising radiation. Additional safety measures are required to conduct these experiments safely.
A technique that is well suited to suspension pipe flow research is Magnetic Resonance Imaging (MRI). Multiple aforementioned investigations (Hogendoorn, Breugem, et al., 2023; Han et al., 1999; Leskovec et al., 2024) make use of MRI. MRI can be used to measure concentration profiles as well as time averaged and instantaneous three dimensional velocity fields. The concentration measurements are based on the difference in signal magnitude between the liquid and solid phase. In the mentioned investigations, the particles don't create a signal at all because they contain a very low amount of hydrogen nuclei. This means that the measured signal intensity in a voxel is directly correlated to the local volume fraction. MRI can thus be used to measure the concentration field instantaneously, but the time averaged field is of more interest. There are different ways to measure velocity fields with MRI. All the above cases made use of phase-contrast MRI. This method can be used to generate instantaneous and time averaged velocity fields. It should be noted that because this methods uses the phase shift of the resonating hydrogen nuclei, the resulting velocity field is the velocity of the fluid phase only.
When researching any kind of pipe flow, the pressure drop is also an important factor. A simple way to measure this is with a differential pressure sensor, connected to two points in the pipe at different axial positions, as used by e.g. Hogendoorn, Breugem, et al. (2023). The pressure measurement can then be used to calculate the friction factor of the flow using eqs. 2 and 3.

Camera imaging is another relatively simple method that can also be used to capture the behaviour of suspension pipe flows. Which information can be accessed by a camera is dependent on the camera's capabilities like frame rate, resolution and dynamic range as well as the setup of the experiment considering e.g. lighting. The aforementioned method PIV is technically also a camera imaging method, but it requires very specific circumstances like the presence of tracer particles and the use of a laser for illumination. The desired result of PIV is also not the camera images themselves but the displacement fields based on the image pairs. To

distinguish from this, the term camera imaging is here used to describe any experiment where a camera takes images of the unaltered flow and these images themselves are the desired result. This technically includes methods like shadowgraphy and schlieren imaging. These methods capture the changes in the refractive index of a fluid, for example caused by changes in density (e.g. Tropea et al., 2007). However, these methods cannot be applied to suspension pipe flows as there are no sharp density gradients in the liquid due to the absence of shockwaves and temperature gradients. Camera imaging in this sense thus cannot be used to obtain any information about the fluid phase as it is transparent and there are no significant changes in fluid density that impact the refractive index. It can however, be used to investigate the particle phase. If the suspension is lit from the same side as the camera, images can be used to investigate the size and shape of particles. Trajectories of single particles can also be measured under certain conditions. Camera measurements can also be used to measure the local concentration of particles in low concentration through particle counting. It can potentially also be used at higher concentrations by backlighting the setup and measuring the loss of light intensity due to the particles present.
This is not an exhaustive list of experimental techniques but an overview of the most applicable, common and non-intrusive methods that may be used to gather velocity, pressure and concentration data about suspension pipe flows.

2.4.3 Choice of method

As shown in the previous sections, one of the most extensive approaches to suspension pipe flow research is a combination of MRI, differential pressure sensors and DNS. This type of approach is very valuable as the experimental measurements give insight into the 3D velocity and concentration fields as well as the friction factor. The numerical simulations give even more detailed results which can be directly validated with the experimental results. A major drawback of this method however, is the time and money it costs to perform these experiments and simulations. It is worthwhile to research other methods that are quicker and less expensive. Since other numerical methods require the modelling of certain physical behaviours, which introduces uncertainties, their use for fundamental research into the behaviour of suspension pipe flows is limited. Any numerical results will have to be validated with experimental data, either new or from literature, before conclusions can be drawn. On top of that, other CFD methods are still time consuming.
Most of the aforementioned experimental methods are more accessible than MRI. However, all of them have their own drawbacks. PIV and LDV are mainly applicable for low ϕ and do not gather particle concentration information. UIV in its current state only generates reliable time averaged velocity and possibly concentration fields. X-ray techniques require extensive safety precautions and camera measurements can not generate velocity fields.
Since one of the goals of this research was finding an experimental technique that is affordable and easily accessible, camera imaging was chosen as the technique to research further. It is in principal much easier to use than the other mentioned methods since it does not require any lasers, ionising radiation, ultrasound transducers or other specialised equipment apart from the camera itself. Camera measurements can potentially be used to measure the particle concentration in the suspension pipe flow. By placing an LED panel on the opposite side of the flow from the camera, the measured light intensity should be proportional to the amount of particles between the light source and the camera. Based on the knowledge that the migration behaviour in neutrally buoyant suspensions is axisymmetric, the measurements can in theory be used to generate a time averaged 3D concentration profile. In tandem, a differential pressure sensor can be used to measure the pressure drop. This combination of pressure drop and concentration data can then be used to characterise a suspension pipe flow at different volume fractions and create a visualisation similar to Fig. 7. It should be noted that this technique has not been applied extensively in this type of research. However, if the results are sufficiently reliable, this technique could be used instead of MRI measurements for concentration gradients. It cannot fully replace MRI since camera measurements cannot generate velocity data. Instead it could potentially be used to quickly generate concentration gradient data to identify interesting cases, to be studied later with MRI.

Light attenuation measurements The measurement method described in the previous section is based on the idea that the camera will be able to measure the reduction in light intensity caused by the presence of the solid, opaque particles. This same concept has been used in different measurement methods which have given rise to different empirical laws. One of the most common is the Beer-Lambert law which is used, for example, in spectrophotometry. Spectrophotometry is a method of measuring the concentration of a chemical in a liquid by illuminating it and measuring the transmitted light intensity. Different molecules absorb light at different wavelengths and at different rates. The Beer-Lambert law is used to find the concentration from the measured

intensity. It is defined as (Hollas, 2004)

$$A = \varepsilon c \ell \tag{14}$$

where ℓ is the optical path length, c is the molar concentration of the specific chemical in the analyte, ε is the molar absorption coefficient of the species, which is a function of the lights wavelength, and A is the absorbance. The absorbance is defined by the initial light intensity I_0 and the measured, attenuated intensity I as (Hollas, 2004)

$$A = \log_{10} \frac{I_0}{I}. \tag{15}$$

Alternatively the absorbance can be defined with the transmittance $T = I/I_0$. The measured intensity will thus follow an exponential function,

$$I = I_0 10^{-\varepsilon c \ell} = I_0 e^{-\alpha \ell} \tag{16}$$

where $\alpha = \ln 10 \ \varepsilon c$ is the Napierian absorption coefficient. Apart from spectrophotometry, the Beer-Lambert law is successfully applied in different radiation absorption experiments and in astronomy. In certain situations however, the measured behaviour deviates from the Beer-Lambert law. Significant research has been done on the different types of deviations that present themselves. Kiteto and Mecha (2024) discuss the three different classes of deviations. Firstly fundamental deviations, which are related to the inherent limitations of the Beer-Lambert law. The law, for example, assumes that there are no interactions between the molecules. Mayerhöfer et al. (2020) explain that at higher concentrations, molecular interactions do come into play. These interactions impact the absorption cross-sections of the molecules. This means that the molar absorption coefficient is in fact a function of concentration. This causes the relationship between the concentration and the absorbance to no longer be linear. The Beer-Lambert law also assumes that the only cause of light attenuation is absorption. In practice, light is also scattered. At low concentrations and with certain measurement geometries, the impact of scattering is minimal and can be ignored. It is sometimes possible to replace the molar absorption coefficient with an extinction or attenuation coefficient (Q) that combines the effects of scattering and absorption. It is then no longer possible to measure the absorbance, instead the attenuation (A_t) is found from the intensity loss. When the Beer-Lambert law is applied to colloids and suspensions or other highly scattering media, this approach often results in deviations from the expected linearity. This is due to multiple scattering behaviour which can be a function of the concentration or the path length (e.g. Kocsis et al., 2006). This means the attenuation coefficient is no longer a constant but itself a function of the concentration or path length.
The second class of deviations are chemical deviations. These deviations are relevant for example for analytes that are in a chemical equilibrium which changes with the surrounding environment, like the pH. The third class of deviations are instrumental deviations. These are deviations caused by flaws in the experimental setup when not all the assumptions of the Beer-Lambert law are taken into account. For example, the Beer-Lambert law assumes that the light source is monochromatic. Since the molar absorption coefficient of the analyte often differs for different light wavelengths, using polychromatic light, together with a sensor that cannot distinguish different wavelengths, will cause a negative deviation. Another added deviation can occur when there is extraneous light coming into the detector. This causes a constant positive offset to the measured intensity, resulting in a negative deviation of the absorption from the Beer-Lambert law.

It is clear that the Beer-Lambert law as presented in Eqs. 14 to 16 is only applicable under stringent conditions. However, Eq. 15 can be used in any situation if the absorption is replaced with the attenuation and the molar absorption coefficient is replaced with an attenuation coefficient. A careful calibration of the measurement system using analytes with known concentration can be used to measure the intensity profile, which can be used to create a model similar to Eq. 16, specific to the system. The most simple models are those for systems where the attenuation remains a linear function of concentration and optical path length. An example of this is given by Xu et al. (2005) who created two models for the attenuation of light in a partially mixed estuary. They defined different attenuation coefficients for different dissolved and suspended substances, in two different salinity ranges. Even though the models contain different attenuation coefficients and different concentration values, the models are still linear and thus resemble the Beer-Lambert law quite closely. For systems that show non-linear attenuation, the models differ from the Beer-Lambert law more significantly. For example, Acién Fernández et al. (1997) found that in the case of a photobioreactor for microalgae illuminated by sunlight, the measured intensity profile followed a hyperbolic path instead of an exponential one. They explain that the the deviation from the Beer-Lambert law is due to the different scattering effects and selective absorption of polychromatic sunlight that occur at high biomass concentrations. They instead propose a hyperbolic model that fits their data. The review by Kiteto and Mecha (2024) contains multiple additional examples of modifications to the Beer-Lambert law in situations where the attenuation is not a linear function of concentration or path length.

While the aforementioned examples are useful for specific systems, efforts have also been made to generalize some of these models so that they are applicable to a wider range of systems. For example, Casasanta and Garra (2018) expand the Beer-Lambert law so that it can also be applied to systems experiencing hyperbolic extinction as well as sub- and super-exponential extinction. They explain that, from a statistics point of view, the Beer-Lambert law assumes that the extinction events in a test sample follow a Poissonian distribution. This does not apply in situations where there is a spatial correlation between the obstacles. If there is a positive correlation, the extinction will be sub-exponential and vice versa. These systems are modelled by a weighted Poisson distribution instead. They then argue that hyperbolic extinction is a result of inhomogeneity in the medium and they incorporate this into their model.
On top of deviations due to physical and chemical phenomena that are unaccounted for, deviations may also come from incongruencies with electromagnetic theory, as explained by Mayerhöfer et al. (2020). They explain that in the case of transflection measurements, where a small film of the test sample is placed on top of a highly reflective substrate, the reflected lightwave can interfere with the outgoing one. This causes the electric field intensity to be a function of the position within the sample, which means that the absorption also varies. The interference pattern will change with the thickness of the sample which means the measured absorption spectra will not be linear functions of the sample thickness, as Beer-Lambert would suggest. They also discuss the concentration dependence of the molar absorption coefficient. They compare the Beer-Lambert law to the ideal gas law as they are both limiting laws that are only applicable under certain stringent conditions. The authors even propose renaming the Beer-Lambert law to ideal absorption law to emphasise this.
For this thesis, it is useful to anticipate the most likely sources of deviations from the Beer-Lambert law that will be encountered. Preliminary measurements that were done on the existing test setup showed that the absorbance had a negative deviation from Beer-Lambert. The setup was then adjusted to eliminate the amount of extraneous light reaching the camera but the negative deviation remained. As mentioned before, a negative deviation can occur when a polychromatic light source is used for the experiments. This is then a result of the wavelength dependence of the attenuation coefficient. In the case of these solid polystyrene particles however, this is unlikely to be the cause of the deviation. If the particles absorbed and scattered visible light of different wavelengths at different rates, they would not be white. The use of a monochromatic light source or a colour filter in front of the sensor is thus not going to impact the measured deviation. A more likely source of the deviation is the interaction of the particles. At high concentrations, the particles cast shadows on each other. Any particle that is shadowed by another particle experiences a lower light intensity than the source intensity. This means that the shadowed particle can attenuate less light than if it were not shadowed. Additionally, multiple scattering is also likely to happen which can cause the attenuation to be a function of the optical path length (e.g. Bhatt et al., 2016).
It is also important to keep in mind that the Beer-Lambert law assumes that the attenuating species are molecules. Measuring the concentration of micro-particles through light attenuation measurements requires the use of modified models (e.g. Acién Fernández et al., 1997). Different investigations have also been done into the impact of particle size on the attenuation of light (e.g. Baker and Lavelle, 1984; Markova et al., 2021) but these are also often limited to micro-particles. In these cases the particle size is similar to the wavelengths of the radiation used. It is possible that the behaviour of macro-particles will be different from suspensions of micro-particles. A benefit of the particles used in this thesis is that they are monodisperse, meaning that a possible size dependence of the attenuation coefficient will not be present.
Considering all this, it is expected that an empirical relationship, analogous to the Beer-Lambert law, can be found for the attenuation as a function of the particle concentration in the pipe flow. The starting point for this relation will be the following equation,

$$\log_{10} \frac{I_0}{I} = A_t = Q\phi_s\ell \tag{17}$$

where At is the attenuation and Q is the attenuation coefficient which is likely to be a function of either ϕ_s or ℓ and possibly both. Here the solid volume fraction is used instead of the molar concentration as this is more applicable in the context of suspensions. It should be noted of course that the volume fraction and molar concentration are simply different ways of conveying the same information. To find the correct form of Q, intensity profiles will have to be measured at varying ϕ_s and ℓ. If a relationship like Eq. 17 can be found, it can be used to find the volume fraction distribution for any combination of Reynolds number and bulk volume fraction with camera imaging. It should be noted that the measured volume fraction distribution is a 2D projection of the 3D system. However, because of the axisymmetric nature of the neutrally buoyant flow, this projection can be used to reconstruct the 3D distribution with tomographic reconstruction. It should be noted that readily available tomographic reconstruction methods like the filtered back projection assume exponential attenuation. To apply these methods to the present research, adjustments will have to be made depending on the experimental findings.

2.4.4 Proposed experiments

The goal of the first experiments is to calibrate the setup and find an attenuation equation as described in Eq. 17. The proposed setup is shown in Fig. 8. The test section of the pipe will sit in a box filled with the suspending liquid. This is done to combat the distortion of the images that would otherwise be present due to the refraction of the cylindrical pipe. Experiments will be done at known bulk volume fractions and at high Reynolds numbers to ensure homogeneous particle distribution at the test section. To verify the homogeneous distribution of particles, average intensity profiles will be measured at different Reynolds numbers. If the profiles do not change with the Reynolds number, it can be assumed that the particles are homogeneously distributed for all Reynolds numbers measured.
As both ϕ and ℓ can impact the attenuation coefficient Q, their impact should be assessed separately. This will be done by first studying only the intensity loss at the centreline of the pipe, shown in Fig. 9. This ensures that the optical path length remains constant while the volume fraction can be varied. It should be noted that for these measurements the homogeneous distribution of the particles is less important. Whether or not the suspension experiences core peaking, the total amount of particles between the light source and the camera at the height of the centreline will remain the same. This is illustrated in Fig. 10. Once the impact of the volume fraction at this constant optical path length has been found, the 2D intensity profiles can be used to assess the influence of ℓ. Here, the homogeneous distribution of particles is crucial to ensure that the volume fraction is constant with varying path length, illustrated in Fig. 10. This figure also shows the optical path length for a measurement point above the centreline. The optical path length in these experiments is not the distance between the light source and the camera but the distance that the light travels through the suspension in the pipe. This means that the optical path length is always equal to the horizontal distance between the inner sides of the tube at the height of the measurement. The optical path length thus varies from zero at the top and bottom of the pipe to D at the centreline.
An intensity measurement without particles should be made every now and then to ensure the value of I_0 is still accurate. This can be done by covering the pump entrance with a sieve. This will keep the particles in the reservoir while the fluid can flow freely. The volume fraction should also be verified during experiments. The overall bulk volume fraction is of course defined when preparing the suspension. The exact weight of the solution and the added particles is known and recorded. Since the suspension is neutrally buoyant, the volume fraction and weight fraction are the same. If, however, some of the particles accumulate somewhere in the flow loop, the volume fraction travelling through the test section may be lower. This can be assessed by finding the solid volume fraction of a sample of the suspension collected from the outflow. At very low volume fractions, particle counting can be used to find the solid volume fractions. This is likely only applicable at $\phi_s < 0.01$.

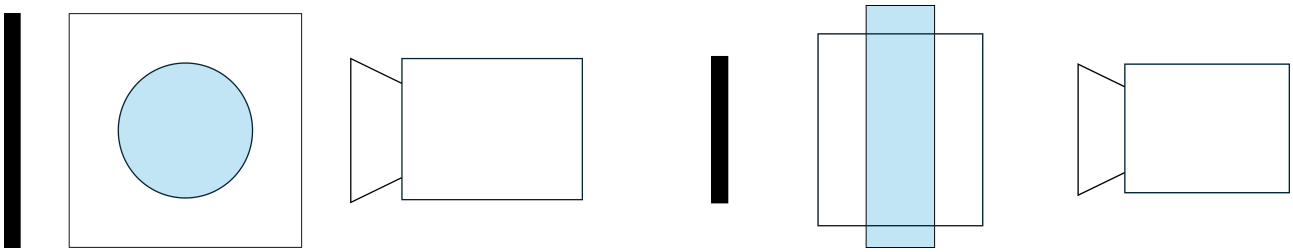

(a) Side view (b) Top view

Figure 8: Schematic representation of the experimental setup with the camera on the right and the light panel on the left in black. In the middle, the test section of the pipe is shown in light blue, surrounded by the box with liquid that will prevent refraction from the tube.

2.5 Conclusion

It is evident that particle migration is still a topic of active research. Where the physical reasons for inertial migration are generally understood and exploited, the cause of shear-induced migration is still partly a mystery. What is clear is that the rate of migration is influenced by the Reynolds number, volume fraction and particle size. The rate at which they impact migration is not yet fully defined. It is also known that the particles migrate away from areas of high shear rate due to particle-particle interactions. The reason these interactions cause displacements in a preferred direction is still a topic of research. These knowledge gaps currently make it impossible to accurately predict the particle distribution in a suspension pipe flow. This in turn means that

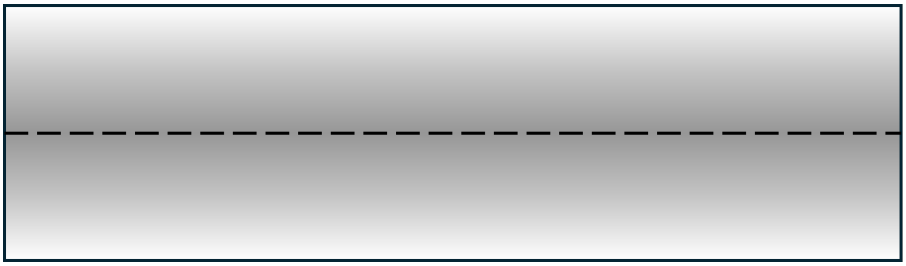

Figure 9: Schematic representation of an intensity profile. A dashed line represents the centreline.

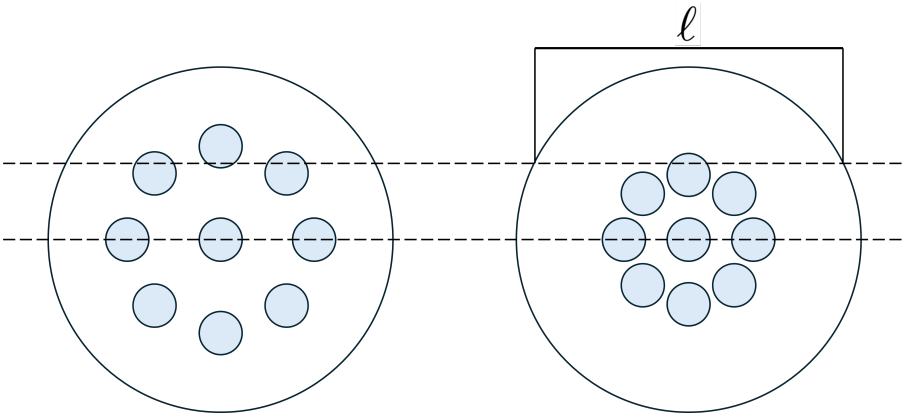

Figure 10: Schematic representation of a suspension pipe flow with different levels of core-peaking. The blue circles represent the particles. The dashed lines show that more significant core peaking does not impact the amount of particles that are measured at the centreline. Core peaking does change the amount of particles present at horizontal lines above or below the pipe centre. The optical path for the higher horizontal is shown at the top right.

existing suspension viscosity models like the Eilers' model cannot be used to make accurate predictions of the friction factor of suspension pipe flows, as they assume homogeneity. The goal of this thesis is to develop an experimental method and use it to study suspension pipe flows undergoing shear-induced migration. More specifically, the investigation focusses on the use of light attenuation measurements with a camera to measure the concentration gradient in a suspension pipe flow at different bulk volume fractions and Reynolds numbers. The particle size will be kept constant throughout the investigation to limit the amount of variables influencing the light attenuation coefficient.
As for light attenuation measurements, it is known that the Beer-Lambert law only holds under stringent conditions which cannot be met for suspensions of macro particles. In many other situations where the Beer-Lambert law is not directly applicable, it is possible to generate a model for the attenuation of light through careful calibration. Measuring the intensity profiles at different concentrations and optical path lengths makes it possible to generate an attenuation coefficient for these systems. Although a model like this was not found in the literature for a suspension of particles in the millimetre size range, the hypothesis is that it is possible to generate such a model for the existing experimental setup, as discussed earlier in Eq. 17 and surrounding text. These knowledge gaps give rise to the following research questions for this thesis.

Can light attenuation measurements be used to measure accurate volume fraction distributions? It is evident that the measured light intensity will diminish when there are more particles in between the light source and the sensor. This means that the volume fraction distribution in the flow can be measured with this camera setup. What is uncertain however, is how accurate the results are. For example, if the results are accurate down to $\phi = \pm 0.01$, camera measurements can be used to characterise a flow in a similar manner to the top-right panel of Fig. 7. If the results are even more accurate, they can be used to construct radial distribution profiles similar to the left panel of Fig. 7. If they are much less accurate than $\phi = \pm 0.01$, the results may still be useful for distinguishing between core-peaking and non-core-peaking flows. This thesis should foremost answer the question if the proposed measurement method can be used to measure volume fraction distributions with an accuracy that is sufficient for the qualification of flows as core-peaking. If this is the case, the following question is, can the measurements also be used to generate a regime map or even radial distribution profiles?

What do the transitions from homogeneously distributed to core-peaking flow look like? This question can only be answered if the camera measurements are good enough to measure local volume distributions accurately. The aforementioned three representative cases defined by Hogendoorn, Breugem, et al. (2023) are very distinct but the transition from one case to the next has not been measured yet. If the light attenuation measurements can be made with sufficient accuracy it will be possible to capture the transition behaviour. If the transitions are sudden, a border between the cases can be defined. It should be noted that this will require a lot of measurement data and it may not be possible to fully answer this question due to the time constraints of this thesis, even if the camera measurements are of appropriate quality.

What is the relationship between the drag change of the flow and the volume fraction distribution? If time allows it may be possible to research the relationship between the core-peaking behaviour and the drag change of suspension flows. The current hypothesis is that the Eilers' model fails when the suspension flow is no longer homogeneous and that the presence of a particle free lubrication layer causes a drag reduction. If the camera measurements are sufficiently accurate, they can be combined with pressure drop measurement to investigate if the deviation from Eilers' indeed lines up with the core-peaking of the flow. It should again be noted that time constraints may prevent this question being answered during this thesis.

If this measurement method can be used to accurately measure the volume fraction distributions in this suspension pipe flow, it can be a precedent for future research. It will allow for faster investigation of the impact of different parameters on the volume fraction distribution in suspension flows. This will lead to a better understanding of the impact of these parameters on the shear-induced migration of particles as well, which can aid in the creation of new models.

3 Methods

To answer the posed questions, in the end two separate experimental setups were needed. In the first place a pipe flow setup is of course necessary to study the particle migration behaviour in a neutrally buoyant suspension pipe flow. However, calibrating the attenuation for known volume fraction and path length as described in section 2.4.3 deemed more difficult than anticipated. Instead, a separate calibration setup was created. This section will first discuss the pipe flow setup and why calibration in this setup was avoided, followed by a discussion of the calibration setup. Finally the data processing steps are explained.

3.1 Experimental pipe flow setup

A schematic of the main experimental setup is shown in Fig. 11. The suspension consists of unexpanded polystyrene particles with an average diameter of $d = 1.3$ mm and the suspending liquid is a mixture of water and glycerol. The intended use for these particles is the manufacturing of expanded polystyrene objects. This means the particles are porous and contain enclosed gas pockets, which causes them to be polydisperse in density. The important part of this flow loop is the pipe section, which starts at the flow conditioner. This flow

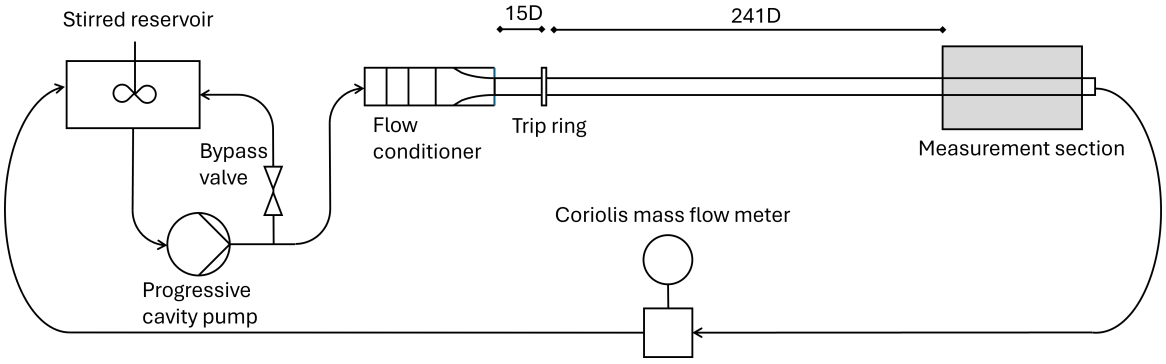

Figure 11: A schematic overview of the flow loop used for the pipe flow experiments. The measurement section consists of the camera setup shown in Fig. 12

conditioner consists of a 60 mm inner diameter cylinder with three dispersion plates inside. These perforated plates intend to properly mix the suspension before it enters the pipe section of the setup. After the dispersion plates the flow converges into the transparent acrylic pipe with a diameter of $D = 20$ mm. This means that for these experiments $d/D = 0.065$. After a distance of $15D$, the flow encounters a trip ring with an internal diameter smaller than the pipe diameter. This ensures that the flow is disturbed and that the turbulence transition happens at a consistent Re_s. After a distance of $241D$ the suspension flows through the measurement section, the details of which will be discussed later. The development length of suspension pipe flows displaying shear induced migration is not generally known. However, we can use the scaling from eq. 13 and the knowledge that Hogendoorn, Breugem, et al., 2023 found that an entrance length of $132D$ was sufficient in their case. Since Nott and Brady, 1994 mention that the scaling analysis resulting in eq. 13 is also applicable to different flow geometries we can rewrite eq. 13 to

$$\left(\frac{\mathcal{L}}{D}\right) \sim 4\left(\frac{d}{D}\right)^{-2}. \tag{18}$$

Since Hogendoorn, Breugem, et al. (2023) used a setup where $d/D = 0.058$, the above equation tells us that the relevant entrance length scales with $\mathcal{L}/D \sim 1189$. However, they found that their measurements done at a distance of $132D$ from the entrance were fully developed. This suggests that relationship between the scaling for the entrance length and the actual sufficient entrance length is

$$\frac{\mathcal{L}}{D} \leq 0.11\left(\frac{\mathcal{L}}{D}\right)_{sc} \tag{19}$$

where $(\mathcal{L}/D)_{sc}$ is the scaling for the entrance length as defined in eq. 18. Since the current setup has $d/D = 0.065$, eq. 18 tells us that $(\mathcal{L}/D)_{sc} = 947$. This means that

$$\frac{\mathcal{L}}{D} \leq 0.11\left(\frac{\mathcal{L}}{D}\right)_{sc} = 104 \tag{20}$$

which means that the flow is indeed fully developed at the measurement section which sits at $241D$ from the trip ring. It should be noted that eq. 18 is a simplified version of the scaling law that is applicable at high solid volume fractions ($\phi > 0.3$). For lower volume fractions, the constant value on the right hand side, which is now four, may be different. Furthermore, this scaling law was based on Stokesian dynamics simulations. It is known that for flows outside the Stokes regime, the particle migration behaviour is also dependent on Re_s. It is therefore likely that the entrance length is also dependent on Re_s. This means that, while the entrance length is still dependent on d/D as well, eq. 18 is not a sufficient scaling for it. However, since Hogendoorn, Breugem, et al. (2023) noted that all their identified cases were fully developed. All the volume fractions and suspension Reynolds numbers that will be investigated here are within the same range that they investigated. The only difference with their experiments is thus the relative particle size d/D. The above justification quantifies the impact of this difference on the entrance length and is therefore sufficient to conclude that the current entrance length is adequate for fully developed shear induced migration.

The suspension in the reservoir is continuously stirred by an IKA RW28 overhead stirrer. This should ensure that the suspension stays properly mixed. The reservoir is covered by plastic sheets during measurements to reduce the amount of evaporation that happens. The flow is generated by an AxFlow Mono C2XA progressive cavity pump. A bypass valve is used to control the flow speed through the pipe section, in tandem with the variable speed of the pump. This approach allows the pump to produce low flow speeds in the measurement section while still running at a relatively high frequency, creating a more stable flow. Keeping the bypass valve partially open at all times also acts as a safety measure. If the particles were to cause jamming anywhere in the pipe section, the flow would simple be rerouted through the bypass. This prevents high pressure spikes due to blockages. The flow that returns to the reservoir passes through a Krohne Optimass MFM 7050K T15 Coriolis mass flow meter. It measures the mass flow rate and the suspension density, from which the volumetric flow rate is found.

To prepare the setup for experiments it is first filled with a mixture of water and glycerol. These two components are mixed in a ratio such that the resulting liquid will have the same density as the particles. The density of this mixture was found using a pre-existing Matlab script that uses the Matlab function created by Volk and Kähler (2018), which also calculates the viscosity. The particles are polydisperse in density so obtaining an exact match of solid and liquid density is an iterative process. The average density of the particles is known from prior experiments to be 1 036 kg/m^3. Additionally, the available glycerol in the lab is already a mixture of glycerol and water. Even though the manufacturer specifies that it contains 86% glycerol, this ratio was found to vary, likely due to mistakes during manufacturing or in the lab. This means that the calculated density of the liquid may not be accurate, as the mass fractions of water and glycerol may be off. This is another reason

that proper density matching is an iterative process. After the initial liquid mixture is made and mixed by running it through the setup for a while, a small amount of polysorbate 20 is added. This is a colourless liquid surfactant, which is used to ensure the particles are properly wetted. Afterwards, particles are added to obtain the lowest desired bulk volume fraction ϕ_b. The system is mixed by running the pump again and then stopped. When the flow stops, all particles will either settle or float depending on their density. When about half the particles in the pipe float and the other half sink, the system is deemed neutrally buoyant. Small amounts of either water or glycerol may be added to obtain this. If necessary, more particles are added again to re-attain the desired ϕ_b. The necessary mass of particles to add can be calculated as

$$\phi_b = \frac{M_p}{M_p + M_l} \tag{21a}$$

$$M_p = \frac{\phi_b M_l}{1 - \phi_b} \tag{21b}$$

where M_p is the mass of particles and M_l is the total mass of the liquid. For each subsequent measurement the amount of particles added was M_p for the next value of ϕ_b minus the already present amount of particles. Using this method does mean that the experiments were done in ascending order of ϕ_b. This is not ideal from an experiment-design point of view as this makes it almost impossible to distinguish between systemic errors that are the result of increasing time and changes in the measurements that are actually dependent on ϕ_b. However, the nature of the experiments makes it difficult to change ϕ_b randomly as removing particles is quite labour intensive and it inevitably causes some of the liquid to leave the system as well, as it sticks to the particles. It was therefore decided that increasing ϕ_b consistently was the more sensible option. The values of ϕ_b that were investigated are given in table 1, together with the achieved suspension Reynolds numbers. The step size varies to investigate the change in attenuation and particle migration more closely around certain ϕ_b. This is done mostly around $\phi_b = 0.10$ as previous results suggested that the attenuation behaviour at the midline of the pipe started to deviate from linearity around this value. Moreover, the change from homogeneous particle distributions to core peaking behaviour was found by Hogendoorn, Breugem, et al., 2023 to happen around this value, as shown in Fig. 7. For each ϕ_b, measurements were done at three Re_s. The initial aim was to measure at $Re_s = 1000, 2500, 5500$ as these values make some of the cases line up with cases from Hogendoorn, Breugem, et al., 2023, allowing for direct comparison later on. Not all cases that were measured will be included in the post processing. This is because some mistake during the experimental preparation caused the flow to not be neutrally buoyant. This means that a detailed discussion of the particle migration is not possible with the data that was gathered. This will be explained further in section 5. The cases that are not processed are printed in gray in table 1.

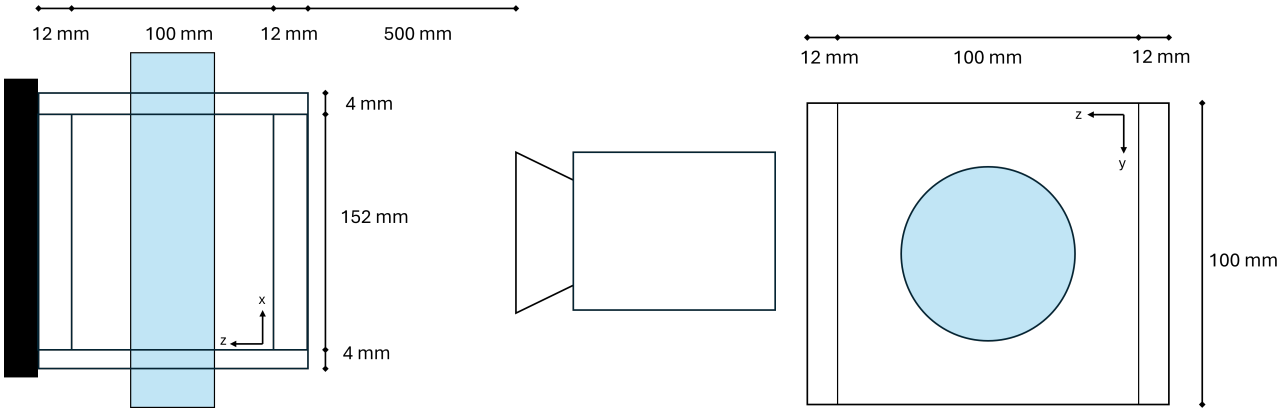

Figure 12: Schematic representation of the measurement section of the pipe flow experiments. Top view with the LED panel on the left and the camera on the right (a) and a side view of only the refraction box and pipe (b), both with coordinate systems and dimensions included.

The measurement section in Fig. 11 consists of the camera setup shown in Fig. 12. Here, the pipe goes through a transparent acrylic box filled with the same ratio of water and glycerol as the suspending liquid. This ensures that the light is not refracted by the circular shape of the pipe. On the backside of this box an unbranded LED panel is set flush to the box. Although the full specifications of the LED panel are unknown,

Table 1: Bulk volume fraction and suspension Reynolds number for all experimental cases. The cases printed in gray will not be included in the post-processing in chapter 5 because the lack of neutral buoyancy in the flows makes a detailed discussion of particle migration impossible with the methods that were used.

ϕ_b	Low Re_s	Mid Re_s	High Re_s
0.01	1190	1692	6003
0.02	1222	2627	5612
0.04	877	2387	5843
0.06	960	2812	5949
0.08	1031	2744	5786
0.09	1022	2604	5803
0.10	1094	2625	5942
0.11	1186	2644	6081
0.12	1046	2548	5871
0.13	1000	2717	5993
0.15	956	2543	5658
0.17	1029	2615	5813
0.19	956	2595	5771
0.21	1057	2656	5671
0.25	1051	2595	5765

Table 2: Camera specifications and settings that were used during pipe flow experiments

Camera specifications	
f	50 mm
Digital output	16 bit
Number of pixels	2560 x 2160
Pixel size	6.5 μm x 6.5 μm
Camera settings	
$f_{\#}$	5.6
Focus distance	$\sim$ 0.45 m
Exposure time	1650 μs
Imaging frequency	5 Hz
N_{tot}	2000

we know that the light that the LEDs emit is white. Since the particles are white too, we know that their attenuation coefficient is not a function of the lights wavelength. This means that the actual intensity and wavelength of the light from the panel will not impact the measured attenuation. The LaVision Imager sCMOS CLHS camera is stood in front of the refraction box, opposite the LED panel. It is equipped with a NIKON AF NIKKOR 50 mm lens. The data is gathered using DaVis 10.2 software. The entire measurement section was shielded from the top and on both sides. This means that the only extraneous light entering the section came from the bottom or from behind the camera. The camera's specifications and settings are shown in table 2. These settings were chosen to attain a maximum amount of light captured, i.e. minimizing the $f_{\#}$, with a depth of field just wide enough to have the entire inside of the pipe in focus. The exposure time was then adjusted to achieve the highest possible exposure without overexposure. The resulting images showed a small amount of motion blur at high flow rates, as is shown in Fig. 13. The impact this has on the results will be discussed in section 3.3. The imaging frequency and total number of samples per measurement N_{tot} were chosen based on some preliminary measurements. These measurements showed that the measurements were adequately converged for $N_{tot} = 2000$. For more details see appendix A.

The imaging frequency of 5 Hz was estimated before any measurements were taken as an appropriate value. It should be low enough to prevent significant oversampling but high enough that reaching a converged mean value can be done in a timely fashion. The current settings mean that a single measurement takes 400 s or just shy of seven minutes. To approximate if the sampling rate isn't too high, we can look at the residence time t_s of a particle in the measurement section. The length of this section is just shy of 15 cm. This is less than the total length of pipe inside the refraction box because the edges of the images also include parts of the sides of the box and therefore cannot be used for the measurements. For this approximation we assume that the average flow velocity of the particles u_p is the same as the measured volumetric flow rate divided by the cross-sectional area of the pipe. The highest u_p is for the case where $\phi_b = 0.25$ and $Re_s = 5765$ where $u_p = 0.92$ m/s. This corresponds to a residence time in the 15 cm pipe section of $t_s = 0.16$ s. This means that for an imaging rate of 5 Hz, on average all the particles present in the pipe section when one image is taken will have left the measurement section before the next image is taken. The lowest $u_p = 0.09$ m/s for the case where $\phi_b = 0.01$ and $Re_s = 1190$. In this case the residence time is thus $t_s = 1.67$ s. This means that on average only every ninth sample consists of entirely new particles. This suggests that for low flow velocities, the current imaging rate is oversampling the behaviour, since subsequent samples contain many of the same particles. Since we know that the average velocity of the particles perpendicular to the main flow velocity is significantly smaller than the streamwise velocity, we can assume that the positions of the particles with respect to each other will also not change significantly between samples. This means that, for low flow rates, subsequent

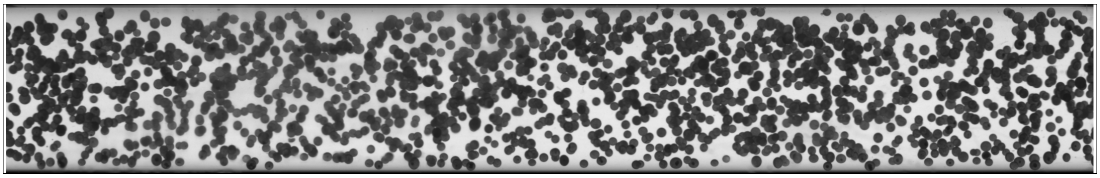

(a) $\phi_b = 0.04$,$Re_s = 877$

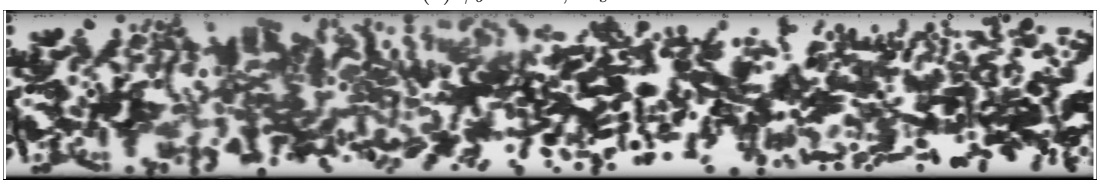

(b) $\phi_b = 0.04$,$Re_s = 5843$

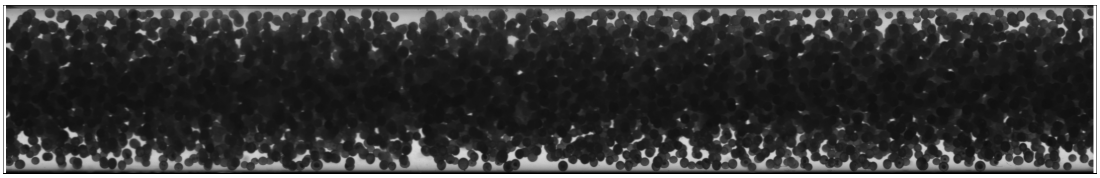

(c) $\phi_b = 0.17$,$Re_s = 1029$

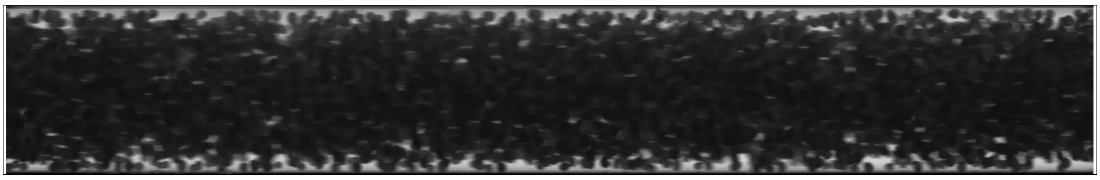

(d) $\phi_b = 0.17$,$Re_s = 5813$

Figure 13: Single measurement frames for varying ϕ_b and Re_s. The effect of motion blur can be seen for the higher Re_s cases (b) and (d).

samples are highly correlated. Oversampling has two main effects. Firstly it means that more data is being gathered than is strictly necessary, making the data processing more time consuming than it would otherwise need to be. Secondly, it can impact the calculation of the standard deviation of the measurement. Here it is important to use only every subsequent uncorrelated sample instead of every single sample. Neglecting to do so will underestimate the standard deviation and the standard error of the mean. This can however easily be avoided by calculating the correlation of the samples. This all means that a lower sampling frequency may have been more efficient, but the current chosen value does not impact results. In the end, the standard deviation of the pipe flow measurement data was not calculated for reasons that will be elaborated in section 3.3. This means that the correlation of the samples was also not calculated as it was not necessary.

As described in section 2.4.3, the intention was to use the pipe flow setup to generate a calibration curve by measuring the attenuation at the midline of the pipe for known volume fractions. However, this comes with a few issues. Most importantly, the potential difference between the bulk volume fraction in the entire system ϕ_b and the effective volume fraction inside the pipe flow. The difference between these values has different causes. Firstly it is possible that certain particles accumulate in parts of the flow loop, specifically the reservoir. Although the overhead stirrer should limit this accumulation in the reservoir, it cannot be ruled out entirely. Secondly the particles may have a different average velocity than the liquid. This would mainly be the case for flows experiencing core peaking, where the particles accumulate in the centre of the pipe. This causes them to have a higher average velocity than the liquid, causing the effective volume fraction to be higher than ϕ_b. This uncertainty in ϕ will translate into an uncertainty of the calibrated A_t value. A second issue is that the particles are not likely to be equally distributed within the pipe. This means that even if the local bulk volume fraction is known, the impact of ℓ cannot be measured independently as the volume fraction will also change in the y-direction. This means that calibration measurements in the pipe setup will only generate data with known ϕ at the midline of the pipe. It was therefore decided to do calibration measurements in a separate setup where the impact of ϕ and ℓ could be measured independently and more data could be gathered. This setup is described in the next section.

3.2 Experimental calibration setup

The calibration experiments were done in a separate setup which is shown in Fig. 14. It consists of a box the same size as the refraction box used for the pipe flow experiments, with a transparent acrylic divider sheet diagonally inside the box. The fit of this divider inside the box ensures that the particles stay on one side while the liquid can pass to the other side freely. The diagonal divider causes the path length through the suspension to vary consistently in the horizontal direction. Even though the distance in the z direction between the front of the box and the diagonal plate varies linearly, this is not quite true for the path length. This is due to the angle of view of the camera. This has been accounted for in the processing of the results as will be described in section 3.3. To prepare for the experiments, the box is filled with the suspending liquid. The proportions of water and glycerol are found in the same way as described in section 3.1. Polysorbate 20 is again used as a surfactant. Because the particles are only present on one side of the divider, calculating the amount of particles needed is slightly different than for the pipe flow experiments. The particle volume V_p can be found by solving the following equation

$$V_p = \phi_b V_{used} = \phi_b \frac{1}{2} L_1 L_2 \frac{V_l + V_p}{L_1 L_2 + L_3 L_4} \tag{22}$$

where V_{used} is the total volume of suspension in front of the divider, V_l is the total liquid volume and L_1, L_2, L_3, L_4 are the lengths given in Fig. 14b. The necessary mass of particles is then $M_p = \rho V_p$. For each subsequent measurement the amount of particles added was M_p for the next value of ϕ_b minus the already present particle mass. For high amounts of particles some of the liquid was removed to prevent overflowing of the setup. The removed liquid was weighed and this was accounted for when calculating the subsequent volume fractions. Measurements were done for $\phi_b = 0.025 \rightarrow 0.60$. The exact values are given in table 3.

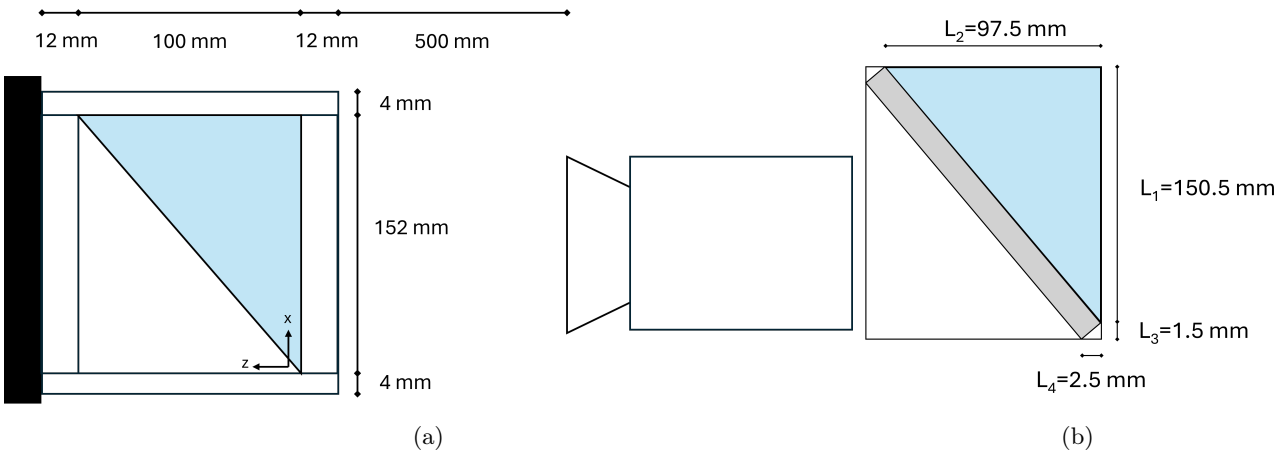

(a) (b)

Figure 14: Schematic representation of the calibration setup. Top view with the LED panel on the left and the camera on the right with dimensions and coordinate system included (a) and a detailed top view showing the inside of the box with the diagonal divider in grey with dimensions included (b). The blue area of the box contains the suspension while the white area only contains the suspending liquid.

Table 3: Bulk volume fraction and total number of samples taken per measurement for all calibration experiment cases.

ϕ_b	N_{tot}
0.025	75
0.050	75
0.075	75
0.100	75
0.125	75
0.150	75
0.175	75
0.200	75
0.250	75
0.300	75
0.350	75
0.400	50
0.450	50
0.500	50
0.550	50
0.600	50

Table 4: Camera settings that were used during calibration experiments

Camera settings	
$f_{\#}$	5.6
Focus distance	$\sim$ 0.45 m
Exposure time	1625 μs
Imaging frequency	5 Hz
N_{tot}	50 or 75
Measurements per case M	7

The box for the calibration experiments was placed on top of the refraction box of the pipe flow experiments so that the measurements could be done with the same camera and LED panel combination. The camera settings used during these experiments are shown in table 4. They are intentionally almost the same as the values in table 2. The small difference in exposure time was necessary to prevent overexposure. This change does not impact the measured attenuation. The main difference is the smaller number of samples taken. This was necessary to accommodate the different flow in the calibration experiments. Since the pipe flow measurements have a continuous flow, it is possible to do one long measurement per case. For these calibration experiments, the flow was created by manually stirring the suspension with a stirring stick. The camera recording would be started after removing the stirring stick. This only allows a short window of time where the measurements can be done before the particles slow down significantly. This was accounted for by doing seven repeat measurements for every case. The amount of samples taken per measurement was 75 for most measurements. At high volume fractions it was decided to take 50 samples instead, as the movement of the particles stopped sooner than for lower ϕ_b. A lower amount of samples ensures that there is some amount of movement happening during the entire measurement. Additionally the high amount of particles ensure that the measurements will converge faster.

3.3 Results processing

For both types of experiments, the direct output of a measurement is a set of gray-scale images captured by the camera. These images are exported from DaVis 10.2 as TIF files which are then imported into MATLAB R2020b. Here, the images are simply matrices with an intensity value for every pixel. Because the camera is 16 bit, the matrix data type is "16 bit unsigned integers". This means the intensity range is 0-65 535. For calculations the data type is changed to "double" to allow for the use of decimals. The first step is to calculate the attenuation for every image separately using the left hand side equivalence in Eq. 17. Technically the values for I_0 and I should be the light intensity before light passes through the suspension and right after it passes through, respectively. However, this is the same as using the measured I of the camera and comparing it to a measurement I_0 taken by the camera of the same setup but without any particles in it. This comparison to the background intensity is also the general practice in spectrophotometry experiments (e.g. Bachmann and Miller, 2020). The mathematical justification of this method is given in appendix B. In the case of the calibration measurements the background image of the setup was simply taken before any particles were added, it is shown in Fig. 15. The red box shows the area of the images that was actually used to generate attenuation data. In the pipe flow case this was not possible because the refraction box needs to be filled with the same proportions of water and glycerol as the pipe. These proportions are only known after correctly density matching the suspension. This means that particles are present in the pipe flow before the refraction box is filled. It was attempted to get a particle free image of the pipe by blocking the reservoir outlet with a sieve. Although this greatly reduced the amount of particles inside the pipe, it was never fully free of particles. Instead, a set

of one hundred images was taken with very few particles. The median of these images was then used as the background image. Both the background image and an example of an images with very few particles are shown in Fig. 16.

Figure 15: Background image taken for calibration experiments. This image is used as I_0 to find the attenuation in the calibration measurements. Only the area inside the red box was used to generate results.

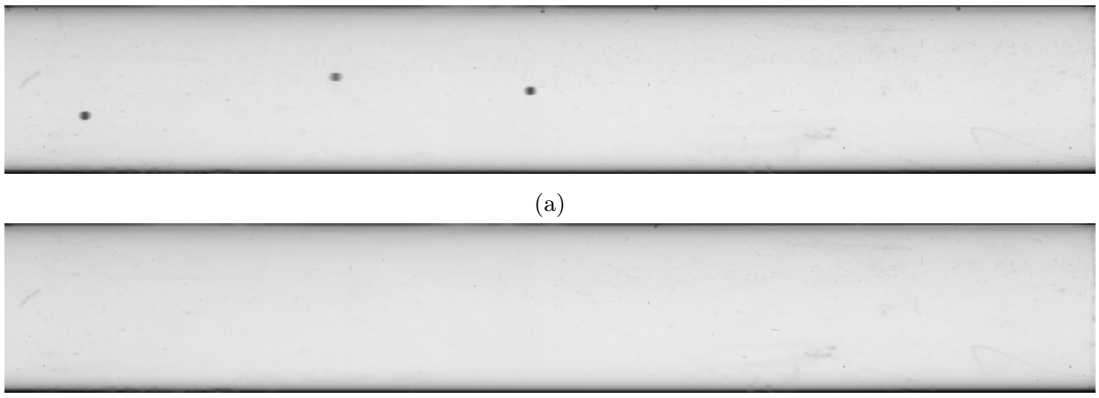

(a)

(b)

Figure 16: One of the hundred images taken with very few particles to generate a background image (a) and the final background image created by taking the median of theses images (b). This image is used as I_0 to find the attenuation in the pipe flow measurements.

The calculated attenuation matrices are then averaged to obtain a 2 dimensional matrix of time average attenuation at every pixel. It is important to do this averaging after calculating the attenuation instead of calculating the attenuation of the average intensity, as they will not result in the same value. As the attenuation is a convex function of the measured intensity, Jensen's inequality (e.g. Dekking et al., 2005) tells us that the average attenuation is greater than or equal to the attenuation of the average intensity. Since the variable of interest is the attenuation, we should calculate the attenuation for every sample first before doing any averaging. This is of particular importance for measurements at low ϕ_b where the measured intensity fluctuates more. This is also the reason that any motion blur will cause issues. Before the pipe flow experiments were conducted, the proposed method for processing the results was to first find the average intensity and then find the attenuation of this average. With this method in mind, motion blur was deemed to not be an issue as the resulting images are essentially a time average of the intensity taken over a very short period of time. However, since the correct

order of operations is to do the averaging after calculating the attenuation, any motion blur is undesirable. However, eliminating motion blur requires a lower exposure time, which lowers the exposure of the images, which is undesirable. Even though motion blur was indeed present in the high Re_s cases, as is shown in Fig. 13, the effect is relatively minor. It is expected to have only minimal impact on the end results.
After obtaining the time averaged attenuation projections, the next step is to average all the found attenuation values for the same path length so that we get a one dimensional result in the form of $A_t = f(\ell)$ for each ϕ_b. We will first discuss the path length related to the calibration measurements. As mentioned earlier, the angle of view of the camera means that the measured path length is slightly different from the distance between the plates in the z-direction. This is exhibited by the fact that the sides of the box are visible in Fig. 15. The horizontal distance between the beginning and end of these sides can be used to find the angle at which they were captured by the camera. Combined with the known width of the box we can then find the distance between the camera and the box as well as the slanted plate in the setup. This allows us to define the path length for every pixel as the distance between the front plate of the box and the diagonal divider along the line of sight for that pixel. This was done for the calibration experiments and it was found that the difference between the path length and the distance between the plates in the z-direction was $< 7\%$. For a large portion of the image the difference is even smaller. Because the pipe flow experiments used a significantly smaller portion of the field of view, the difference between the real path length ℓ and the horizontal distance in z-direction between the front and back of the pipe is very small. This means that ℓ approximately only varies with y. This is also a requirement to be able to apply the inverse Abel transform later on. We thus simply average the attenuation profiles for the pipe flow experiments in the x-direction to get a 1 dimensional average attenuation profile as a function of y. In the case of the calibration experiments, the attenuation at all pixels with the same path length are averaged to find 1 dimensional attenuation profiles as a function of ℓ for each measurement. As mentioned in table 4, seven measurements were done for each ϕ_b. The resulting attenuation profiles are then averaged to find a single profile for each ϕ_b. To get an idea of the precision of this mean profile we look at the pooled standard deviation of the means which is defined as (e.g. Figliola and Beasley, 2015)

$$\langle s_{\bar{A}_t} \rangle = \frac{\langle s_{A_t} \rangle}{\sqrt{M}} \tag{23}$$

where $\langle s_{A_t} \rangle$ is the pooled standard deviation which is defined as

$$\langle s_{A_t} \rangle = \sqrt{\frac{1}{M-1} \sum_{j=1}^{M} (\bar{A}_{t,j} - \langle \bar{A}_t \rangle)^2} \tag{24}$$

where $\bar{A}_{t,j}$ is the mean attenuation for one measurement and $\langle \bar{A}_t \rangle$ is the pooled mean attenuation of all measurements for the same ϕ_b. From this we can find the confidence interval of the pooled means using the Student's t variable. If we assume a normal distribution of the means around the pooled mean, we can state that

$$\bar{A}_{t,i} = \langle \bar{A}_t \rangle \pm t_{\nu,P} \langle s_{\bar{A}_t} \rangle. \tag{25}$$

$\pm t_{\nu,P} \langle s_{\bar{A}_t} \rangle$ is the confidence interval given at the percentage probability P where $\nu = M - 1$ is the degrees of freedom. The value for this Student's t is tabulated for given values of P and ν (e.g. Figliola and Beasley, 2015). For a 95% confidence interval with the current $\nu = M - 1 = 6$ the Student's $t_{6,95} = 2.447$. Since the attenuation curves are constructed from seven measured curves, every point on the mean attenuation curves will have its own pooled standard deviation of the means.

The resulting A_t curves from the calibration measurements can be combined to form one curve that shows $A_t = f(\phi\ell)$, as it is clear from theory that A_t should increase monotonically with both increasing ϕ and ℓ. This is because both of these result in an increase of particles in between the light source and the camera. In fact a doubling of ℓ at constant ϕ increases the average amount of particles by the same amount as doubling ϕ at constant ℓ. This means that A_t should be a function of the product $\phi\ell$. The calibration experiments should thus result in a calibration curve that connects the measured A_t to the product $\phi\ell$. We can use this calibration curve to transform the measured $A_t = f(y)$ profiles for the pipe flow experiments into $\phi\ell = f(y)$. Since the suspension is neutrally buoyant, the particle migration behaviour should be axisymmetric. This means that the $\phi\ell$ profiles should be symmetric in the midline. This allows us to reproduce the 3 dimensional volume fraction distribution using the inverse Abel transform.
The Abel transform is an integral transform that mathematically describes the projection of an axisymmetric function onto a plane. The measurements taken in the pipe flow experiments are projections of the axisymmetric flow and are thus the Abel transform of the axisymmetric volume fraction distribution in the flow. We can

reconstruct the radial volume fraction distribution with the inverse Abel transform. The analytical definition of the inverse Abel transform is

$$f(r) = -\frac{1}{\pi}\int_{r}^{D/2}\frac{dF}{dy}\frac{dy}{\sqrt{y^2-r^2}} \tag{26}$$

where $f(r)$ is the radial volume fraction distribution and $F(y)$ is the $\phi\ell = f(y)$ projection from the experiments. Implementing this numerically to discrete data can be done in different ways. The method chosen here is described by Pretzler (1991). This method was implemented into a Matlab function by Carsten Killer (2025). The core of the method is that the radial distribution is approximated with a cosine expansion. The Matlab function only requires one half of the $\phi\ell$ profile as input. If the flow is indeed fully axisymmetric, both sides of the profile should be identical. This half profile, the radius of the system $D/2$ and the number of cosine terms to use should be given as input to the function. The Abel transform of the cosine expansion is then least squares fitted to the real data, from which the amplitudes of the cosine terms are gathered. The result is a radial volume fraction distribution of the form

$$\phi(r) = \sum_{n=0}^{N_u} A_n f_n(r),\ f_0(r) = 1,\ f_n(r) = 1-(-1)^n cos\left(n\pi\frac{r}{D/2}\right) \tag{27}$$

where N_u is the upper frequency limit or the amount of cosine terms that will be used for the expansion, A_n are the amplitudes and $f_n(r)$ is the set of cosine functions. It should be noted that this method is only accurate for axisymmetric systems. If the flow is not neutrally buoyant, the ϕ distribution won't be axisymmetric and therefore the proposed method will not be able to generate radial ϕ distributions. If this is the case, the gathered data is in general not enough to reconstruct the three dimensional volume fraction distribution. Instead, projections from different angles would be needed and an inverse Radon transform would be necessary instead of the inverse Abel transform.

The result from the inverse Abel transform will be radial volume fraction distributions for every measured ϕ_b and Re_s. These profiles can then be compared amongst each other and to results from other sources to verify the accuracy and applicability of the method. Comparison to other sources will verify the quantitative accuracy of the proposed method. It will also help to verify if the method is qualitatively able to capture certain phenomena. Comparing the profiles among themselves is also used to verify the qualitative accuracy of the method. Most importantly, the radial profiles should reach higher values at the centreline for increasing ϕ_b at constant Re_s and the profiles should show more core peaking for lower Re_s at constant ϕ_b. The degree to which the radial profiles can be distinguished will determine the accuracy of the proposed experimental method.

Lastly it should be mentioned that, in the case of the pipe flow measurements, only one long measurement was done. This means that there is no pooled mean and thus no pooled standard deviation of the means. Instead the precision of the measured value is argued with the convergence of the mean, as was mentioned in section 3.1 and appendix A. It is possible to define a standard error of the mean based on the standard deviation of the measurement and the number of uncorrelated samples. However, this was not done for the pipe flow results, in the first place because it was already proven that the mean values were properly converged. Secondly, because the pipe flow measurements were not symmetric due to a lack of neutral buoyancy. This will be discussed in later sections. Since the experimental method is designed specifically for neutrally buoyant suspensions, the resulting radial volume fraction distributions will not be quantitatively correct. This means that only a qualitative discussion of the results is in order, for which the exact standard error of the mean is not of much importance. Because of this, the correlation of the samples in the pipe flow experiments was not calculated either.

4 Calibration

The calibration measurements, as described in the previous section, resulted in sixteen datasets of attenuation dependent on path length for different volume fractions. This data is visualized in Fig. 17a. A single error bar is shown on the lowest curve for $\phi_b = 0.025$. As mentioned in the previous section, every point of every curve has its own pooled standard deviation of the means and thus its own confidence bounds. The error bar shows the absolute largest confidence bound of all the points. This is $\pm t_{6,95}\langle s_{\bar{A}_t}\rangle = 2.447 \cdot 0.0138 = 0.0338$. It should be noted that the average confidence bound for all points is more than five times smaller than this, as most points have a lower pooled standard deviation of the means. Fig. 17b shows the calibrated A_t data plotted against $\phi\ell$. It can be seen that part of the data indeed collapses onto a single curve. However, for all datasets, the data measured at higher ℓ starts to deviate from this common curve. The attenuation starts to decrease with increasing ℓ. This phenomenon is thought to be due to an issue with the experimental setup. The higher path lengths are measured towards the right side of the box. During the experiments it could be

seen that the particles near the right wall looked brighter than those in the middle. This is shown in Fig. 18. This is likely caused by extraneous light coming from parts of the LED panel besides the experimental area entering through the transparent side of the box. This light is then scattered by the particles, making them brighter than they would have been if only light from behind the box had been measured. This artifact is more prominent for higher ϕ. To account for this artifact, only the data gathered for $\ell < 45$ mm is considered reliable.

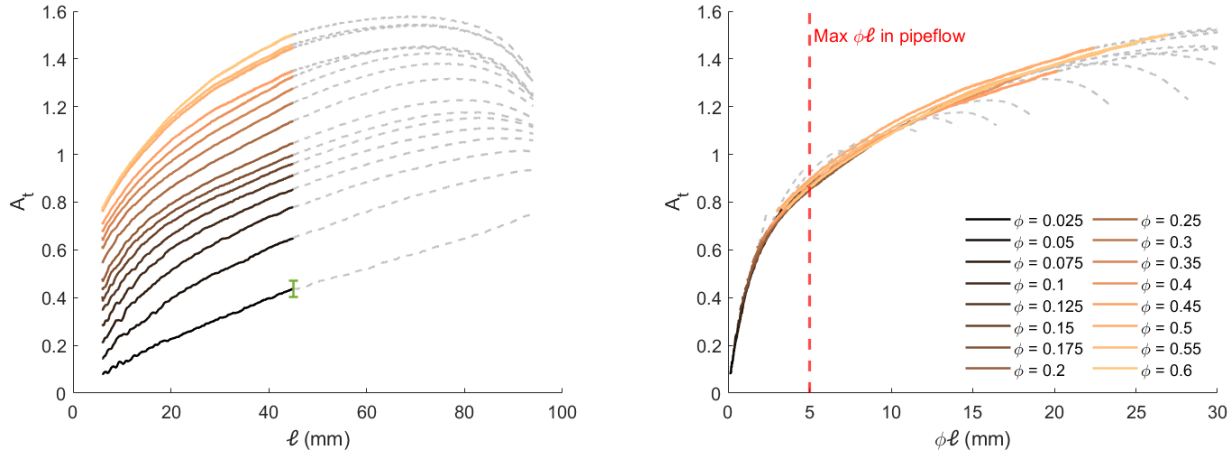

(a) (b)

Figure 17: Measured attenuation as function of path length for varying solid volume fractions with error bar showing the maximum 95% confidence interval of $\pm t_{6,95}\langle s_{\bar{A}_t}\rangle = 0.0338$ (a). This data collapses into one curve when plotting the attenuation as a function of $\phi\ell$ (b). The maximum value for $\phi\ell$ expected in the pipe flow setup is indicated with a red dashed line. The unreliable part of the data where $\ell > 45$ mm is shown in gray.

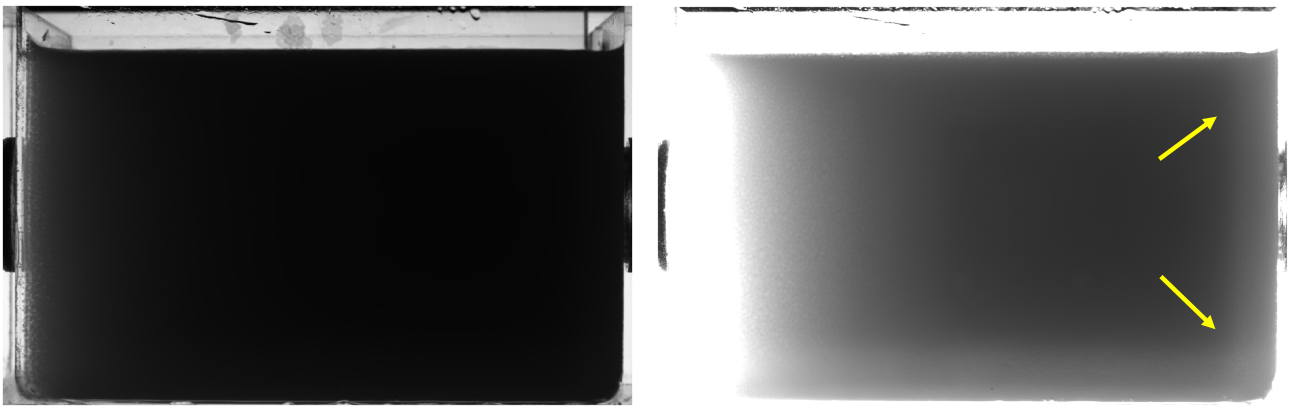

(a) (b)

Figure 18: Time averaged image for $\phi = 0.60$ (a) and the same image rescaled to an intensity range of zero to eight thousand to emphasise the brightening effect on the right side of the image (b).

This part of the data can then be used to generate a calibration curve and to further investigate the light attenuation behaviour in this system. While the calibration experiments produced reliable results up to $\phi\ell = 27$ mm, the highest value that is expected to be relevant to the pipe flow experiments is $\phi\ell = 5$ mm since the pipe diameter, and thus the maximum path length, is 20 mm and the highest measured bulk volume fraction is $\phi_b = 0.25$. This maximum is also indicated in Fig. 17b. An eighth order polynomial fit of the form $\phi\ell = f(A_t)$ will be used as calibration curve to find the $\phi\ell$ value from the measured average A_t. This polynomial fit was found using the Curve Fitting Toolbox in Matlab which applies a least-squares method. The zero-order term of the polynomial was bound to zero to ensure that applying the calibration to a measurement of $A_t = 0$ results in $\phi\ell = 0$. This also necessary because the current measurement data has a minimum of $\phi\ell = 0.15$, therefore there is no knowledge of how the system actually behaves below this value. While the Beer-Lambert law and similar models are of the form $A_t = f(\phi\ell)$, the eighth order polynomial fit instead uses A_t as the independent

variable as this is the variable that is being measured. Delgado (2022) explains that fitting a function of the form $A_t = f(\phi\ell)$ will introduce an error into the results if the calibration curve is then used to find $\phi\ell$ from the measured A_t. Since the fit was created by finding the least square error between the measured and fitted values for A_t for given $\phi\ell$, it is not ensured that the error between measured and fitted $\phi\ell$ is minimized for given A_t. Although Delgado (2022) specifically discusses linear regression models, this problem persists for different types of fits. Even though the high amount of measurement points from the calibration experiments means that the difference between both fits is minimal, for consistency, the correct fit of the form $\phi\ell = f(A_t)$ will be used. Using this calibration curve, the attenuation corresponding with the maximum $\phi\ell = 5$ mm is $A_t = 0.86$.
The data from Fig. 17b has been replotted on a log-log scale in Fig. 19 to investigate possible power law fits for the data. The data for lower $\phi\ell$ has a slope close to one which suggests a linear relationship between A_t and $\phi\ell$ and the data for higher $\phi\ell$ has a slope close to 1/3, suggesting a cube root relationship. Between these two domains, the slope transitions gradually. This shows that although the behaviour starts out linear, it eventually deviates from the Beer-Lambert law, as was expected based on prior knowledge. The Curve Fitting Toolbox was then once again used to find the appropriate fits of these types to the relevant data. The resulting fits are shown in Fig. 19, both on the log-log scale and the linear scale in the insert. They are also tabulated in table 5 which also shows the domain that was used for fitting and the resulting R^2 value on that domain.

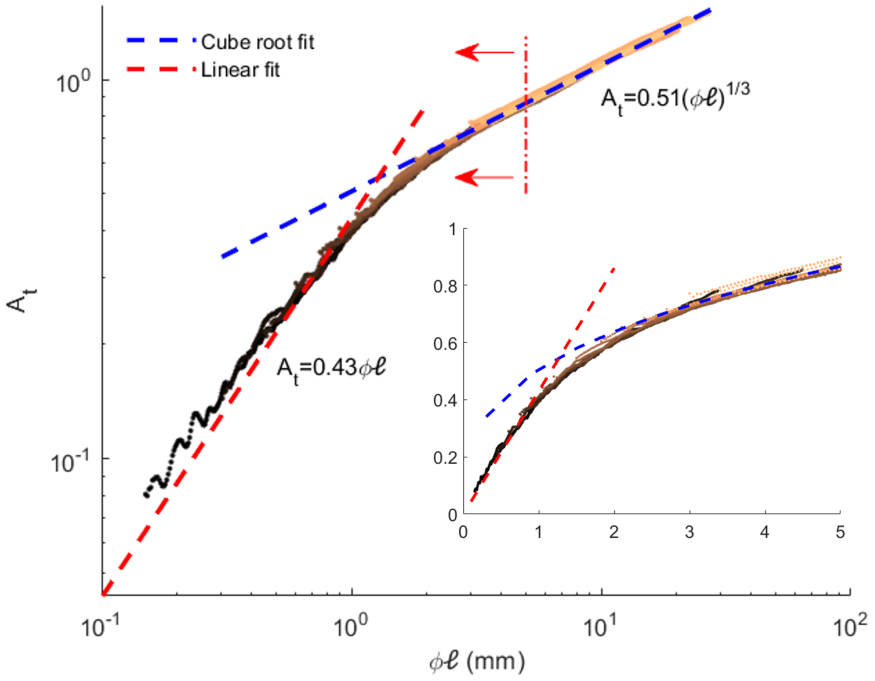

Figure 19: Measured attenuation plotted against $\phi\ell$ on a log scale with curve fits included. The maximum of $\phi\ell = 5$ mm is indicated by the vertical dashed-dotted red line. The inserted graph shows the part of the data relevant to the pipe flow measurements on a linear scale. The axes show the same variables as the log scale plot.

Table 5: Potential fits to the calibration data

Curve fit	Domain	R^2
$A_t = 0.43\phi\ell$	$0 < \phi\ell \leq 0.9$	0.955
$A_t = 0.51(\phi\ell)^{1/3}$	$2.5 \leq \phi\ell$	0.996
8^{th} order polynomial fit*	$0 < \phi\ell$	0.999

*The coefficients for the polynomial fit are given in appendix C.

5 Pipe flow results

The pipe flow experiments, described in section 3.1, result in average attenuation profiles along the y-axis. The profiles for all measured bulk volume fractions at high suspension Reynolds numbers are shown in Fig. 20. The profiles are shown in two separate plots with different ranges on the horizontal axes to more clearly show the behaviour of the low ϕ_b profiles. It is clear from the attenuation profiles that the measured attenuation indeed increases with both increasing ϕ_b and ℓ. There are, however, some issues with the profiles. Firstly they are not symmetrical, the maximum value for all profiles lies below the midline. This is likely due to a mismatch in density between the particles and the suspending liquid, causing the particles to not be perfectly neutrally buoyant. Alternatively it could be due to a similar issue with extraneous light as was present in the calibration experiments, causing the brightening effect in Fig. 18. This can be verified and accounted for in the future by doing calibration measurements in the pipe flow setup itself to capture the impact of this brightening on the measured attenuation. Regardless of the cause of this lack of axisymmetry, it means that these experimental results are not representative and thus cannot be used to study the behaviour of neutrally buoyant suspensions. They can, however, be used to verify the applicability and limitations of the proposed experimental method. One such limitation actually pertains to the lack of axisymmetry itself. Since the experimental methods were designed to be applied to neutrally buoyant, and thus axisymmetric, flows, the gathered data is not sufficient to characterize non-neutrally buoyant suspensions. Specifically the assumption that capturing a single projection of the flow is sufficient to reconstruct the three dimensional behaviour does not hold. This means that, although the inverse Abel transform can be applied, the resulting profiles will not be actual representations of the measured flows. Because of this, not all measured cases will be post-processed, as a detailed discussion of these results with regards to particle migration is not possible based on the current data. As mentioned in table 1, the cases that are considered in this chapter are the high Re_s cases for all ϕ_b, shown in Fig. 20, and all three Re_s cases for $\phi_b = 0.04, 0.08, 0.17, 0.25$, shown in Fig. 21. The results from these cases are sufficient for the discussion of the impact of Re_s and ϕ on the measured A_t. Moreover, the accuracy of the method can also be established from these cases. The cases that are not considered did not show significant deviation from the behaviour of the considered cases. They are therefore left out of this chapter because adding their results simply would not impact the conclusions. This also reduces the time necessary for the further post processing steps.

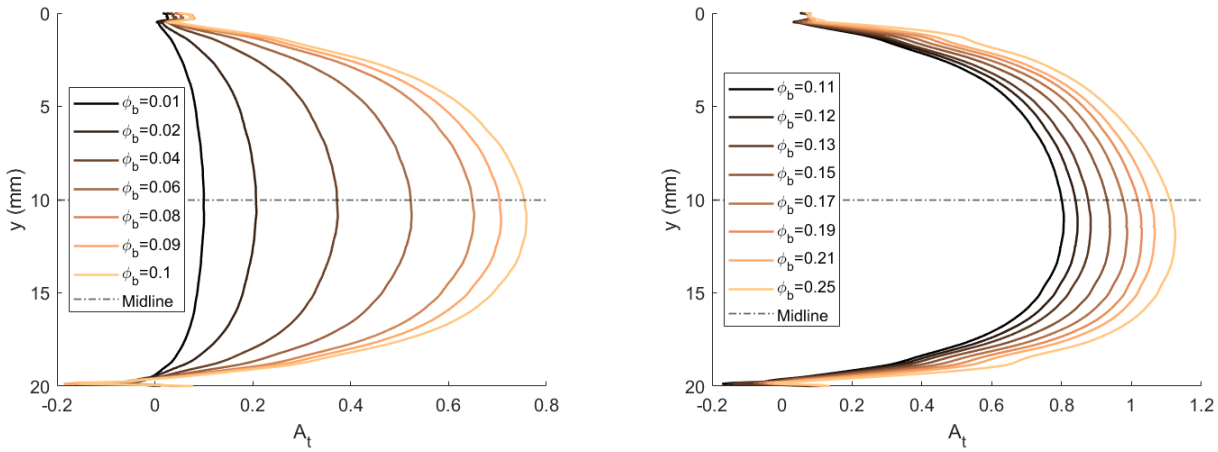

(a) (b)

Figure 20: Measured average attenuation profiles for all measured ϕ_b at $Re_s \approx 5800$. The midline of the pipe is shown with the dashed-dotted line.

The plots in Figs. 21a and 21b show a second issue with the results. The low Re_s cases plotted in yellow have a very different shape from the other profiles. They have maxima at different locations. This is thought to be because some of the particles start to float or sink. While at higher flow speeds, the particles are continuously mixed, at these lower flow speeds this happens less. This causes the particles whose density is most different from the liquid to move vertically due to buoyancy. These particles accumulate near the top and bottom of the pipe. This causes the attenuation to be higher in these areas. This effect can be seen most clearly in Fig. 21a where the curve for $Re_s = 877$ has two local maxima above and below the midline, additional to the one near the midline. It should be noted that, although this effect was indeed observed during the experiments, the gathered data is not sufficient to verify this. Since the measurements are only taken from one angle, it cannot

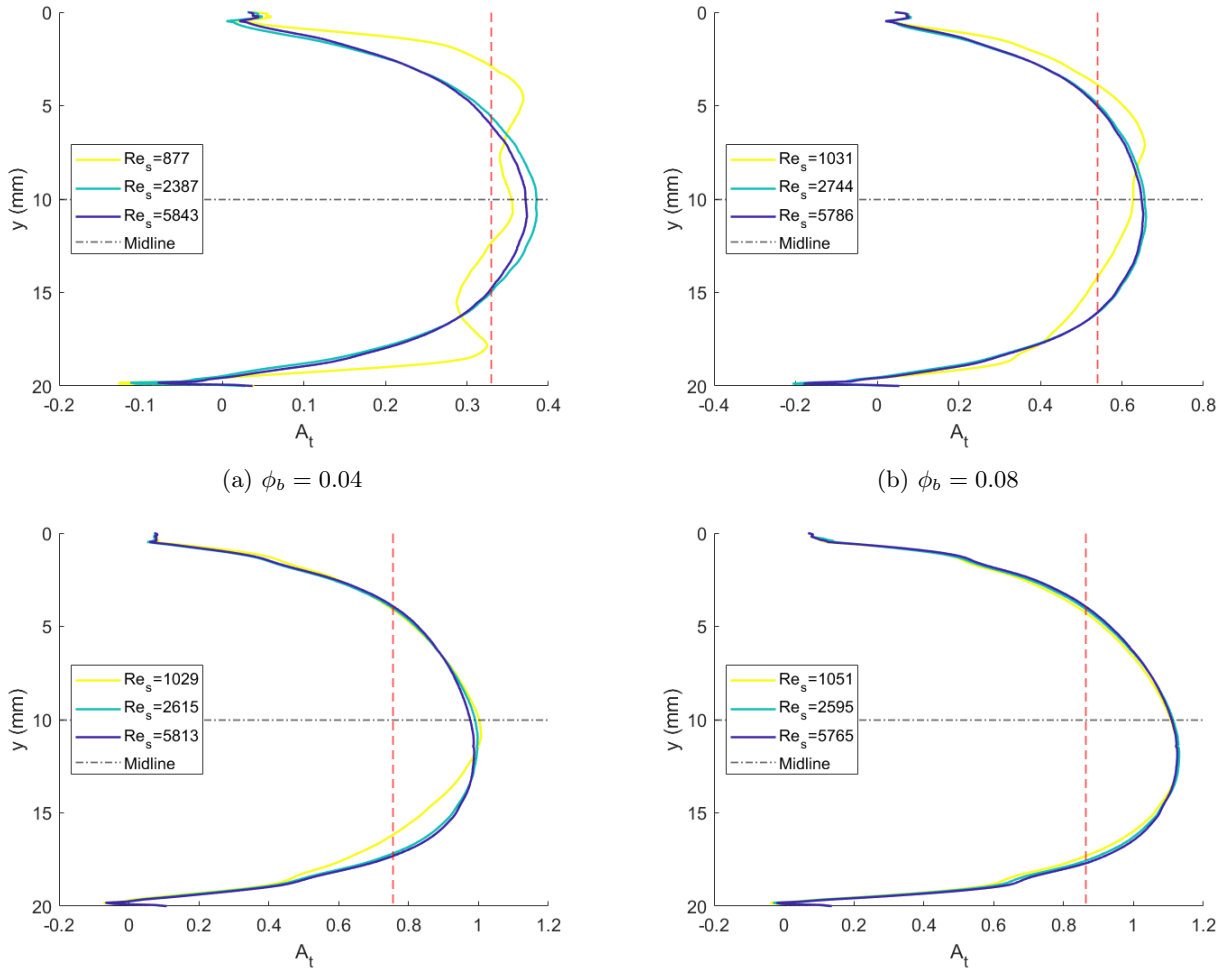

(a) $\phi_b = 0.04$ (b) $\phi_b = 0.08$

(c) $\phi_b = 0.17$ (d) $\phi_b = 0.25$

Figure 21: Measured average attenuation profiles for varying ϕ_b and Re_s. The midline of the pipe is shown with the dashed-dotted line. the vertical dashed line shows the expected attenuation value at the midline based on the calibration.

be confirmed that this behaviour is indeed the result of buoyancy. This is another reason why the gathered A_t profiles cannot be used to find the particle distributions for certain cases.

A third issue with the profiles is visible at the edges. Here the measured attenuation shows unexpected behaviour. At the top of the pipe for $y \to 0$ mm, the A_t profiles show a small bump before they start rising smoothly. At the bottom of the pipe, for $y \to 20$ mm, the A_t dips below zero. The location of these artifacts corresponds with the shadows cast by the walls of the pipe in all gathered images. Since these areas are comparatively dark in the background image already, a relatively small change in light intensity can create an attenuation artifact. It is assumed that this measured behaviour is thus not a phenomenon related to the suspension flow but a result of these shadows. To avoid these artifacts, a closer match in refractive index between the liquid and the acrylic pipe material would be necessary.

A fourth issue with the results is that the actual maximum A_t that was measured is much higher than the expected value of $A_t = 0.86$. In fact, the measured attenuation at the midline significantly deviates from the value expected from the calibration curve described in section 4. The red dashed lines in the plots of Fig. 21 show the calibrated value corresponding to the $\phi\ell$ expected at the midline of the pipe. It can be seen that these lines are below the actual measured values for these four ϕ_b. This is the case for all but one of the measured ϕ_b, as is shown in Fig. 22. This figure shows the deviation of the measured attenuation at the midline from the expected value from the calibrations, for all ϕ_b, high Re_s cases. The deviation is defined as

$$\text{Deviation} = \left(\frac{A_{t,m}}{A_{t,c}} - 1 \right) \cdot 100 \tag{28}$$

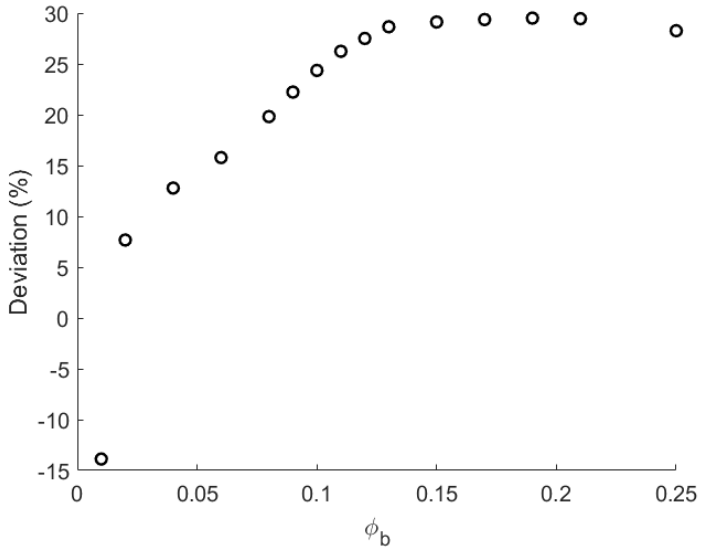

Figure 22: Deviation of the measured attenuation at the midline from the expected value from the calibration for all measured ϕ_b and $Re_s \approx 5800$.

where $A_{t,m}$ is the measured attenuation at the midline and $A_{t,c}$ is the calibration value for $\phi\ell = \phi_b \cdot 20$ mm. As the suspensions were not neutrally buoyant, the actual measured ϕ at the midline is likely lower than ϕ_b. This means that the values found in Fig. 22 cannot be used to account for the deviation by changing the calibration curve according to these values, as the measured $\phi\ell$ is unknown. The actual deviation between the calibrated and the measured A_t at the same $\phi\ell$ is probably higher than what was found from eq. 28. The main purpose of Fig. 22 is thus to show the trend of the change in the deviation. It shows that the deviation from the calibration increases with ϕ_b. As the experiments were done in the order of increasing ϕ_b, determining whether this increasing deviation is a result of increasing ϕ_b directly or a result of some other factor that changed during the experiments is not straight forward. The different possible reasons for this discrepancy will be discussed in more detail in section 6. It is difficult to account for this deviation in the further data processing steps. Instead it was decided to apply the calibration curve without accounting for the deviation. This means that the results cannot be used to make quantitive statements about the ϕ distributions in the flow. Instead the results will be compared amongst each other to examine trends and to research the potential applicability of the experimental method to more accurate data.

Using the calibration curve, the measured A_t profiles can be converted to $\phi\ell$ profiles. This process is shown in Fig. 23 for $\phi_b = 0.04, 0.08, 0.17, 0.25$ at $Re_s \approx 5800$. The resulting profiles are the projections that will be used as input for the inverse Abel transform. As the inverse Abel transform is designed for symmetric profiles, only one half of the profiles, from the midline of the projection to the edge, is needed as input. This means that the inverse Abel transform can be applied to non-symmetric profiles as well by simply using either half of the profiles as input. However, the resulting radial volume fraction profiles will not be real representations of the distribution of ϕ in the measured pipe flows. Still it is worthwhile to process the current data in this way to review the process and verify how extensively the shortcomings in the data impact the desired end result. The numerical inverse Abel transform method that will be applied was described previously in section 3. This method was applied using a Matlab function created by Carsten Killer (2025) and is based on Pretzler (1991). The top half of the $\phi\ell$ profiles will be used as input. The artifact at the edge, although much less prominent in the $\phi\ell$ profiles than in the A_t profiles as can be seen in Fig. 23, will not be taken into account. This means that the first nine data points will be removed and the tenth data point will be considered the value at the edge. This means that the effective radius used for the transform is 9.9464 mm instead of 10 mm. Replacing the missing values is also a possible strategy. The impact that this has on the final results will be discussed in section 6.3. Apart from the radius and the $\phi\ell$ profile, the numerical transform also requires an upper frequency limit N_u as input. This defines the number of cosine terms that will be used to construct the radial volume fraction distribution profile. A high N_u will result in longer computation times but it may offer smoother results. Because the gathered data is asymmetric, a detailed discussion of the proper N_u is not possible as the accuracy of the resulting radial ϕ profiles cannot be analysed. In the end a N_u of 20 was chosen as the results looked relatively smooth and the computation time was manageable.

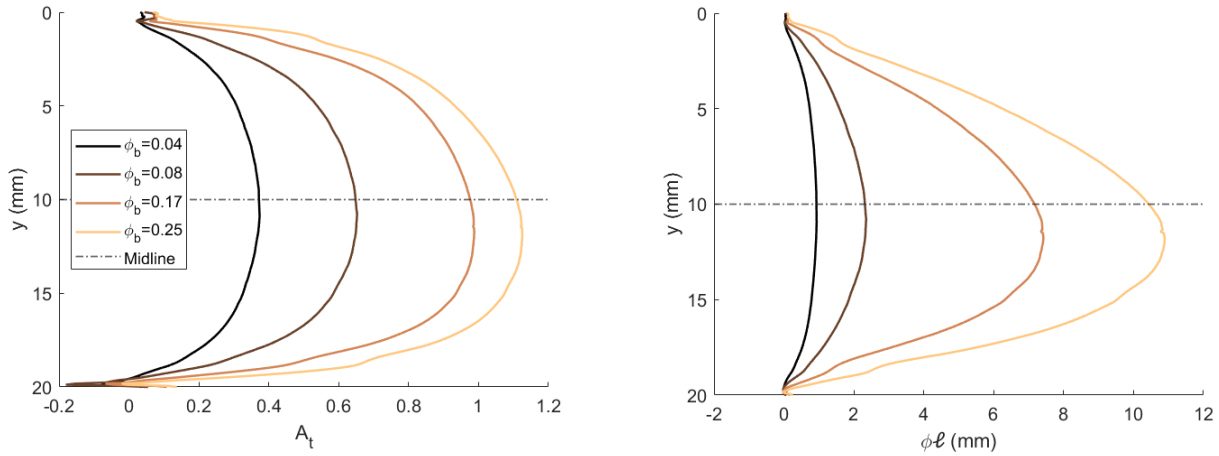

(a) (b)

Figure 23: Measured attenuation profiles for different ϕ_b at $Re_s \approx 5800$ (a) and their corresponding $\phi\ell$ profiles found using the calibration curve (b).

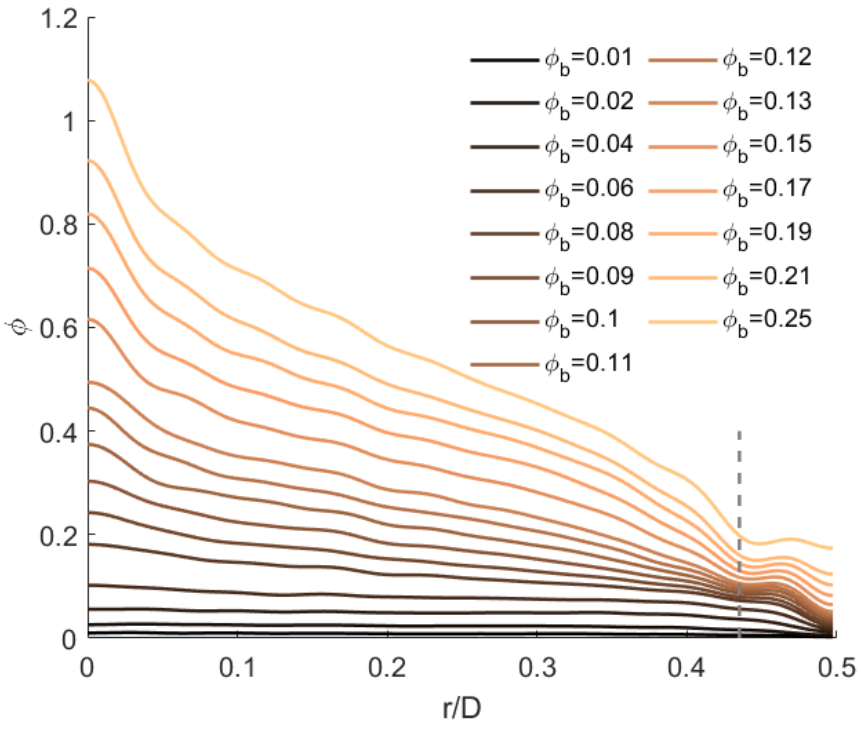

Figure 24: Radial ϕ profiles obtained from the numerical inverse Abel transform of the $\phi\ell$ projections for all ϕ_b and $Re_s \approx 5800$. The gray dashed line denotes a distance of one particle diameter from the edge of the pipe.

The radial ϕ profiles for all measured ϕ_b at high Re_s are shown in Fig. 24. Here, a few key things stand out. Firstly, that ϕ peaks at the centreline of the pipe where $r/D = 0$. This is especially true for the higher ϕ_b cases. For $\phi_b = 0.25$ this peak even reaches a maximum of $\phi > 1$ which is of course impossible. This is partly due to the deviation of the measurements from the calibration curve. As can be seen in Fig. 23 the measured A_t at the midline for $\phi_b = 0.25$ corresponds to $\phi\ell \approx 9$ which would mean that the average volume fraction along the midline of the pipe is $\phi = 0.45$. Another cause for this effect is the asymmetry of the input profiles. This causes the slope of the half profiles used as input for the inverse Abel transform to not be zero at the midline. This is not possible for a truly symmetric, continuous profile and thus the Abel transform is not equipped to deal with it properly. A second element of the profiles that is unphysical is seen near $r/D = 0.5$ where the profiles do not decrease to zero. This is a result of removing the bump from the $\phi\ell$ profile before applying the inverse

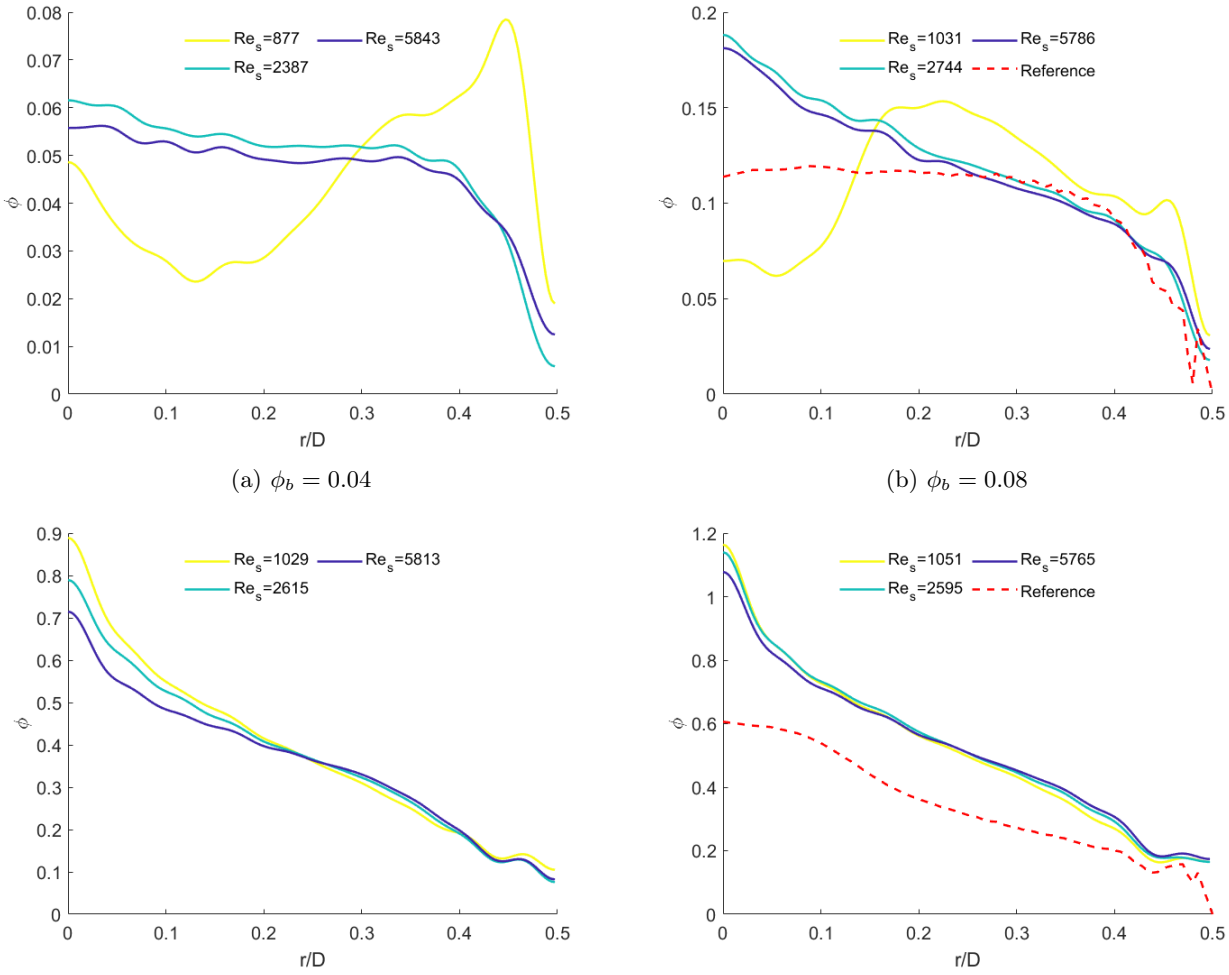

(a) $\phi_b = 0.04$

(b) $\phi_b = 0.08$

(c) $\phi_b = 0.17$

(d) $\phi_b = 0.25$

Figure 25: Radial volume fraction profiles for varying ϕ_b and Re_s. The red dashed lines show reference profiles from Hogendoorn, Breugem, et al. (2023) for $\phi_b = 0.089$ and $Re_s = 5740$ in (b) and $\phi_b = 0.252$ and $Re_s = 1083$ in (d) or case 3 and 1 in the reference respectively.

Abel transform. As the profiles now end at a non-zero A_t value, the inverse Abel transform does not reach zero either. Both of these issues are elaborated on in section 6. Another characteristic of the radial ϕ distributions is a wiggle in the profiles around $0.4 < r/D < 0.5$. This is likely due to the presence of a particle wall layer. The same behaviour was described by Hogendoorn, Breugem, et al. (2023), who explain that the particles form a ring-like structure as they are constrained by the wall. To verify that this behaviour is indeed the cause of these wiggles, we can look at the location of the local minimum. This should be at around one particle diameter from the wall which is at $r/D = 0.5 - d/D = 0.5 - 0.065 = 0.435$, this location is shown in Fig. 24 with a grey dashed line. The local minimum in the profiles occurs around $r/D = 0.447$. This does not line up exactly with the expected value, although it is close. The discrepancy may be due to the removed bump at the edge of the $\phi\ell$ profile. This will also be further investigated in section 6.

The radial ϕ profiles for $\phi_b = 0.04, 0.08, 0.17, 0.25$ at varying Re_s are shown in Fig. 25. The yellow profiles for low Re_s in Figs. 25a and 25b stand out. They both have a maximum near the wall, after which they drop down, corresponding to the maxima above the midline shown in the A_t profiles in Figs. 21a and 21b. As discussed before this is likely due to the lack of proper mixing at low flow velocities. When disregarding these two profiles, the profiles in all four plots show a common behaviour. For constant ϕ_b, the lowest Re_s cases have the highest volume fraction at the centreline and vice versa. This is especially noticeable for $\phi_b = 0.17$ and $\phi_b = 0.25$, where all three profiles have roughly the same shape. This suggests that, for lower Re_s, there are more particles near the centre of the pipe and for higher Re_s they are more evenly distributed throughout the pipe. This is consistent with the findings of Hogendoorn, Breugem, et al. (2023) for flows with ϕ_b in this range. They found that, at constant ϕ_b, a lower Re_s flow will show more core peaking than a higher Re_s flow.

This result is a strong indicator that, even though the current application of this method has its shortcomings, light attenuation measurements are sensitive enough to detect these changes in particle distributions. It also shows that, although these flows were not neutrally buoyant, shear-induced migration is still present, even if the characteristic axisymmetric core peaking behaviour was absent.
Figs. 25b and 25d both include a radial ϕ profile reproduced from Hogendoorn, Breugem, et al. (2023) as reference. These are profiles for $\phi_b = 0.089$ and $Re_s = 5740$ and for $\phi_b = 0.252$ and $Re_s = 1083$ or case 3 and 1 in the reference respectively. These profiles are the azimuthal averages of the 3D data that was gathered using MRI measurements. Comparing the current results to these profiles gives more insight into the extent of the shortcomings. Comparing the reference curve to the two blue curves in Fig. 25b, we can see that the measured values for ϕ are somewhat similar in the range of $0.25 < r/D < 0.5$. However, due to the issues with neutral buoyancy and the deviation from the calibration, this is likely a coincidence and not a true sign of corresponding results. For lower r/D the measured profiles start to deviate more strongly from the reference. Additionally, while the blue profiles rise continuously from the pipe wall inward, the reference profile shows a clear plateau. In Fig. 25d the profiles seem qualitatively similar for about $0.15 < r/D < 0.4$, where both the reference and the measured profiles rise continuously from the pipe wall inward. They do not however, rise with the same slope. This is likely due to both the deviation from the calibration and the lack of neutral buoyancy. For $0.4 < r/D < 0.5$ the profiles show a similar wiggle, characteristic of the particle wall layer behaviour described earlier. The minimum occurs around the same point, which is to be expected as the particle sizes are also similar namely $d/D = 0.065$ for the current measurements and $d/D = 0.058$ for the reference data. For $r/D < 0.15$ the behaviour is quite different. Here, the reference profile first rises more steeply before levelling out to a plateau. This is due to the core peaking behaviour this flow displays. The blue curves instead continues to rise to a peak at the centreline. The absence of a plateau is likely partly due to the lack of neutral buoyancy making it impossible for core peaking to present itself in the same way as for neutrally buoyant flows. The peak created by the non-zero slope of the $\phi\ell$ profiles at the midline adds to this effect. This will also be discussed further in section 6.

6 Discussion

Because the calibration data and the pipe flow data deviate, it is worthwhile to discuss them separately. First, this deviation itself is discussed including potential causes and solutions. Secondly the results from the calibration experiments are discussed and potential reasons for the deviation from the Beer-Lambert law are proposed. Then the pipe flow experiment results are discussed, including the impact that the assymmetry has on the inverse Abel transform.

6.1 Deviation from calibration

As mentioned before, the calibration curve from section 4 is not directly applicable to the pipe flow data and the deviation is quite significant, almost reaching thirty percent at its maximum. To investigate the potential reasons for this deviation, we look at the differences between the calibration measurements and the pipe flow measurements and possible issues with both sets of measurements. A notable difference is that the calibration experiments were not shielded. This was done because the calibration setup needed to be accessible for stirring. This meant that extraneous light from other sources than the LED panel could also enter the camera. This was largely prevented in the pipe flow measurements. During an early stage of the experiments, the background light intensity in the lab was measured by doing some short measurements with the camera while the LED panel was off and the setup was not shielded. These measurements revealed a background intensity of less than five hundred. While these measurements were not taken during the calibration experiments, they do give a general idea of the extent of this extraneous light intensity. Because the calibration experiments were done at a slightly different position, it is possible that the extraneous light intensity was higher than the five hundred measured before. We can calculate how high this extraneous light intensity I_E needs to be to fully explain the calibration deviation by looking at the difference in the calibrated attenuation $A_{t,c} = 0.86$ and the measured attenuation $A_{t,m} = 1.1$ for $\phi\ell = 5$ mm. For both measurements we assume $I_0 = 60\ 000$ and $I = I_0 10^{-A_{t,m}} = 4\ 766$.

$$A_{t,c} = log_{10} \frac{I_0 + I_E}{I + I_E} \tag{29a}$$

$$I + I_E = (I_0 + I_E) 10^{-A_{t,c}} \tag{29b}$$

$$I_E = \frac{I_0 10^{-A_{t,c}} - I}{1 - 10^{-A_{t,c}}} = 4\ 079. \tag{29c}$$

It should be noted that although the pipe flow measurements were shielded, it is unlikely that these measurements truly had zero extraneous light coming in. Combining this with the value found for I_E which is more than eight times higher than the previously measured amount, it is unlikely that the deviation from the calibration is caused entirely by the lack of shielding of the calibration measurements. If we instead assume that $I_E = 500$ and that I and I_0 are the previously mentioned values, Eqs. 29a and 28 tell us that the measured I_E only accounts for a deviation of 4%.

A different possible explanation for the deviation is that the light intensity of the LED panel may fluctuate over time. This would cause the I_0 to not be constant. This introduces an error in the results as all measurements are compared to the original background image taken at the beginning of the measurements, which would then differ from the current I_0. For the pipe flow measurements, the camera was made to use an area of interest, meaning that it only captured the inside of the pipe. This means it is not possible to measure the fluctuation of the light intensity of the LED panel during these measurements directly. The calibration measurements however, did not make use of an area of interest. We can investigate the fluctuations in the background intensity for these measurements to get an idea of their order of magnitude. A small area below the experimental setup is used for this, shown by the red box in Fig. 26a. The average light intensity in this area was plotted as a function of time for each of the calibration measurements in Fig. 26b. This shows that, although the intensity does fluctuate during the measurements of 15 and 10 s respectively, during this time frame the fluctuations are not significant. However when we look at the time averaged intensity for all measurements and compare these, a not insignificant change can be seen. This is shown in Fig. 26c. The intensity fluctuates between 61 200 and 62 300 which is a change of around 2%. It should be noted that the calibration measurements were done over the course of about 4.5 hours, starting with $\phi = 0$ and continuously adding particles until $\phi = 0.60$ was reached. The horizontal axis in Fig. 26c can thus be considered a sort of time axis. While this fluctuation is measurable, it has not significantly impacted the calibration results as they still showed a relatively clean collapse onto a single curve, as shown in Fig. 17. Nevertheless, it is possible that the change in background intensity during the pipe flow measurements were more significant, as these experiments took much longer in total. We can calculate how much the light intensity would have had to change to cause the deviation from the calibration.

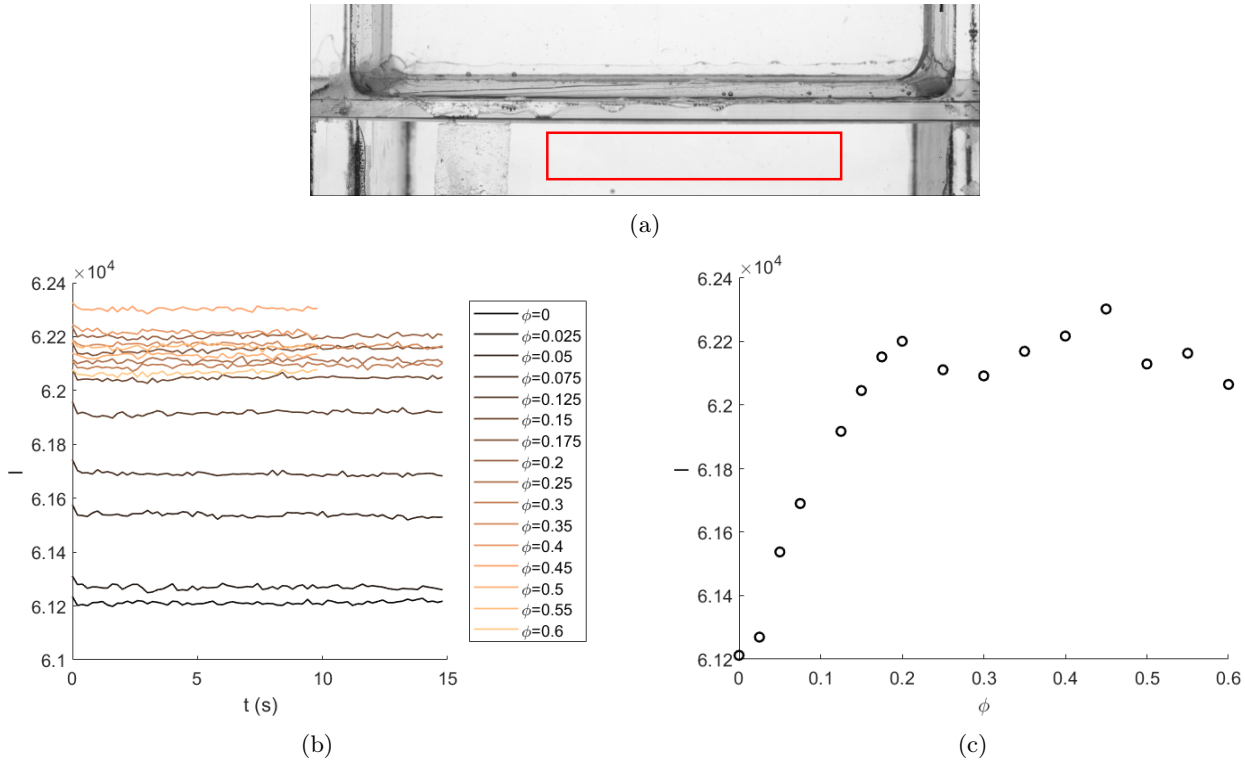

Figure 26: Area below the experimental setup in the calibration experiments used for LED panel intensity tracking (a), the spatial average of the intensity during measurements (b) and the time averaged values for different volume fraction measurements (c). The experiments were done over a period of 4.5 hours starting with $\phi = 0$ and increasing gradually to $\phi = 0.60$.

We start by defining the current background intensity $I_{0,cur} = \eta I_{0,or}$ where $I_{0,or}$ is the original intensity of the background image. We can then find the difference between the measured attenuation $A_{t,m}$ and the actual attenuation $A_{t,real}$ as such

$$A_{t,m} = log_{10}\left(\frac{I_{0,or}}{I}\right) \tag{30a}$$

$$A_{t,real} = log_{10}\left(\frac{I_{0,cur}}{I}\right) = log_{10}\left(\frac{\eta I_{0,or}}{I}\right) = A_{t,m} + log_{10}(\eta). \tag{30b}$$

The maximum difference between the measured and calibrated attenuation at the midline occurs for $\phi_b = 0.25$ where $A_{t,c} = 0.86$ and $A_{t,m} = 1.11$. If we assume that $A_{t,c} = A_{t,real}$, that means that

$$log_{10}(\eta) = -0.25 \rightarrow \eta = 0.56 \tag{31}$$

which means that the LED panel would have had to lose almost half of its light intensity to explain the deviation. This would have been clearly noticeable in the lab, and this was not encountered. If we consider the maximum change in intensity of 2% that was derived from Fig. 26c, the change in attenuation this would result from that is $log_{10}(1.02) = 0.0086$. This all tells us that the deviation from the calibration cannot be solely due to a change in light intensity from the LED panel.

There are several other factors that may be of influence as well. Firstly the fact that the pipe flow measurements were done over the course of two days while a background image was only taken on the first. Any changes in the setup on the second day would not be taken into account since no background image was taken. However, if this was indeed the case we would expect to see a distinctive difference in Fig. 22 between the cases measured on the first and second day. This would have to occur between $\phi_b = 0.13$ and $\phi_b = 0.15$ and this does not present itself. This is therefore not likely to be of major importance to the deviation. Secondly the volume fraction calculations may have been wrong in either set of experiments. This would cause the measured ϕ to be different from the assumed value. In the calibration experiments this can be ruled out. If the volume fractions were off the results would not collapse upon rescaling the horizontal axis in Fig. 17. In the pipe flow measurements this cannot be ruled out entirely. Eq. 21 was used to figure out how many particles to add for each volume fraction. This calculation assumes that the liquid and the particles have the same density, making the solid volume fraction

and the solid mass fraction the same. While the lack of neutral buoyancy proves that this assumption is not true for the pipe flow measurements, the fact that when the system was at rest, over time some of the particles still floated, shows that the difference in density cannot have been too large. It may also have been possible that the setup was not emptied of liquid entirely before refilling. However since this exact issue showed up during some preliminary tests, extra attention was given to the proper emptying before the pipe flow experiments. It is unlikely that more than a few hundred grams of liquid would have stayed behind in the system, if any at all. Especially at higher ϕ_b this would have had a marginal impact. It is however likely that the actual bulk volume fraction flowing through the pipe is different from the amount in the entire setup as the particles could potentially accumulate somewhere. Additionally the migration of the particles away from the pipe walls causes a difference in the effective volume fraction in the pipe from the ϕ_b in the reservoir. As Hogendoorn, Breugem, et al. (2023) explain, the higher velocity in the centre causes the particles to have a higher average velocity than the bulk flow. In any case, if the calibration curve is indeed correct and the deviation is only due to a wrong ϕ_b in the pipe flow measurements, the volume fraction in the pipe flow would at its highest have been $\phi_b = 0.45$, as this is the calibrated value of ϕ corresponding to maximum measured $A_t = 1.1$ at the midline. While it is definitely possible that the actual volume fractions during the pipe flow measurements deviate from the ones reported here, it is unlikely that they deviate enough to explain the deviation of the measured attenuation from the calibrated values.

Another possible explanation could be that the liquid became less clear as the experiments went on. This could have been caused by dirty particles slowly releasing dust into the system as they get agitated in the flow over time. A similar issue happened during preliminary calibration measurements, shown in Fig. 27. Here, the particles that were used hadn't been used before and had not been cleaned before use either. This meant that they were covered in polystyrene dust, which came of in the liquid. These dust particles significantly impacted the attenuation measurements, as the dust particles also attenuate light. While such a drastic change in the liquids clarity was not observed during the pipe flow measurements, it is possible that a smaller amount of dust did accumulate in the setup. This could partially explain the deviation from the calibration. However, since no visible difference in turbidity was noted during the experiments, it is unlikely that this could explain it entirely. None of the mentioned possible causes can fully explain the deviation on their own. It is likely that it was caused by a combination of different factors. While the above discussion of potential causes is the result of careful considerations of potential issues and inconsistencies, it is likely that there are other potential causes that have been overlooked here. New experiments would be needed to fully define the correct causes. Recommendations for these experiments will follow in section 7.

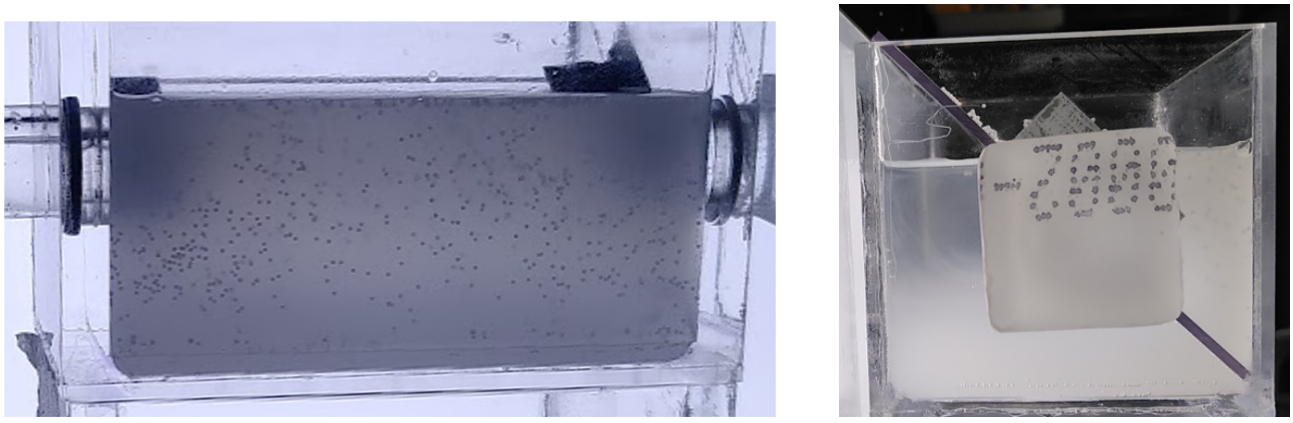

(a) (b)

Figure 27: Turbid liquid in a preliminary calibration measurement. The cloudiness is caused by dust present on particles that haven't been cleaned before use. Front view (a) and side view (b).

6.2 Calibration outcomes

Even though the calibration experiments were conducted with the explicit goal of acquiring a calibration curve for the pipe flow experiments, it is also worthwhile to discuss their outcomes separately. Firstly it should be mentioned that the variation of the LED panel intensity and the presence and fluctuation of extraneous light as mentioned in section 6.1 were present during these measurements. However, the impact that these error sources had is only moderate, as the 95% confidence interval is quite slim and the curves all collapse onto a single curve. This suggests both that the variation during measurements as well as between consecutive measurements was

only minor. This means that we can say with some level of confidence that the found calibration curve is a good representation of the light attenuation behaviour in this experimental setup.
The attenuation behaviour found for this system starts out linear at low $\phi\ell$ before the slope begins changing and it starts to follow a cube root function. This suggests that the Beer-Lambert law is applicable at low $\phi\ell$ while at higher $\phi\ell$ there is a negative deviation from the Beer-Lambert law. This is in line with the expectations based on previous experiments, as mentioned in section 2.4.3. As this section also mentions, there are many possible causes for a negative deviation from the Beer-Lambert law. In the present case, the distinct two region behaviour tells us that the cause of the deviation is linked to an increase in particles in the volume between the light source and the camera. This means that it has something to do with interactions between the particles and is not due to a material or geometric property of the particles. One explanation could come from the concepts of optical depth (τ) and mean free path (λ). The mean free path is the average distance light can travel through the suspension without encountering a particle and it is defined as $\lambda = 1/\sigma n$ where σ is the cross-sectional area of the particles and $n = \phi/V_p$ is the number density of the particles, which uses the volume of a single particle V_p. The optical depth is another measure that compares the amount of light transmitted through a system to the original light intensity, it is related to transmission and attenuation. It can be defined as $\tau = \ell/\lambda = \ell\sigma n$. In the context of highly scattering media, the optical depth can be used to predict whether single or multiple scattering behaviour will dominate. The domains that are generally used (e.g. Swanson et al., 1999; Piederrière et al., 2004) are $\tau < 1$ for single scattering, $1 < \tau \leq 10$ for multiple scattering and $\tau > 10$ for diffusion. It should be noted that diffusion in this case is simply the result of a high number of subsequent scattering events and can therefore still be considered multiple scattering. We can define the optical depth in the current system as such.

$$\tau = \ell\sigma n = \frac{\sigma}{V_p}\phi\ell = \frac{4}{3}\frac{1}{r_p}\phi\ell = \frac{15}{13}\phi\ell \tag{32}$$

where $r_p = d/2 = 0.65$ mm is the radius of a particle. Here the general formulas for the volume of a sphere and the area of a circle are used to simplify the equation before solving it. This means that the margins of the different scattering domains can be defined as a function of $\phi\ell$.

$$\tau = 1 \rightarrow \phi\ell = \frac{13}{15} \approx 0.87\text{mm} \tag{33a}$$

$$\tau = 10 \rightarrow \phi\ell = \frac{130}{15} \approx 8.7\text{mm} \tag{33b}$$

If we look at Fig. 19 again, we see that the lower bound does seem to coincide with the deviation from the linear behaviour. However, the transition region from linear to cube root behaviour ends at around $\phi\ell \approx 4$ mm. Nevertheless, the characteristic behaviour of these two domains with a transition region in between does suggest that the cause of the deviation from the Beer-Lambert law is multiple scattering. New experiments could be used to verify this, specifically by generating more data for lower $\phi\ell$. As the current setup only generated data for $\ell \geq 6$ mm, there is no data for $\phi\ell < 0.15$ mm and for $\phi\ell < 0.6$ mm the data is a combination of only four measured curves which are somewhat noisy. Generating more data in this regime can strengthen the finding that the Beer-Lambert law is applicable in this region.
The presence of light scattering effects is confirmed by extra experiments that were done. The setup was exactly the same as for the calibration measurements with the only difference being that a black paper sheet with a small square cut out was placed between the LED panel and the box holding the suspension. This meant that there was only a small area where light came through. The background image, shown in Fig. 28a, clearly shows this square hole being bright while the surrounding areas are dark. However when particles are added, the light intensity in the entire box is higher than in the background image. While the square hole is still clearly the brightest spot, the surrounding areas aren't as dark as in the background image. This is shown for $\phi_b = 0.10$ in Fig. 28b. To make this relatively small change in intensity visible, the images aren't shown in gray scale but in a different colour mapping. Please note that any pixel with an intensity above 1000 has the same deep red colour. The maximum intensity in the square hole of the background image was close to 60 000. If we compare the light intensity within the horizontal band bounded by the two dashed red lines in Fig. 28a we can quantify the difference in light intensity of the areas besides the square hole, this is shown in Fig. 28c. We can see that the background intensity to the left of the square hole is around 350. For all three cases with particles this value is around 700. If we also calculate the average attenuation measured at the square hole for all three ϕ_b and compare them to the calibration curve we found with the regular calibration setup, we can see that the measured A_t is much higher than the calibrated values. This is shown in Fig. 28d. This is likely because the small amount of light that enters through the square hole is scattered throughout the entire system. This also happens in the regular calibration measurements but in that case there is light from other parts of the LED panel being scattered to the relevant area, resulting in a higher light intensity and thus a lower A_t. This all

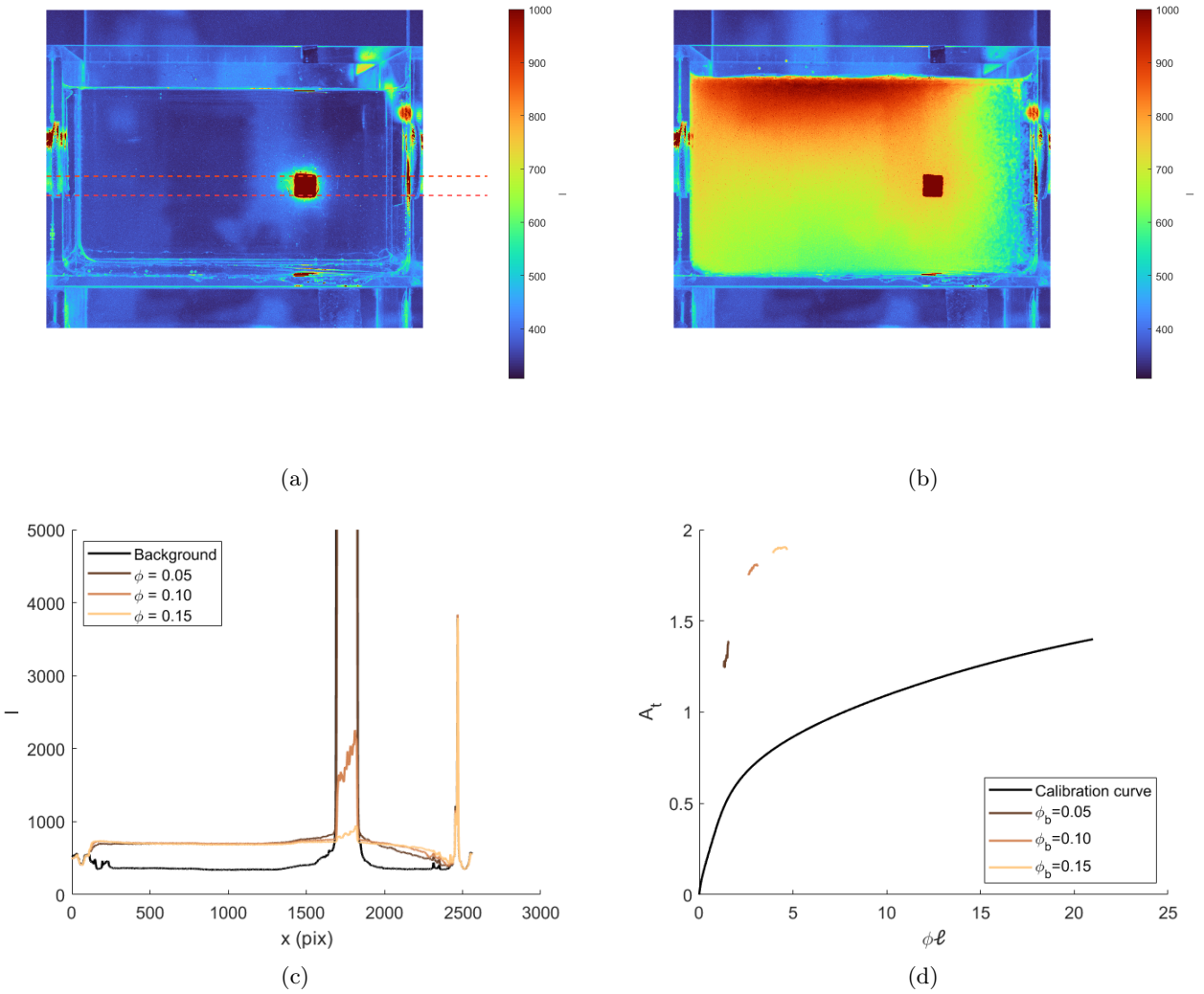

Figure 28: Calibration measurements done with a sheet with a square hole cut out. The background intensity (a) and the intensity measured with $\phi_b = 0.10$ (b) clearly show that the light intensity besides the square hole is higher when particles are present. This is also shown in the intensity plot (c) which shows the vertical average of the intensity as function of x within the red dashed lines in figure (a). Due to light diffusion, the measured attenuation at the square hole (d) does not line up with the calibrated values.

supports the hypothesis that the main factor in light attenuation for suspensions beyond a certain $\phi\ell$ is multiple scattering. It should be noted that just as the regular calibration experiments, these experiments were not shielded from outside light. It therefore cannot be ruled out that the higher intensity besides the square hole for the suspension measurements was partly due to the particles scattering extraneous light. This is supported by the fact that the particles near the top of Fig. 28b are brighter than those that are lower.

While this all tells us that a considerable amount of light is scattered and diverted from its original trajectory, the fact that the outline of the square are still visible in Fig. 28b suggests that a lot of light also passes through the system without being diverted. This means that the light scattering can not yet be considered diffusion, as this would require the edges of the square to blur significantly. To verify that this is not the case we can look at the gradient of the average light intensity profiles from Fig. 28c. These gradients are shown in Fig. 29 for the different ϕ_b investigated. Only the area surrounding the square is shown and the values on the vertical axis are different in each sub-figure. The profile in Fig. 29a shows two noticeable peaks at the edges of the square. This is of course expected as the background image shows a clear view of the cut out. The profiles in Figs. 29b and 29c show similar sudden peaks, although they are of course less high because the light intensity is lower. This means that for these particle loadings the edges of the square are still clearly measurable. If the light was diffusing strongly, the gradient would increase over a broader area as the edges of the square would blur. The erratic behaviour of the gradient between the two peaks in these two profiles shows that the measurements had

not yet converged properly. For a well converged measurement we would expect the light intensity measured in the square to vary consistently from left to right causing the gradient to be a positive value. Even in Fig. 29d the two peaks can be seen at the edges of the square cut out. This suggests that diffusion is still not happening significantly. However, since the fluctuations of the gradient within the square area are of the same magnitude as the peaks. This conclusion is less strong for this measurement than for the previous measurements. This could be verified by doing new measurements that are properly converged which would reduce the fluctuations of the gradient between the two peaks.

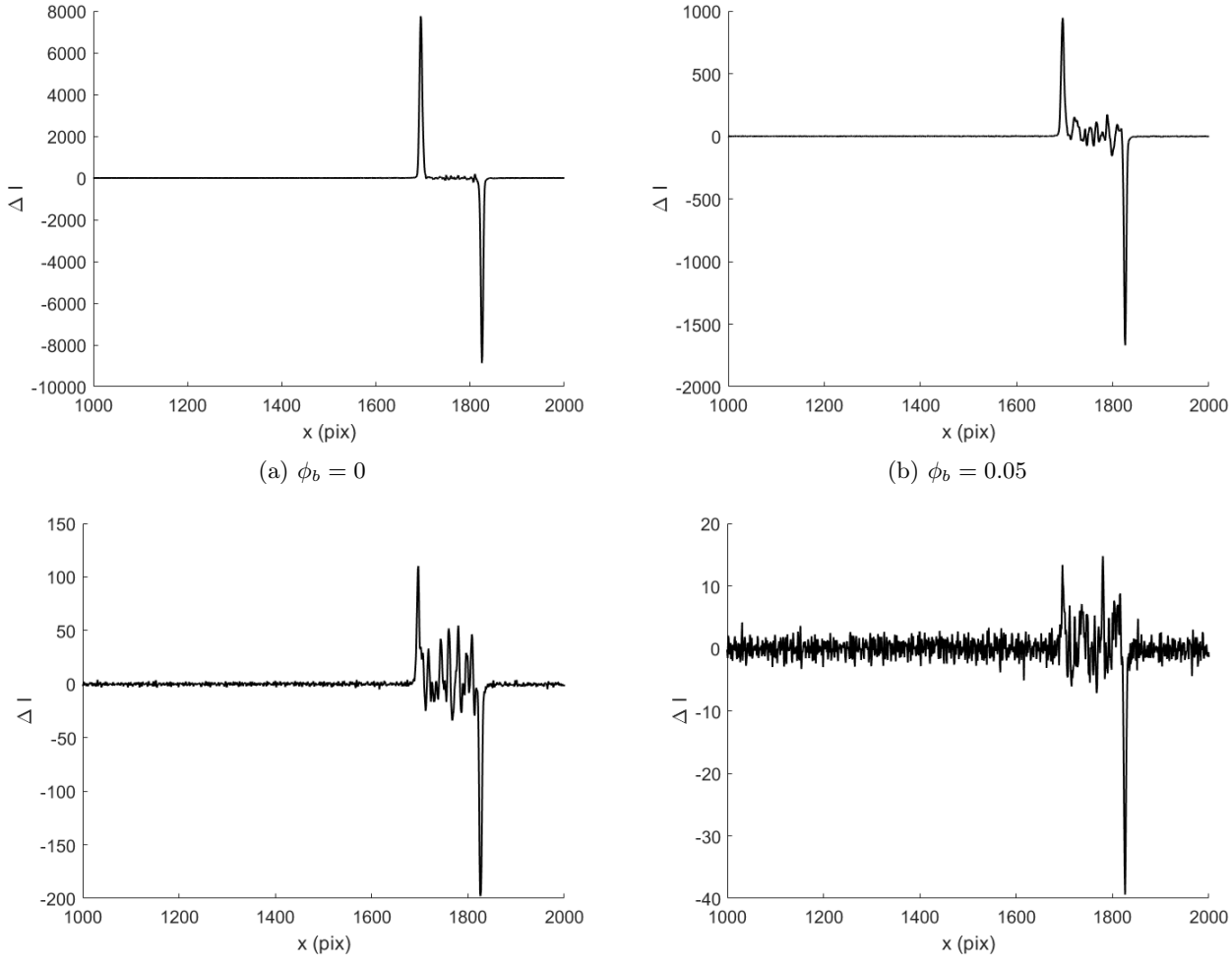

(a) $\phi_b = 0$

(b) $\phi_b = 0.05$

(c) $\phi_b = 0.10$

(d) $\phi_b = 0.15$

Figure 29: Spatial gradient of the average light intensity in the calibration measurements done with a sheet with a square hole cut out for varying bulk volume fractions. The peaks in the gradient show the edges of the square hole.

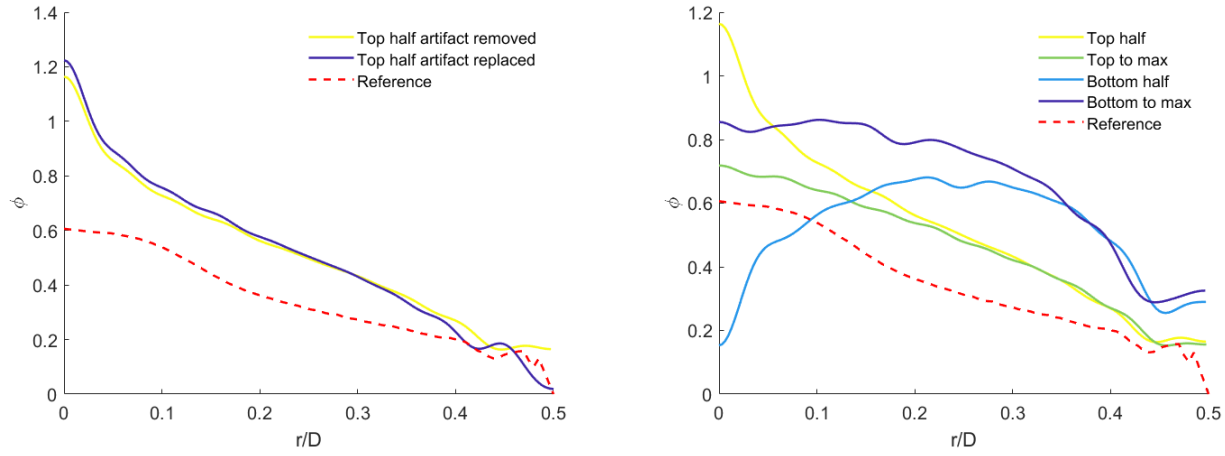

(a) (b)

Figure 30: Resulting radial ϕ profiles using different parts of the A_t profile for $\phi_b = 0.25$ and $Re_s = 1051$ as input compared to reference data from Hogendoorn, Breugem, et al. (2023) for $\phi_b = 0.252$ and $Re_s = 1083$ or case 1 in the reference. Comparison between using the top half of the profile with the edge artifact removed or replacing the artifact with values descending linearly to zero (a). Comparison between using the top half of the profile, from the top to the maximum value, the bottom half or from the bottom to the maximum value (b) all with the edge artifacts removed.

6.3 Pipe flow outcomes

The deviation of the pipe flow measurement outcomes from the calibration means that these outcomes are not quantitatively correct. Nevertheless we can discuss their qualitative differences and discuss the applicability of the used methods. As mentioned in section 5, the non-symmetry of the attenuation profiles, resulting from the non-neutral buoyancy of the particles, poses an issue for the inverse Abel transform. To investigate the impact this has on the resulting radial ϕ profiles, the inverse Abel transform was applied to different sections of the attenuation profiles. As the inverse Abel transform is supposed to be applied to symmetric profiles, the numerical inverse Abel transform function in Matlab only requires half an attenuation profile as input. In section 5, the top half of the measured profiles was used, with the artifact present at the edge removed. Firstly, the impact of this artifact removal can be investigated by replacing the artifact with descending positive values. The choice was made to simply replace them with a linear interpolation from the last reliable A_t value near the edge to zero. This interpolated A_t profile was then used as input for the inverse Abel transform. An example of such a resulting radial ϕ profile can be seen in Fig. 30a for the case where $\phi_b = 0.25$ and $Re_s = 1051$. Comparing it to the profile where the artifact was removed shows some notable differences. Replacing the artifact causes the radial ϕ profile to drop to a lower value at the edge of the pipe where $r/D = 0.5$. Although it is more realistic for the ϕ at the edge to be close to zero, the shape at the edge does not resemble the shape of the reference profile. This suggests that a linear interpolation is not a good representation of the actual A_t profile. A result of this lower value at the edge is that the peak value at the centre is now higher than before. The local minimum of the wiggle near the edge has shifted further away from the wall compared to the profile where the artifact was removed. The minimum of the old profile is at $r/D = 0.447$ and for the new profile it is at $r/D = 0.425$. The expected value of the minimum based on the particle diameter is $r/D = 0.435$. This difference shows that measuring the location of this local minimum accurately, requires a reliable measurement of the attenuation at the edge of the pipe. Alternatively, the fact the the correct location of the minimum is known a priori can be used to quantify the precision of any radial ϕ profiles.

Secondly, the impact of using different parts of the A_t profiles as input for the inverse Abel transform is considered. Both the top and the bottom halves of the A_t profiles are used as well as the top and bottom parts separated by the maximum value of the A_t profile for the $\phi_b = 0.25$ and $Re_s = 1051$ case. The top and bottom halves are technically the only correct profiles to use with the inverse Abel transform, as they should start at the centre and end at the edge. In the case of a symmetrical A_t profile these result in the same radial ϕ distribution. However, since the A_t profiles aren't symmetric, the gradient at the midline is not zero. To investigate the impact of this, the top and bottom parts of the A_t profile separated by the maximum are also processed. For this case, the maximum is at $y = 11.88$ mm. The resulting profiles are shown in Fig. 30b. As expected, none of the profiles resemble the shape of the reference profile. But comparing the shapes of the profiles among themselves

does tell us a few things. Firstly, the impact of the non-zero slope at the midline is significant. This is illustrated mostly by the stark difference in the peak values of the yellow and green top curves at $r/D = 0$. Even though the A_t profile for the green curve has a higher peak value, the ϕ profile does not show a drastic peak at the centre. This shows that the peaks present in most ϕ profiles in Fig. 24 are a result of the non-zero slope at the midline of the A_t profiles. The bottom half of the A_t profile was used to generate the light blue curve. As expected, the off centre maximum causes the resulting ϕ profile to drop significantly towards the centre. When comparing the dark blue and green curves for the top and bottom parts of the A_t profile separated by the maximum, we see that neither displays a sharp peak or drop at $r/D = 0$. This all suggests once more that the impact of the non-neutral buoyancy of the particles during the pipe flow experiments was quite detrimental to the final results.

7 Conclusion and recommendations

This thesis' primary goal was to verify the applicability of a proposed light attenuation measurement technique to measure volume fraction distributions in neutrally buoyant suspension pipe flows. As has been discussed, the current investigation ran into multiple issues. Foremost the density mismatch between the suspending liquid and the solid particles during the pipe flow experiments. This caused the flow to not be neutrally buoyant, which resulted in an average particle distribution that is not axisymmetric. The measurement method was specifically designed to be applied to neutrally buoyant systems, and thus only captures a projection of the flow from one angle. This means it cannot be used to characterise the 3 dimensional particle distribution in the non-neutrally buoyant flow. However, this is explicitly not a shortcoming of the light attenuation measurement method, but a mistake in the conducted experiments. This does mean that the gathered data cannot be used to investigate particle migration in neutrally buoyant suspensions and thus the last two research questions posed in section 2.5 cannot be answered presently. The data is however, sufficient to discuss the precision of the method. The measured attenuation profiles for different bulk solid volume fractions shown in Fig. 20 show a consistent increase in A_t for increasing ϕ_b. All the profiles are distinguishable from each other and, apart from the edge artifacts, they never overlap. This suggests that the method is precise enough to distinguish variations of at least $\phi = \pm 0.01$, even at low ℓ, as this is the minimum difference in ϕ_b between measurements. At the lowest measured path length of $\ell = 6.5$ mm this corresponds to a precision of $\phi\ell = \pm 0.065$. The potential precision might be even better than this since the path lengths $\ell < 6.5$ are only inaccessible because of the shadow cast by the wall of the pipe near the top and bottom edges of the images. This is supported by the fact that measurements at constant ϕ_b and differing Re_s showed slight differences in the attenuation profiles that are in line with the increase of shear-induced migration that is expected when lowering Re_s, as described by Hogendoorn, Breugem, et al., 2023. This is further supported by the calibration results, which had a minimum measurable path length of $\ell = 6$ mm which corresponded to a minimum $\phi\ell = 0.15$ mm. However, for these low path lengths, the average attenuation was a bit noisy. This suggest that the measurements for low $\phi\ell$ had not converged properly yet. Taking longer measurements could solve this issue. The minimum path length in the calibration experiments is governed by the experimental setup, at lower path lengths the line of sight also crosses through the side wall of the box. It could be possible to measure the attenuation of the particles at lower ℓ by altering the setup to avoid this. While this all suggests that light attenuation measurements can be used to measure the volume fraction with quite a high level of precision, the exact connection between measured A_t and the parameter of interest $\phi\ell$ present in the flow is not known for the pipe flow experiments. The calibrated values for $\phi\ell = f(A_t)$ did not coincide with the measured values in the pipe flow experiments. Sections 4 and 6.1 discussed the details of this mismatch and certain potential causes for it. This means that although the current investigation suggest that a high level of precision is possible in measuring $\phi\ell$ with this light attenuation method, it has not actually succeeded in doing so. However, the expected negative deviation from Beer-Lambert has been verified. The likely cause of this behaviour is multiple scattering.

There are certain improvements that can be made to the experimental procedures to avoid certain issues that were encountered. Firstly, more care should be put into matching the density of the liquid to that of the particles. Since the current procedure, described in section 3, is somewhat slow, it is likely that the suspension was deemed neutrally buoyant before the liquids had mixed properly. Simply taking more time for this step can resolve this issue. It should also be noted that the pump heats up the suspension, thus reducing the density of the liquid slightly. Whether this change is enough to cause non-neutrally buoyant behaviour can not be established with the current data since the flow was never neutrally buoyant to begin with. If this does prove to be an issue, a heat exchanger may be added to the flow loop. However, many references in the literature that used similar flow loops also do not include a heat exchanger, suggesting that this may not be necessary. Secondly, the attenuation artifact near the top and bottom edges of the pipe may be reduced by getting a closer

refractive index match between the liquid and the acrylic material of the pipe. However, the liquid is a mixture of water and glycerol, which is mixed to try to match the density of the particles. Since the refractive index of the mixture changes depending on its composition, obtaining a good density match as well as a good refractive index match is complicated. Adding additional solvents to get a closer index match will change the density as well. A proper density match has priority over a proper index match since the goal of the experiments is researching neutrally buoyant suspensions. This means that the attenuation artifacts near the walls may be unavoidable to a degree. This will have an effect on the resulting radial volume fraction profiles. Since the near-wall behaviour is present at every point on the pipe wall, it impacts the entire attenuation projection. If the attenuation profiles and thus the $\phi\ell$ profiles are better defined at the edges, the near-wall behaviour can be measured on its own. This means that we will know better which impact the near-wall behaviour has on the entire projection. Therefore, acquiring a good refractive index match is beneficial, even though it is complicated.
Thirdly, it is important to acquire a calibration curve that is applicable to the pipe flow measurements. There are essentially two ways to go about this. The first method would be to create a calibration curve with data that was gathered in the pipe flow setup itself. This is not straight forward though, since we know that the particles are rarely actually equally distributed in the pipe. This means that the local volume fraction distribution is not known, and thus the value for $\phi\ell$ is not known at each point on the projection. The only place in the projection that is not impacted by this is the midline. If the flow is neutrally buoyant, the particle migration behaviour will be axisymmetric and the value for $\phi\ell$ will not change based on particle migration. This does mean that the calibration curve will need to be constructed from many different measurements with different ϕ_b. This brings another issue with this method, namely that the effective bulk volume fraction in the pipe often deviates from the bulk volume fraction in the reservoir. This can be caused by particles that are exceptionally light or heavy getting stuck in the system somewhere and thus not flowing through the pipe. Additionally, particle migration causes the particles to have an average velocity that is different from that of the liquid, altering the effective volume fraction as well. These issues could be mitigated by designing a different experimental setup to ensure proper mixing of the suspension right before the measurement area. The second method for acquiring a proper calibration curve would be to redo the calibration measurements as they were done for this investigation, but with some minor tweaks to avoid the issues mentioned in 6.1. Firstly, both the calibration setup and the pipe flow setup should be shielded to avoid extraneous light entering the camera lens. This would require a redesign of the calibration setup, either so that is does not need to be stirred by hand as this inhibits the setup being shielded in the current way, or by using a different shielding method that allows access to the setup. Secondly both setups should also continuously measure the intensity of the LED panel so that any intensity fluctuations are measured and can be accounted for in the results processing. Thirdly, the pipe flow setup should be adjusted so that the turbidity of the liquid can be monitored during the experiments as well. This could be done by adding a pipe above the current one that contains the liquid but prevents the particles from getting in. This does make the volume fraction calculations a little more complicated and would require more pumping power. Alternatively, the turbidity of the water can be checked periodically by taking a water sample every now and then and placing it in a transparent vessel in the camera frame. This is a simpler option, but it does not provide instant monitoring of the liquid turbidity.
In short, although certain errors in the experimental execution make it impossible to use the present data to investigate particle migration in neutrally buoyant suspensions, the results do show that light attenuation measurements are potentially a very useful tool for this research. In the first place because it is fast and relatively easy to apply and secondly because the measurements are precise enough to distinguish between different bulk volume fractions and different levels of shear-induced migration. The expected deviation from the Beer-Lambert law for higher particle loadings has been verified and the mechanism that is the likely cause of this is multiple scattering.

A Measurement convergence

The convergence of the pipe flow measurements can be investigated by looking at the difference between the current and the previous mean for each subsequent sample. This was first done with a single measurement in the pipe flow which had $\phi_b \approx 0.025$, $Re_s \approx 6000$ and $N_{tot} = 6000$. These flow values are approximate because a mistake in the initial filling process of the flow loop was made. This meant that the total liquid volume was not known accurately, which means that ϕ_b was not known accurately. Because of this these results are not included in the main results discussion. The convergence of the average intensity value at a single pixel is shown in Fig. 31a. The location of this pixels is shown in Fig. 32. Fig. 31b shows the moving mean of the values from Fig. 31a. From this we can see that the difference between the current and previous mean is below 10 for $N_{tot} = 2000$. The average intensity value here is around 35 000, meaning that the change with subsequent samples is less than 0.03%. This was deemed a sufficiently converged average. Similar measurement with $N_{tot} = 2000$ were then done for higher particle loadings, the results of which are also shown in Fig. 31. As expected, they converge slightly faster as more particles present cause less variation in the measured intensity values. It should be noted that the desired result from these measurements is the attenuation and not just the intensity. However, since the attenuation is a logarithmic function of the intensity, it is more intuitive to look at the difference in the mean intensity. Additionally, the attenuation measurements are also averaged spatially in the horizontal direction before they are processed further. This means that every image taken contains more than two thousand samples for every value of y. This means that the actual variable of interest will converge even faster than the pixel intensity considered here. All things considered, this was deemed sufficient evidence that $N_{tot} = 2000$ is enough to obtain converged measurements.

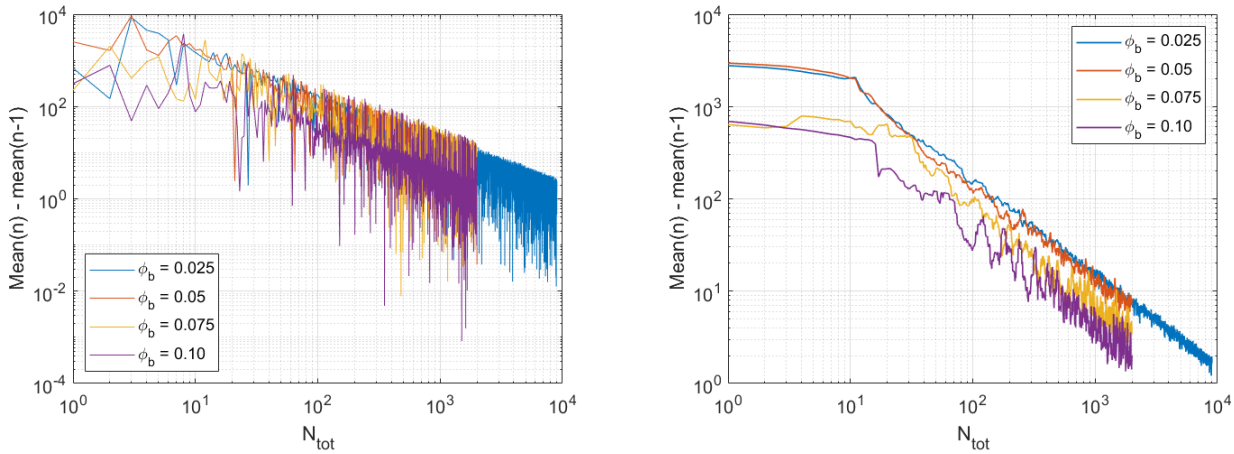

Figure 31: Convergence of the mean intensity at a single pixel for differing ϕ_b (a) and the moving mean of this convergence using a window size of 17 (b).

Figure 32: Position of the pixel that was used for the convergence plots.

B Attenuation calculation

In spectrophotometry, the attenuation of a substance is generally calculated by comparing the measured light intensity that passes through the substance to the background intensity that was measured in the same setup without the attenuating substance. For this background measurement, a cuvette with the suspending liquid but without the substance of interest is present in the spectrophotometer. The resulting measured intensity will thus be used as I_0 in Eq. 17. We can use the schematic shown in Fig. 33 to mathematically verify that this method can also be applied to the present case. Since we are only interested in the attenuation caused by the particles, the value we want to find is

$$A_t = log_{10}\frac{I_1}{I_2} = log_{10}\frac{1}{T_p} \tag{34}$$

where I_1 and I_2 are the light intensity before and after the light passes through the particles respectively and T_p is the transmittance through the particles. We can further define the total transmittance based on the light intensity at the LED panel I_{start} and at the camera I_{end} as

$$T_{tot} = \frac{I_{end}}{I_{start}}. \tag{35}$$

We then find that

$$I_{end} = T_{tot} I_{start} = T_2 T_p T_1 I_{start} \tag{36}$$

since

$$T_2 T_p T_1 = \frac{I_{end}}{I_2}\frac{I_2}{I_1}\frac{I_1}{I_{start}} = \frac{I_{end}}{I_{start}} = T_{tot}. \tag{37}$$

In the case where there are no particles, we know that $I_2 = I_1$. This means that the light intensity at the camera in this case is

$$I_{end,\phi=0} = T_2 T_1 I_{start}. \tag{38}$$

If we divide Eq. 36 by Eq. 38 we find that

$$\frac{I_{end}}{I_{end,\phi=0}} = T_p = \frac{I_2}{I_1} \tag{39}$$

which means that indeed

$$A_t = log_{10}\frac{I_1}{I_2} = log_{10}\frac{1}{T_p} = log_{10}\frac{I_{end,\phi=0}}{I_{end}}. \tag{40}$$

Thus, comparing the measured intensity to the background intensity measured when $\phi = 0$ is a correct way to calculate the attenuation.

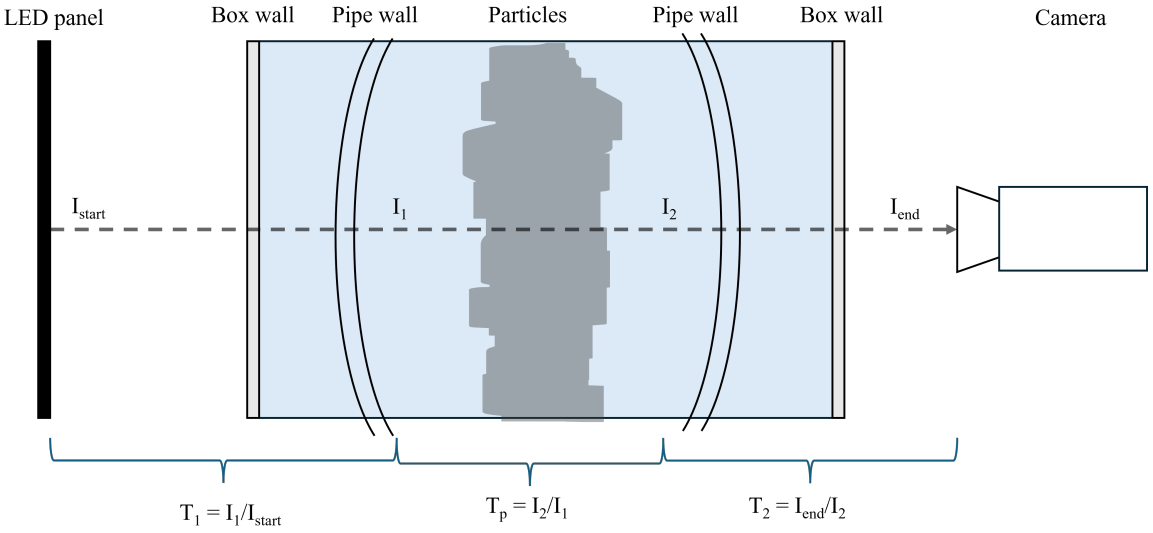

Figure 33: Schematic overview of the measurement section of the pipe flow experiments showing light intensities and transmittance at different positions.

C Polynomial fit to calibration data

As mentioned, an eighth order polynomial fit to the measured calibration data was used as the calibration curve. The coefficients for this polynomial are given in table 6. The polynomial is of the form $\phi\ell = p_1 A_t^8 + p_2 A_t^7 + p_3 A_t^6 + p_4 A_t^5 + p_5 A_t^4 + p_6 A_t^3 + p_7 A_t^2 + p_8 A_t + p_9$. The value for the zeroth order coefficient was set to zero manually to ensure that the calibration curve returns $\phi\ell = 0$ for $A_t = 0$.

Table 6: Coefficients for the eighth order polynomial fit to the calibration measurement data.

Coefficient	Value
p_1	-8.68
p_2	58.69
p_3	-140.89
p_4	145.14
p_5	-48.82
p_6	-7.27
p_7	8.66
p_8	0.87
p_9	0

References

Acién Fernández, F. G., F. García Camacho, J. A. Sánchez Pérez, J. M. Fernández Sevilla, and E. Molina Grima (Sept. 1997). "A model for light distribution and average solar irradiance inside outdoor tubular photobioreactors for the microalgal mass culture". *Biotechnology and Bioengineering* 55.5, pp. 701–714. ISSN: 00063592. DOI: 10.1002/(SICI)1097-0290(19970905)55:5<701::AID-BIT1>3.0.CO;2-F.

Aliseda, Alberto and Theodore J. Heindel (Jan. 2021). "X-Ray Flow Visualization in Multiphase Flows". *Annual Review of Fluid Mechanics* 53.1, pp. 543–567. ISSN: 0066-4189. DOI: 10.1146/annurev-fluid-010719-060201.

Ardekani, Mehdi Niazi, Léa Al Asmar, Francesco Picano, and Luca Brandt (June 2018). "Numerical study of heat transfer in laminar and turbulent pipe flow with finite-size spherical particles". *International Journal of Heat and Fluid Flow* 71, pp. 189–199. ISSN: 0142727X. DOI: 10.1016/j.ijheatfluidflow.2018.04.002.

Avila, Kerstin, David Moxey, Alberto de Lozar, Marc Avila, Dwight Barkley, and Björn Hof (July 2011). "The Onset of Turbulence in Pipe Flow". *Science* 333.6039, pp. 192–196. ISSN: 0036-8075. DOI: 10.1126/science.1203223.

Bachmann, Lorin M. and W. Greg Miller (2020). "Spectrophotometry". *Contemporary Practice in Clinical Chemistry*. Ed. by William Clarke and Mark A Marzinke. 4th ed. Elsevier, pp. 119–133. DOI: 10.1016/B978-0-12-815499-1.00007-7.

Baker, Edward T. and J. William Lavelle (1984). "EFFECT OF PARTICLE SIZE ON THE LIGHT ATTENUATION COEFFICIENT OF NATURAL SUSPENSIONS." *Journal of Geophysical Research* 89.C5, pp. 8197–8203. ISSN: 01480227. DOI: 10.1029/JC089iC05p08197.

Bhatt, Manish, Kalyan R. Ayyalasomayajula, and Phaneendra K. Yalavarthy (July 2016). "Generalized Beer–Lambert model for near-infrared light propagation in thick biological tissues". *Journal of Biomedical Optics* 21.7, p. 076012. ISSN: 1083-3668. DOI: 10.1117/1.jbo.21.7.076012.

Blasius, H. (1913). "Das Aehnlichkeitsgesetz bei Reibungsvorgängen in Flüssigkeiten". *Mitteilungen über Forschungsarbeiten auf dem Gebiete des Ingenieurwesens*. Berlin, Heidelberg: Springer Berlin Heidelberg, pp. 1–41. DOI: 10.1007/978-3-662-02239-9{_}1.

Burdick, G M, N S Berman, and S P Beaudoin (2001). "Describing hydrodynamic particle removal from surfaces using the particle Reynolds number". *Journal of Nanoparticle Research* 3, pp. 455–467.

Carsten Killer (2025). *Abel Inversion Algorithm*. MATLAB Central File Exchange. URL: https://www.mathworks.com/matlabcentral/fileexchange/43639-abel-inversion-algorithm.

Casasanta, Giampietro and Roberto Garra (2018). "Towards a generalized beer-lambert law". *Fractal and Fractional* 2.1, pp. 1–7. ISSN: 25043110. DOI: 10.3390/fractalfract2010008.

Chun, B. and A. J.C. Ladd (2006). "Inertial migration of neutrally buoyant particles in a square duct: An investigation of multiple equilibrium positions". *Physics of Fluids* 18.3. ISSN: 10706631. DOI: 10.1063/1.2176587.

Costa, Pedro, Francesco Picano, Luca Brandt, and Wim Paul Breugem (Sept. 2016). "Universal Scaling Laws for Dense Particle Suspensions in Turbulent Wall-Bounded Flows". *Physical Review Letters* 117.13. ISSN: 10797114. DOI: 10.1103/PhysRevLett.117.134501.

Dash, Amitosh, Willian Hogendoorn, Gosse Oldenziel, and Christian Poelma (Mar. 2022). "Ultrasound imaging velocimetry in particle-laden flows: counteracting attenuation with correlation averaging". *Experiments in Fluids* 63.3. ISSN: 14321114. DOI: 10.1007/s00348-022-03404-x.

Deboeuf, S., N. Lenoir, D. Hautemayou, M. Bornert, F. Blanc, and G. Ovarlez (Mar. 2018). "Imaging non-Brownian particle suspensions with X-ray tomography: Application to the microstructure of Newtonian and viscoplastic suspensions". *Journal of Rheology* 62.2, pp. 643–663. ISSN: 0148-6055. DOI: 10.1122/1.4994081.

Dekking, Frederik Michel, Cornelis Kraaikamp, Hendrik Paul Lopuhaä, and Ludolf Erwin Meester (2005). *A Modern Introduction to Probability and Statistics*. London: Springer London. ISBN: 978-1-85233-896-1. DOI: 10.1007/1-84628-168-7.

Delgado, Rosario (2022). "Misuse of Beer-Lambert Law and other calibration curves". *Royal Society Open Science* 9.2. ISSN: 20545703. DOI: 10.1098/rsos.211103.

Eilers, H. (Dec. 1941). "Die Viskosität von Emulsionen hochviskoser Stoffe als Funktion der Konzentration". *Kolloid-Zeitschrift* 97.3, pp. 313–321. ISSN: 0303-402X. DOI: 10.1007/BF01503023.

Fåhræus, Robin and Torsten Lindqvist (Mar. 1931). "THE VISCOSITY OF THE BLOOD IN NARROW CAPILLARY TUBES". *American Journal of Physiology-Legacy Content* 96.3, pp. 562–568. ISSN: 0002-9513. DOI: 10.1152/ajplegacy.1931.96.3.562.

Figliola, R. S.. and Donald E.. Beasley (2015). *Theory and design for mechanical measurements*. John Wiley & Sons, p. 614. ISBN: 9781118881279.

Gadala-Maria, F. and Andreas Acrivos (Dec. 1980). "Shear-Induced Structure in a Concentrated Suspension of Solid Spheres". *Journal of Rheology* 24.6, pp. 799–814. ISSN: 0148-6055. DOI: 10.1122/1.549584.

Gholami, Mohammad, Ahmadreza Rashedi, Nicolas Lenoir, David Hautemayou, Guillaume Ovarlez, and Sarah Hormozi (July 2018). "Time-resolved 2D concentration maps in flowing suspensions using X-ray". *Journal of Rheology* 62.4, pp. 955–974. ISSN: 0148-6055. DOI: 10.1122/1.4994063.

Hampton, R. E., A. A. Mammoli, A. L. Graham, N. Tetlow, and S. A. Altobelli (May 1997). "Migration of particles undergoing pressure-driven flow in a circular conduit". *Journal of Rheology* 41.3, pp. 621–640. ISSN: 0148-6055. DOI: 10.1122/1.550863.

Han, Minsoo, Chongyoup Kim, Minchul Kim, and Soonchil Lee (Sept. 1999). "Particle migration in tube flow of suspensions". *Journal of Rheology* 43.5, pp. 1157–1174. ISSN: 0148-6055. DOI: 10.1122/1.551019.

Hogendoorn, Willian, Wim Paul Breugem, David Frank, Martin Bruschewski, Sven Grundmann, and Christian Poelma (Dec. 2023). "From nearly homogeneous to core-peaking suspensions: Insight in suspension pipe flows using MRI and DNS". *Physical Review Fluids* 8.12. ISSN: 2469990X. DOI: 10.1103/PhysRevFluids.8.124302.

Hogendoorn, Willian, Bidhan Chandra, and Christian Poelma (June 2021). "Suspension dynamics in transitional pipe flow". *Physical Review Fluids* 6.6. ISSN: 2469990X. DOI: 10.1103/PhysRevFluids.6.064301.

Hogendoorn, Willian, Bidhan Chandra, and Christian Poelma (Apr. 2022). "Onset of turbulence in particle-laden pipe flows". *Physical Review Fluids* 7.4. ISSN: 2469990X. DOI: 10.1103/PhysRevFluids.7.L042301.

Hogendoorn, Willian and Christian Poelma (Nov. 2018). "Particle-Laden Pipe Flows at High Volume Fractions Show Transition Without Puffs". *Physical Review Letters* 121.19. ISSN: 10797114. DOI: 10.1103/PhysRevLett.121.194501.

Hollas, J. Michael (2004). *Modern Spectroscopy*. 4th ed. John Wiley & Sons.

Jamshidi, Rashid, Jurriaan J.J. Gillissen, Panagiota Angeli, and Luca Mazzei (Jan. 2021). "Roles of solid effective stress and fluid-particle interaction force in modeling shear-induced particle migration in non-Brownian suspensions". *Physical Review Fluids* 6.1. ISSN: 2469990X. DOI: 10.1103/PhysRevFluids.6.014301.

Karnis, A, H L Goldsmith, and S G Mason (1966). "The Kinetics of Flowing Dispersions I. Concentrated Suspensions of Rigid Particles 1". *JOURNAL OF COLLOID AND INTERFACE SCIENCE* 9, pp. 531–553.

Kiteto, Moses Kayanda and Cleophas Achisa Mecha (Sept. 2024). "Insight into the Bouguer-Beer-Lambert Law: A review". *Sustainable Chemical Engineering*, pp. 567–587. ISSN: 2717-5758. DOI: 10.37256/sce.5220245325.

Kocsis, L., P. Herman, and A. Eke (Mar. 2006). "The modified Beer-Lambert law revisited". *Physics in Medicine and Biology* 51.5. ISSN: 00319155. DOI: 10.1088/0031-9155/51/5/N02.

Kulkarni, Pandurang M. and Jeffrey F. Morris (2008). "Suspension properties at finite Reynolds number from simulated shear flow". *Physics of Fluids*. Vol. 20. 4. American Institute of Physics Inc. DOI: 10.1063/1.2911017.

Leighton, David and Andreas Acrivos (1987). "The Shear-Induced Migration of Particles in Concentrated Suspensions". *Journal of Fluid Mechanics* 181, pp. 415–439. ISSN: 14697645. DOI: 10.1017/S0022112087002155.

Leskovec, Martin, Sagar Zade, Mehdi Niazi, Pedro Costa, Fredrik Lundell, and Luca Brandt (Sept. 2024). "Turbulent pipe flow with spherical particles: Drag as a function of particle size and volume fraction". *International Journal of Multiphase Flow* 179. ISSN: 03019322. DOI: 10.1016/j.ijmultiphaseflow.2024.104931.

Liu, Wenwei and Chuan Yu Wu (June 2019). "Analysis of inertial migration of neutrally buoyant particle suspensions in a planar Poiseuille flow with a coupled lattice Boltzmann method-discrete element method". *Physics of Fluids* 31.6. ISSN: 10897666. DOI: 10.1063/1.5095758.

Markova, A. I., S. D. Khizhnyak, E. Ruehl, and P. M. Pakhomov (Sept. 2021). "Spectroscopic Method for Studying the Morphology of Suspensions". *Journal of Applied Spectroscopy* 88.4, pp. 744–748. ISSN: 15738647. DOI: 10.1007/s10812-021-01234-z.

Martel, Joseph M. and Mehmet Toner (2014). *Inertial focusing in microfluidics*. DOI: 10.1146/annurev-bioeng-121813-120704.

Matas, Jean Philippe, Virginie Glezer, Élisabeth Guazzelli, and Jeffrey F. Morris (2004). "Trains of particles in finite-Reynolds-number pipe flow". *Physics of Fluids* 16.11, pp. 4192–4195. ISSN: 10706631. DOI: 10.1063/1.1791460.

Matas, Jean Philippe, Jeffrey F. Morris, and Élisabeth Guazzelli (2009). "Lateral force on a rigid sphere in large-inertia laminar pipe flow". *Journal of Fluid Mechanics* 621, pp. 59–67. ISSN: 14697645. DOI: 10.1017/S0022112008004977.

Mayerhöfer, Thomas G., Susanne Pahlow, and Jürgen Popp (Sept. 2020). *The Bouguer-Beer-Lambert Law: Shining Light on the Obscure*. DOI: 10.1002/cphc.202000464.

Mirbod, Parisa (Apr. 2016). "Two-dimensional computational fluid dynamical investigation of particle migration in rotating eccentric cylinders using suspension balance model". *International Journal of Multiphase Flow* 80, pp. 79–88. ISSN: 03019322. DOI: 10.1016/j.ijmultiphaseflow.2015.11.002.

Moody, Lewis F (Nov. 1944). "Friction Factors for Pipe Flow". *Transactions of the A.S.M.E.* 66.8, pp. 671–684. DOI: 10.1115/1.4018140.

Nott, Prabhu R. and John F. Brady (Sept. 1994). "Pressure-driven flow of suspensions: Simulation and theory". *Journal of Fluid Mechanics* 275.6, pp. 157–199. ISSN: 14697645. DOI: 10.1017/S0022112094002326.

Nott, Prabhu R., Elisabeth Guazzelli, and Olivier Pouliquen (2011). "The suspension balance model revisited". *Physics of Fluids* 23.4. ISSN: 10706631. DOI: 10.1063/1.3570921.

Orsi, Michel, Laurent Lobry, Elisabeth Lemaire, and François Peters (Nov. 2024). "Mass and momentum balance during particle migration in the pressure-driven flow of frictional non-Brownian suspensions". *Journal of Fluid Mechanics* 998, A16. ISSN: 0022-1120. DOI: 10.1017/jfm.2024.609. URL: https://www.cambridge.org/core/product/identifier/S0022112024006098/type/journal_article.

Piederrière, Y., J. Cariou, Y. Guern, B. Le Jeune, G. Le Brun, and J. Lortrian (2004). "Scattering through fluids: speckle size measurement and Monte Carlo simulations close to and into the multiple scattering". *Optics Express* 12.1, p. 176. ISSN: 1094-4087. DOI: 10.1364/OPEX.12.000176.

Piedra, Patricio, Aimable Kalume, Evgenij Zubko, Daniel Mackowski, Yong Le Pan, and Gorden Videen (July 2019). "Particle-shape classification using light scattering: An exercise in deep learning". *Journal of Quantitative Spectroscopy and Radiative Transfer* 231, pp. 140–156. ISSN: 00224073. DOI: 10.1016/j.jqsrt.2019.04.013.

Pirozzoli, Sergio, Davide Modesti, Paolo Orlandi, and Francesco Grasso (Apr. 2018). "Turbulence and secondary motions in square duct flow". *Journal of Fluid Mechanics* 840, pp. 631–655. ISSN: 14697645. DOI: 10.1017/jfm.2018.66.

Pretzler, Georg (July 1991). "A New Method for Numerical Abel-Inversion". *Zeitschrift für Naturforschung A* 46.7, pp. 639–641. ISSN: 1865-7109. DOI: 10.1515/zna-1991-0715.

Reynolds, Osborne (Jan. 1883). "III. An experimental investigation of the circumstances which determine whether the motion of water shall be direct or sinuous, and of the law of resistance in parallel channels". *Proceedings of the Royal Society of London* 35.224-226, pp. 84–99. DOI: https://doi.org/10.1098/rspl.1883.0018. URL: https://royalsocietypublishing.org/.

Seeger, A., K. Affeld, L. Goubergrits, E. Wellnhofer, and U. Kertzscher (Aug. 2001). "X-ray-based assessment of the three-dimensional velocity of the liquid phase in a bubble column". *Experiments in Fluids* 31.2, pp. 193–201. ISSN: 0723-4864. DOI: 10.1007/s003480100273.

Segré, G. and A. Silberberg (1962). "Behaviour of macroscopic rigid spheres in Poiseuille flow: Part 2. Experimental results and interpretation". *Journal of Fluid Mechanics* 14.1, pp. 136–157. ISSN: 14697645. DOI: 10.1017/S0022112062001111.

Snook, Braden, Jason E. Butler, and Élisabeth Guazzelli (Nov. 2015). "Dynamics of shear-induced migration of spherical particles in oscillatory pipe flow". *Journal of Fluid Mechanics* 786, pp. 128–153. ISSN: 14697645. DOI: 10.1017/jfm.2015.645.

Swanson, Nancy L., Barton D. Billard, and Theresa L. Gennaro (Sept. 1999). "Limits of optical transmission measurements with application to particle sizing techniques". *Applied Optics* 38.27, p. 5887. ISSN: 0003-6935. DOI: 10.1364/AO.38.005887.

Tropea, Cameron, Alexander L. Yarin, and John F. Foss, eds. (Oct. 2007). *Springer Handbook of Experimental Fluid Mechanics*. Springer Science & Business Media. ISBN: 978-3-540-25141-5.

Volk, Andreas and Christian J. Kähler (May 2018). *Density model for aqueous glycerol solutions*. DOI: 10.1007/s00348-018-2527-y.

Waldschläger, Kryss, Maximilian Born, Win Cowger, Andrew Gray, and Holger Schüttrumpf (Dec. 2020). "Settling and rising velocities of environmentally weathered micro- and macroplastic particles". *Environmental Research* 191. ISSN: 10960953. DOI: 10.1016/j.envres.2020.110192.

White, Frank M. (2016). *Fluid Mechanics*. 8th ed. McGraw-Hill. ISBN: 978-9-814-72017-5.

Xu, Jiangtao, Raleigh R. Hood, and Shenn-Yu Chao (Aug. 2005). "A simple empirical optical model for simulating light attenuation variability in a partially mixed estuary". *Estuaries* 28.4, pp. 572–580. ISSN: 0160-8347. DOI: 10.1007/BF02696068.

Xue, Qingzhong (Feb. 2004). "The influence of particle shape and size on electric conductivity of metal-polymer composites". *European Polymer Journal* 40.2, pp. 323–327. ISSN: 00143057. DOI: 10.1016/j.eurpolymj.2003.10.011.

Zeng, Lanying, Fady Najjar, S. Balachandar, and Paul Fischer (Mar. 2009). "Forces on a finite-sized particle located close to a wall in a linear shear flow". *Physics of Fluids* 21.3. ISSN: 1070-6631. DOI: 10.1063/1.3082232.